Investigating the active role of mechanical force during T-cell activation



Huw Colin-York

University of Oxford

This dissertation is submitted for the degree of

Doctor of Philosophy

Pembroke College November 2016

Declaration

I hereby declare that except where specific reference is made to the work of others, the contents of this dissertation are original and have not been submitted in whole or in part for consideration for any other degree or qualification in this, or any other university. This dissertation is my own work and contains nothing which is the outcome of work done in collaboration with others, except as specified in the text and in the following:

- Rat Basophilic Leukaemia cells expressing Lifeact-citrine were produced by Dr James Felce.
- E6.1-57 Jurkat T cells stably expressing the 1G4-TCR and the corresponding pMHC molecules were produced by Dr Veronica Chang.
- E6.1-57 1G4-TCR Jurkat T cells stably expressing Lifeact-citrine were produced by Dr Marco Fritzsche.
- The calcium response data was collected in cooperation with Ms Angela Lee, an MSc student in the lab of Dr Marco Fritzsche.

Huw Colin-York

November 2016

Acknowledgements

First and foremost, I would like to thank Christian for warmly welcoming me into the Eggeling lab. I deeply appreciate your continued support and confidence in my research.

To Marco, I will always be grateful for the time and freedom that you gave me to pursue my ideas, coupled with your relentless support and encouragement. Without this, the achievements of my thesis would not have been possible.

To all the members of the Eggeling Lab, past and present, you have made my DPhil immensely enjoyable and fulfilling. In particular, to Erdinc, for your guidance; to Silvia, for your valued microscopy expertise; to Falk, for answering my biochemical questions and to Dilip, for answering all those questions that Falk could not. To Chris and Esther, who kept the microscopes running through adversity and to Dominic, whose advice on image analysis and beyond was invaluable. Lastly, to those that started this with me, my fellow DPhil-ers Tess and Gregorio, for all the 'Positive Energy'.

I would also like to acknowledge those members of other labs who contributed to my work. I am hugely grateful to James Felce and Veronica Chang of the Davis Lab, whose efforts ensured me an endless supply of cells. To all those at HHMI Janelia Farm, who helped make the journeys there during my DPhil so fruitful.

Finally, I would like to thank my vitally important family and friends. To my mum and brother, without your indispensable generosity and support this work could not have been realised. To rejuvenate at home on the farm has provided me with the best environment to consolidate my ideas and produce this thesis. To Melissa, for your proof-reading, your patience, your wonderful energy that kept me going, but most of all, your unwavering faith in me.

Abstract

The role of mechanical force has gained increasing interest in the field of cell biology owing to the realisation that cells are continually subject to stresses and strains induced by the cellular environment. Cells are known to be able to sense and react to forces imposed on them by their local environment as well as being able to directly impart force during motility, adhesion and cell division. This is also true for cells of the adaptive immune system, specifically during the intimate cell-cell interaction occurring between the T-cell and Antigen Presenting Cell (APC), known as the Immunological Synapse (IS). This highly selective process by which a T cell is able to bind, recognise and react to only foreign antigens has been the focus of intense study due to its crucial importance in the adaptive immune response. The actin cytoskeleton is known to play an essential role in the formation and maintenance of the IS, but questions remain regarding the influence of forces generated by actin during this process. With the aim of measuring mechanical force generated at the IS, we present a novel method combining the super resolution imaging technique, Stimulated Emission Depletion (STED) microscopy and Traction Force Microscopy (TFM). Using the tunable kinetics of the 1G4 Jurkat T-cell system in combination with high spatial and temporal resolution microscopy we demonstrate that actin dynamics at the IS is antigen dependent and show by TFM that force generation occurs on two distinct time scales during activation, mediated by the actin cytoskeleton. Together, the results highlight the intimate links between the dynamics of the actin cytoskeleton, force generation and the antigen response of T cells during activation.

Table of Contents

List of Figures **ix**

List of Tables **xi**

Acronyms **xii**

1 Introduction **1**

2 Background **4**

2.1 The adaptive immune system 4

2.2 T cells in the adaptive immune response 5

2.2.1 TCR triggering 6

2.2.2 Signalling downstream of the TCR 8

2.2.3 Immunological synapse formation 11

2.3 Mechanical force in T-cell activation 13

2.3.1 Mechanical force in T-cell triggering 13

2.3.2 Mechanical force at the immunological synapse 15

2.3.3 The TCR is mechanosensitive 15

2.4 The cell cytoskeleton 16

2.4.1 The actin cytoskeleton 17

2.4.2 Cellular actin structures 18

2.5 Measuring mechanical force on the single cell level 19
2.5.1 Recent attempts to measure mechanical force during T -cell activation 24
2.6 Aims of the thesis 24

3 Materials and methods 25

3.1 Cell Lines 25
3.2 Cell culture 26
3.2.1 Cervical HeLa cells 26
3.2.2 Rat Basophilic Leukaemia cells 26
3.2.3 WT and 1G4-TCR Jurkat T cells 26
3.3 Transient transfections 27
3.3.1 Cervical HeLa cells 27
3.4 Transductions 28
3.4.1 Rat Basophilic Leukaemia cells 28
3.4.2 1G4-TCR Jurkat T cells 28
3.5 Protein production 29
3.6 Cell labelling 30
3.7 Drug treatments 31
3.8 Polyacrylamide gel fabrication 31
3.9 Polyacrylamide gel functionalisation 32
3.10 Cover-slip functionalisation 33
3.11 Protein biotinylation 34
3.12 Confocal microscopy 35
3.13 STED microscopy 36
3.14 Lattice-light sheet microscopy 36
3.15 High-NA Linear TIRF-SIM microscopy 38

3.16 Calcium response assay . . . 39
3.17 Quantification of actin retrograde flow . . . 40
3.17.1 Optical flow analysis . . . 41
3.17.2 Kymograph analysis . . . 41
3.18 Quantification of T-cell spreading . . . 42

4 STED-Traction Force Microscopy 43
4.1 Traction force microscopy . . . 43
4.2 Principles of Traction Force Microscopy . . . 46
4.2.1 Fourier Transform Traction Cytometry . . . 46
4.2.2 Regularisation . . . 48
4.2.3 Extracting the displacement field . . . 49
4.2.4 Improving TFM using STED . . . 53
4.3 Increased sampling density improves traction recovery . . . 55
4.4 STFM experimental optimisation . . . 62
4.5 STFM of HeLa cell focal adhesion . . . 64
4.6 STFM of RBL cell activation . . . 65
4.7 Summary . . . 69

5 T-cell force generation 71
5.1 1G4-TCR Jurkat T-cell calcium response is antigen dependent . . . 72
5.1.1 1G4-TCR Jurkat T-cell triggering is antigen dependent . . . 73
5.1.2 Actin spreading follows single calcium peak . . . 75
5.2 Global actin reorganisation during T-cell activation . . . 78
5.3 Actin retrograde flow velocity is antigen dependent . . . 80
5.4 Actin velocity distribution at the IS . . . 83
5.5 Force generation at the IS . . . 86

5.5.1 Polyacrylamide gel functionalisation 86
5.5.2 Gradual force generation 93
5.5.3 Load-fail dynamics 95
5.5.4 STFM load-fail dynamics 101
5.5.5 Load-fail dynamics is dependent on actin flow, but not myosin IIA 102
5.6 Summary 103

6 Discussion 108
6.1 Summary 108
6.2 Future work 112
6.3 DPhil Publications 115

References 117

Appendix A The Cerruti Problem 128

List of Figures

2.1 T-cell activation 7
2.2 Signalling downstream of the TCR 10
2.3 Immunological synapse formation 12

3.1 Validation of 1G4-TCR expression 30

4.1 Overview of TFM 44
4.2 TFM regularisation 50
4.3 Bead tracking method via SPT 52
4.4 STED and confocal bead density 57
4.5 STFM simulations 58
4.6 Comparing traction recovery using PIV and SPT 60
4.7 Microscope objective characterisation 63
4.8 STFM applied to HeLa cell focal adhesions 66
4.9 STFM applied to RBL cell activation 68

5.1 1G4-TCR kinetics 72
5.2 1G4-TCR Jurkat T-cell calcium release 74
5.3 Simultaneous actin and calcium response 76
5.4 Global actin reorganisation measured by LLSM 79
5.5 Actin retrograde flow velocity 82

5.6 Actin distribution and velocity measured by TIRF-SIM 85
5.7 Distribution of antigen on glass and Polyacrylamide (PAA) gel 87
5.8 Quantification of 1G4-TCR Jurkat T-cell spreading 88
5.9 Optimisation of 1G4-TCR Jurkat T-cell spreading 90
5.10 Surface protein distribution 91
5.11 Force induced by PLL and OKT3 94
5.12 Load-fail dynamics of 1G4-TCR Jurkat T-cells 97
5.13 Load-fail dynamics across all antigens 99
5.14 Load-fail dynamics of 1G4-TCR Jurkat T-cells measured by STFM . . 102
5.15 Jasplakinolide and Y27632 treatment during load-fail dynamics 104

A.1 The Cerruti problem 129
A.2 1D Cerruti problem 130

List of Tables

3.1 Table containing the concentration of bis-acrylamide and acrylamide and the corresponding gel stiffness 32

3.2 Quantification of protein biotinylation by the HABA assay 35

4.1 Comparing traction recovery using PIV and SPT 61

Acronyms

ADP Adenosine diphosphate. 18, 19

AFM Atomic Force Microscopy. 17, 22, 23, 47

APC Antigen Presenting Cell. 6–10, 12–15, 91, 94, 113, 117

APS ammonium persulfate. 33, 35

APTMS (3-aminopropyl)trimethoxysilane. 34

ATP Adenosine triphosphate. 18, 19

BFP biomembrane force probe. 17

BM Brillouin optical cell microscopy. 24

BSA Bovine Serum Albumin. 36

DMEM Dulbecco's Modified Eagle's Medium. 28–30

DTM Deviation of Traction Magnitude. 58, 63

ECM Extra Cellular Matrix. 66

ER endoplasmic reticulum. 10, 11, 74, 80

FBS Fetal Bovine Serum. 28–30

FRET Förster resonance energy transfer. 22, 47

FTTC Fourier Transform Traction Cytometry. 45, 57, 95

FWHM Full Width at Half Maximum. 59

HRP Horseradish peroxidase. 37

IS Immunological Synapse. 6, 12–16, 25, 47, 73, 74, 83, 86, 88, 91, 97, 100, 102, 105, 107–109, 112–117

ITAM immuno-receptor tyrosine-based activation motif. 7–9, 11

LLSM Lattice-light-sheet microscopy. 38, 74, 80–82, 107, 112, 113, 116

MEM Minimum Essential Media. 28–30

MHC Major Histocompatibility Complex. 6–8, 30, 31, 48, 113, 117

NHS N-Hydroxysuccinimidet. 36

OT Optical tweezer. 23

PAA Polyacrylamide. xiv, 21, 33, 34, 45–47, 59, 64–67, 88, 89, 91–95, 108, 115, 116

PBS Phosphate-buffered saline. 34–36

PDMS Poly(dimethylsiloxane). 22

PIV Particle Image Velocimetry. 54, 55, 61, 63, 67, 71, 95

pMHC Peptide bound Major Histocompatibility Complex. 6–10, 12, 14–17, 25, 31, 35, 36, 73, 74, 77, 80, 83, 85, 86, 95, 97, 100, 102

PSF Point Spread Function. 46, 56, 58, 61, 71, 116

PTM Particle tracking micro-rheology. 24

RBL Rat Basophilic Leukaemia. 27, 28, 30, 45, 69, 71, 111

SIM Structured Illumination Microscopy. 57, 85

SMAC Supramolecular Activation Complex. 13

SPT Single Particle Tracking. 51, 53, 54, 61, 71, 97, 99, 100, 104

STED Stimulated-Emission Depletion. 38, 45, 46, 48, 56–61, 63–67, 69, 71, 72, 104, 111, 112, 115, 116

STFM STED Traction Force Microscopy. 27, 29, 38, 56, 64, 67, 69, 71, 72, 103, 111, 112, 115, 116

TCR T-cell receptor. 6–17, 25, 30–32, 48, 73–75, 79, 80, 83, 85, 88, 95, 97, 98, 100, 102, 107–109, 112–114, 116

TEMED tetramethylethylenediamine. 33, 35

TFM Traction Force Microscopy. 21, 22, 25, 27, 28, 37, 45–49, 51, 55–57, 64, 66, 71, 74, 88, 91, 92, 103, 108, 111, 112, 114–117

UV ultra violet. 35

Chapter 1

Introduction

Mechanical force is a fundamental regulator of cellular function. Processes essential to life, such as cell migration and division, are intimately dependent on the cells ability to generate mechanical force.[1–3] Cells are also able to sense their mechanical environment, converting mechanical stimuli into biological responses. It is becoming increasingly clear that mechanical force is also important in T-cell activation, a key process in the adaptive immune response.[4]

Because of its vital role in protecting our bodies against invading pathogens and cancers, as well as its role in auto-immune disease, T-cell activation has been the subject of intense research. As a result, we now have a deep understanding of the intracellular signalling pathways that define activation.[5] However, much of this understanding has been gained from traditional biochemical methodologies, and it is only now that we are beginning to appreciate the biophysical aspects of T-cell activation. It has long been known that the actin cytoskeleton plays an indispensable role during activation, but the precise mechanism by which actin contributes towards activation remains unclear. Together with the motor protein, myosin, actin forms the primary force generating machinery within the cell. Given its key role in activation and its ability to

generate force, it remains a key question whether mechanical force generated by the actin cytoskeleton contributes towards T-cell activation.

In this thesis, I aim to investigate whether mechanical force generated by the actin cytoskeleton plays an active role in the formation and maintenance of the immunological synapse that forms between the T cell and antigen presenting cell during activation. To this end, I first focus on the utilisation of the methodology of traction force microscopy to measure the relevant forces. After characterising the distribution and dynamics of the actin cytoskeleton during activation, I then apply the tools developed to measure mechanical force within an engineered T-cell system.

The thesis is divided into this introduction and a further 5 chapters. Chapter 2 provides the necessary background of the biological processes important in this work. This includes a description of our current understanding of how T cells become activated, detailing the molecular events and signalling pathways involved. Owing to its importance in activation, I present a brief overview of the relevant concepts concerning the actin cytoskeleton, highlighting the key proteins as well as their organisation and regulation within the cell. Finally, I summarise the methods available to measure cell generated forces and describe how some have previously been applied to measure forces during T-cell activation.

In chapter 3, I outline the materials and methods used throughout the work. This includes a description of the cell lines, protein expression and labelling, genetic tools for fluorescence microscopy, as well as a description of the various microscopy modalities used.

In chapter 4, I focus on the development of a tool to measure the relevant forces. I first introduce the necessary theoretical concepts underpinning classical traction force microscopy, describing its limitations and how it can be improved using super-resolution optical Stimulated-Emission Depletion (STED) microscopy. As an initial

proof of concept, I demonstrate the potential improvement of combining the two techniques using computer simulations. I go on to demonstrate the improvements of STED traction force microscopy in two model biological systems, namely HeLa cell focal adhesions and in activating Rat Basophilic Leukaemia cells.

In chapter 5, I apply the tools and techniques acquired from chapter 4, to measure forces in an engineered 1G4-TCR Jurkat T-cell system. Before quantifying the mechanical force, I characterise the 1G4-TCR Jurkat T-cells antigen response using a calcium release assay. Following this, I present data acquired during visits to the The Howard Hughes Medical Institute (HHMI) at Janelia Farm Research Campus where I made use of two advanced microscopy modalities developed in the laboratory of Prof Eric Betzig to further our understanding of the dynamics of the actin cytoskeleton during activation. Lattice Light Sheet microscopy is employed to characterise the global actin rearrangements during activation, which is supported by TIRF-SIM to measure in detail the organisation and dynamics of actin at the immunological synapse. Further to this, the actin dynamics in response to different antigens is quantified. Lastly, after optimising the required experimental protocols, I apply traction force microscopy to quantify forces during T-cell activation, including measuring the antigen dependence of force generation.

Finally, in chapter 6, I summarise the results of the thesis and discuss possible future extensions to the work.

Chapter 2

Background

In this chapter, I present an introduction to the relevant biophysical and immunological concepts required for the understanding of the thesis. This includes a summary of the current knowledge of how T cells become activated in response to antigen stimulation. In doing so, I explain the molecular mechanism by which T-cell activation is initiated as well as the signalling pathways that lead to full activation of T cells. An outline is given of how mechanical force has been postulated to be playing a role in all stages of activation, with a focus on the role of the actin cytoskeleton. Finally, an overview is presented of the methods currently available to measure and probe mechanical force within living cells, as well as a summary of recent attempts to measure mechanical force during T-cell activation.

2.1 The adaptive immune system

The adaptive immune system provides vertebrates with the ability to defend against pathogens.[6] Unlike the innate immune system, which relies on general mechanisms to protect the body, the adaptive immune response can mount a pathogen specific

defence.[6] The adaptive immune response is mediated by a set of specialised cells known as lymphocytes. Lymphocytes can be broadly separated into those that induce an antibody-mediated response, known as B cells, and those that can carry out a cell-mediated response, known as T cells. In this work, I focus on the cell-mediated adaptive immune response, specifically the interaction that occurs between the T cell and the host cell presenting foreign antigens, known as the Antigen Presenting Cell (APC).[6]

2.2 T cells in the adaptive immune response

APCs, such as dendritic cells, process foreign invading material such as bacteria or viruses and present antigen peptides on their surface bound to a molecule known as the Major Histocompatibility Complex (MHC).[6] To initiate an immune response, the T cell and APC form a close cell-cell contact known as the Immunological Synapse (IS), during which the T cell must bind to and recognise whether the Peptide bound Major Histocompatibility Complex (pMHC) is bearing a self or foreign peptide (see Figure 2.1a).[7] This specificity is achieved via a molecule known as the T-cell receptor (TCR) expressed on the surface of the T cell. Following their formation in the bone marrow, T cells undergo a maturation process in the thymus, during which, T cells expressing TCRs with a high affinity for self peptides undergo specific negative selection leading to a population of T cells expressing TCRs with a high affinity for foreign peptides. On encountering an APC bearing a foreign antigen, T cells expressing a TCR specific for the given antigen will bind. If the TCR-pMHC affinity is sufficient, a complex signalling pathway is initiated leading to activation of the T cell. T cells can be subdivided into those that express the co-receptor CD4 and those that express CD8.[6] This surface expression determines the MHC molecule that the T cell will bind, with CD4 T cells binding to so called professional APCs expressing MHC-class II molecules, and CD8 T

cells binding cells expressing MHC-class I molecules. In each case, the effector function following activation will differ, with CD4 cells behaving as helper T cells, proliferating and releasing cytokines. CD8 cells, also referred to as cytotoxic T cells, directly kill cells that induce activation.[6,8,9]

T cells must be exquisitely sensitive in their antigen recognition. The overwhelming majority of peptides presented by APCs are self i.e. they are derived from the hosts body.[10] During maturation in the thymus, T cells with high affinity for self peptides are negatively selected, however, they will still weakly bind self antigens.[10] Thus, the T cell must be able to discern rare, strongly binding foreign antigens amongst a sea of weakly binding self antigens.

A critical first step in the activation response is the initial phosphorylation of the TCR complex, a process known as triggering. The TCR is present on the membrane of the resting T cells in complex with its co-receptor, CD3. Together they form what is referred to as the TCR complex. Because the TCR has no intrinsic kinase activity (unlike other receptors such as growth factor receptors[11]), it is dependant on other cooperating molecules to transduce a signal across the plasma membrane. Specifically, the phosphorylation of immuno-receptor tyrosine-based activation motifs (ITAMs) on the CD3γ, δ, ϵ and ζ chains by the tyrosine kinase Lck, and to some degree by Fyn, is responsible for initiating the signalling cascade downstream of the TCR complex that leads to full activation of T cells[5] (see Figure 2.1b). Tight control of this phosphorylation event is therefore crucial to the T cells ability to differentiate between foreign and self pMHCs.

2.2.1 TCR triggering

Despite significant research, the precise molecular mechanism by which information of the pMHC-TCR binding is translated across the plasma membrane remains controver-

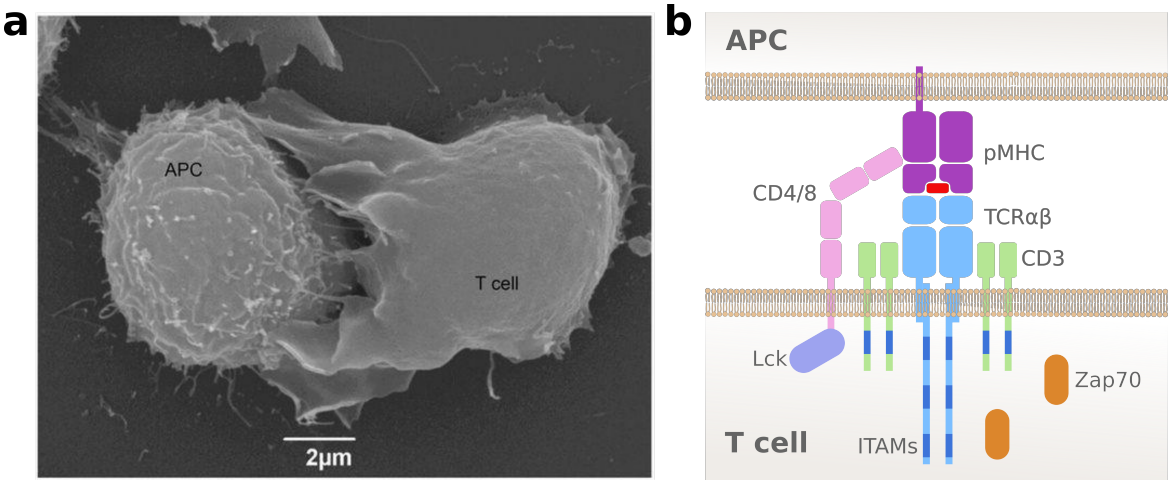


Fig. 2.1 T-cell activation - **a**) Scanning Electron Microscope (SEM) image of a T cell forming the close cell-cell contact with an APC known as the immunological synapse. Image reproduced with the permission of Oreste Acuto's laboratory, Sir William Dunn School of Pathology, University of Oxford. **b**) The TCR binds the pMHC on the APC membrane. Binding of the TCR-pMHC induces a signal across the plasma membrane, resulting in the phosphorylation of the CD3 ITAM domains by the tyrosine kinase Lck, triggering the TCR complex. Phosphorylation of the the ITAMs leads to binding of the molecule, Zap70, the first step in the cascade of intracellular signalling leading to full activation.

sial. A number of models have been proposed in an attempt to explain experimental observations. A summary of the models follows:[10]

TCR Aggregation

Binding of multimeric MHC molecules, as well as soluble antibodies specific for the TCR complex can induce triggering. The ability of these ligands to oligomerise the TCR is thought to be responsible for their efficacy in triggering, resulting from trans-autophosphorylation of the receptor complex.[12] However, under physiological conditions it is unclear how the extremely low density of pMHC found on the surface of the APC could induce such aggregation of the TCR complex.

Kinetic Segregation

In the resting state, the TCR complex is continuously phosphorylated by constitutively active membrane associated Lck.[13] To maintain the resting state of the cell, the phosphatase CD45 dephosphorylates the TCR complex, maintaining a net dephosphorylated

state. In the kinetic segregation model of TCR triggering the close membrane contact that develops between the APC and T cell is sufficient to exclude CD45, which has large ectodomains.[13,14] The spatial exclusion of CD45 leads to net phosphorylation of the TCR complex. The affinity of the TCR for its antigen determines the stability of the exclusion. If the TCR-pMHC interaction is sufficiently stable, the phosphorylated domains of the TCR will bind their substrates, preventing further dephosphorylation.[15]

Conformational change

A number of models have proposed triggering induced by conformational change of the TCR complex.[16,17] Ligand binding to the extracellular portion of the TCR is thought to induce a pulling force on the TCR complex, which in turn results in a conformational change in molecules forming the TCR complex, making its phosphorylation more likely. Recent evidence suggests that in the resting state, the ITAM domains are shielded from phosphorylation due to their charge based affinity for the plasma membrane.[18] A pulling force on the TCR complex, assuming a rigid structure, is thought to induce a piston like movement on the complex, leading to exposure of the ITAM domains from the plasma membrane, facilitating phosphorylation by Lck.

2.2.2 Signalling downstream of the TCR

Following phosphorylation of the ITAMs by Lck, a well characterised signalling cascade proceeds[6] (see Figure 2.2. The phosphorylated domains of the ITAMs serve as a binding site for Zap-70 (Syk-kinase zeta chain-associated protein of 70 kDa), via its tandem SH2 domains. After being phosphorylated by Lck, Zap-70 itself phosphorylates LAT (linker of activated T cells) which binds SLP-76 (SH2 domain containing leukocyte protein of 76kDa). LAT and SLP-76 serve as a scaffold for a number of key effector proteins. Phospholipase C-γ (PLC-γ) binds LAT where it is activated by Itk, allowing

it to hydrolyse the membrane lipid PIP_2 (Phosphatidylinositol 4,5-bisphosphate) to yield DAG (diacylglycerol) and IP_3 (Inositol trisphosphate). IP_3 binds to receptors on the endoplasmic reticulum (ER), releasing the secondary messenger, Ca^{2+}, into the cytoplasm.[19] The decreased concentration of Ca^{2+} in the ER is sensed by STIM1 (Stromal interaction molecule 1), which in turn activates Calcium release-activated channels (CRAC) on the plasma membrane, allowing external Ca^{2+} to enter then cell, sustaining the elevated levels of Ca^{2+} within the cytoplasm.[20] The elevated levels of Ca^{2+} activate the calcium sensitive enzyme, calcineurin, which in turn activates transcriptions factors such as NFAT (Nuclear factor of activated T-cells), leading to expression of proteins that induce the T-cell effector functions, such as Interleukin 2 (IL-2). The release of Ca^{2+} from the ER is commonly used as a marker for early T-cell activation[21,22]

Crucially, this signalling cascade interacts with key regulators of the actin cytoskeleton in numerous and complex ways.[23–25] SLP-76 serves as a scaffold for a number of actin regulators, including the Rho GTPases nucleotide exchange factor, Vav1, and the adaptor molecule Nck. Vav1 is a GEF (Guanine nucleotide exchange factor) that activates the GTPases Cdc42 and Rac1. Cdc42 and Rac1 then activate the actin regulators WASp (Wiskott-Aldrich syndrome protein) and WAVE2 respectively. Nck is an adapter protein that directly binds WASp, bringing WASp into contact with the GTPases Cdc42. WASp and WAVE2 activate the actin nucleation factor, Arp2/3, and present an actin monomer, allowing elongation of actin filaments to take place.[26] Cells deficient in WASp lack the ability to polymerise actin and individuals lacking WASp suffer from Wiskott-Aldrich syndrome (WAS), a severe immune deficiency disorder,[27] highlighting the importance of the actin cytoskeleton in T-cell activation.

Whilst the TCR-pMHC interaction is the central binding event during activation, there are a number of other molecular interactions that occur between the membranes

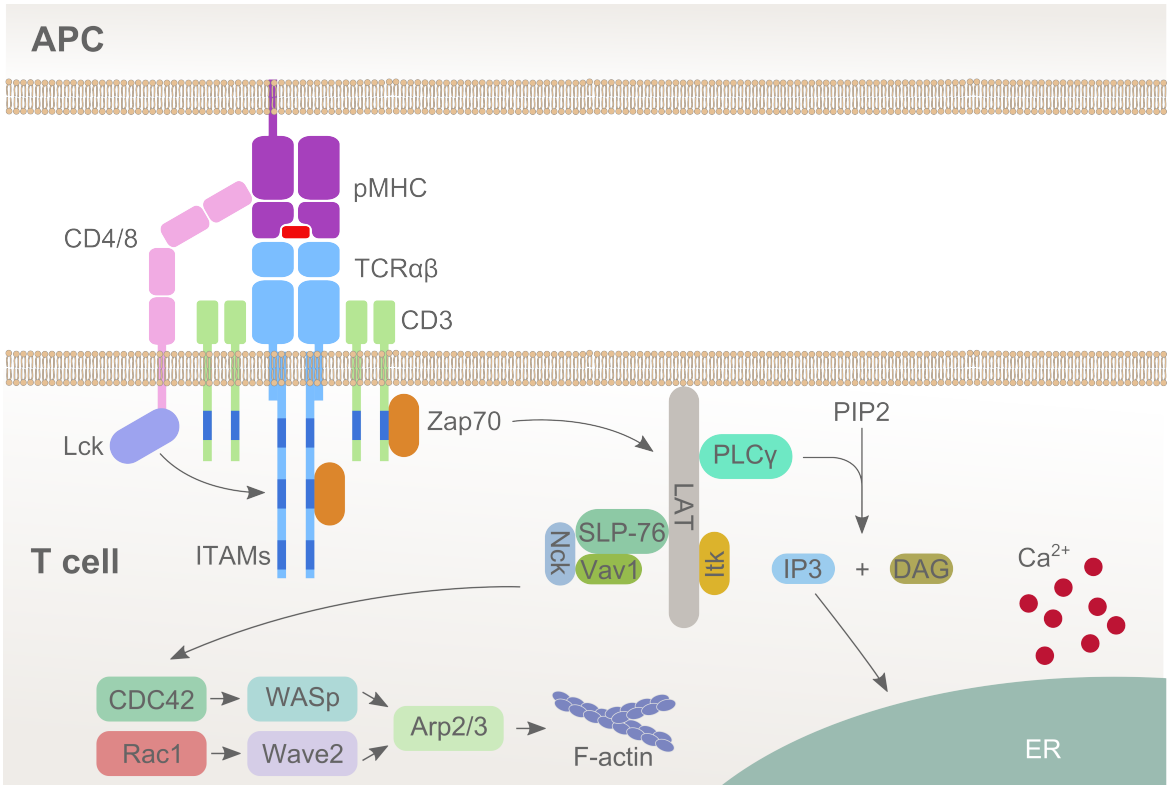


Fig. 2.2 Signalling downstream of the TCR - Following the initial triggering of the TCR complex, characterised by phosphorylation of the CD3 ITAM domains and subsequent binding of Zap70, signalling is propagated by recruitment of the scaffold proteins LAT and SLP-76. To this scaffold, PLC-γ binds, leading to hydrolysis of the membrane lipid PIP_2, forming IP_3, which lead to the release of Ca^{2+} from the ER. In addition to this, the scaffold binds Nck and Vav1, key regulators of the actin cytoskeleton. Vav1 activates Cdc42 and Rac1, leading to the activation and WASp and WAVE2, which in turn activates the actin nucleation factor Arp2/3 resulting in actin polymerisation.

of the T cell and the APC that contribute to activation. Owing to their small size of 15 nm, the interaction between the TCR and pMHC is unfavourable, given the extension and persistent repulsive force of the glycocalyx, a glycoprotein-polysaccharide coating which surrounds the cell.[28] Because of this, the initial contact between the T cell and APC is likely mediated by larger integrin molecules (40 nm), such as ICAM-1 (Intercellular Adhesion Molecule 1) expressed on the surface of the APC and its ligand LFA-1 (Lymphocyte function-associated antigen 1) present on the T-cell membrane.[15] Once a stable contact has formed, other molecules such as CD2, present on the T-cell membrane and its ligand, LFA-3, can interact, reducing the distance between the cell membranes, making the interaction of the TCR and pMHC more likely.

2.2.3 Immunological synapse formation

Following triggering of the TCR complex, the T cell undergoes a highly orchestrated series of morphological changes culminating in the formation of the IS (see Figure 2.3). Seconds after successful triggering of the TCR, the described signalling pathways lead to rapid polymerisation of actin filaments in a symmetric and coordinated manner outwards from the site of initial contact, increasing the contact area between the T cell and the APC.[23] The leading edge of the cytoskeletal protrusion contains a dense zone of actin undergoing retrograde flow, much like that which is observed at the leading edge of a migrating cell.[29] In contrast, the symmetric nature of the cell spreading means that all actin flow is directed towards the centre of the contact zone.

In studies conducted using lipid bilayers to mimic the membrane of the APC, micro-clusters containing TCRs as well as other signalling molecules form at the periphery of the contact.[30–32] The clusters are actively trafficked centripetally towards the centre of the IS where recent evidence suggests they are degraded.[33] The majority of the

active phosphorylation of the TCR occurs in micro-clusters at the periphery of the IS, co-localising with the zone of most dynamic actin.[34,35]

As the IS matures, molecules key to signalling become spatially segregated in concentric zones known as the central (c), peripheral (p) and distal (d), Supramolecular Activation Complex (SMAC). The cSMAC is characterised by high concentrations of immobile TCR, which have since been shown to be vesicles rich in TCR released by the cell.[33] The pSMAC contains high concentrations of the integrin LFA-1 which binds to the adhesion molecule ICAM-1, present on the bilayer. The outer region of the IS, referred to as the dSMAC, is rich in the phosphatase, CD45.

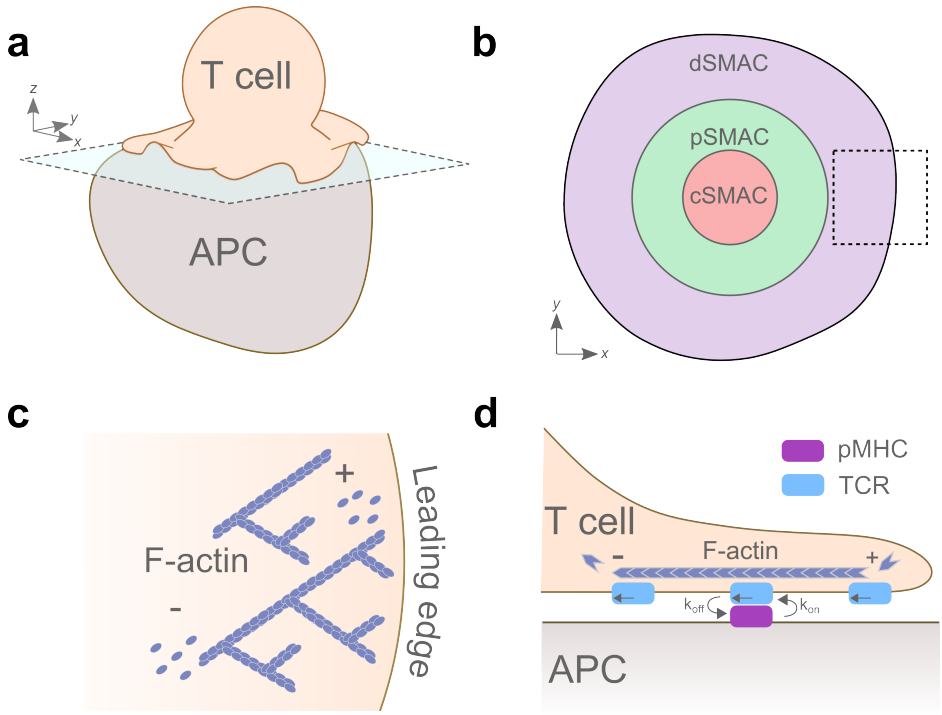


Fig. 2.3 Immunological synapse formation - **a**) Schematic outlining the 2D geometry of the interaction between the T cell and the APC which leads to the formation of the IS. **b**) The IS is characterised by molecular segregation into three distinct zones known as the the cSMAC, pSMAC and dSMAC. The cSMAC shows high concentrations of TCR, the pSMAC is rich in the integrin LFA-1 which binds to the adhesion molecule ICAM-1 and the outer dSMAC is rich in the phosphatase, CD45. **c**) The periphery of the IS (boxed region in **b**)) is characterised by a dynamic region of actin, resembling the lamellipodium of a migrating cell. The region contains a dense and branched meshwork of actin filaments which polymerises against the cell membrane, resulting in a net backwards motion of each actin monomer within the filament, referred to as actin retrograde flow. **b**) Micro-clusters containing TCRs and other signalling molecules form at the periphery and are actively trafficked towards the centre of the cell contact. The motion of the micro-clusters correlates with the retrograde flow of actin at the IS.

2.3 Mechanical force in T-cell activation

T cells are highly motile cells, navigating through a range of environments in search of target APCs. As a result, T cells are continually generating mechanical force as well and experiencing mechanical force from their surroundings. This is also true for the interaction between the T cell and the APC at the IS, where membrane receptors on both cells are inevitably subjected to mechanical force due to the adhesion and relative motion of the two membranes. Indeed, it has been shown that the kinetics of the TCR-pMHC interaction are significantly different when measured in solution, that is in the 3D case, compared to those values measured in the more physiological 2D case.[36,37] Forces imposed on the molecular interaction may be responsible for altering the observed TCR-pMHC kinetics.[38] This has led to speculation that mechanical force may play an active role during activation. The cytoskeleton provides the molecular machinery necessary for cells to actively generate force, thus understanding the role of the cytoskeleton during all stages of activation is of critical importance. It is known that a functional actin cytoskeleton is crucial for successful activation, but the question still remains whether actin plays a structural role, providing the right architecture to promote signalling or whether it is playing an active role, where its dynamics and hence force generating ability is crucial for activation. In this section, a summary is given of how force has been postulated to be playing a role in both triggering and signalling at the IS.

2.3.1 Mechanical force in T-cell triggering

As discussed, there are a number of TCR triggering models that rely on a conformational change of the receptor complex on ligand binding to induce triggering. It has been shown that soluble pMHCs fail to trigger the TCR, whilst surface bound pMHCs

do.[39] Hence, conformational change by binding alone is not sufficient. It has been postulated that forces generated by the actin cytoskeleton following binding of the TCR-pMHC provides the necessary force to induce a conformational change that initiates signalling. In support of this, T cells treated with cytoskeleton perturbing drugs such as Latrunculin A, which sequesters actin monomers, and Jasplakinolide, which stabilises actin filaments, show a diminished calcium flux[30] as well as diminished phosphorylation of PLC-γ.[40,41]

Models that rely on the spatial segregation of large phosphatases such as CD45 depend on the strength of the TCR-pMHC interaction to provide the necessary force to maintain a sufficiently stable zone of close cell-cell contact. However, considering the persistent repulsive force of the glycocalyx, this binding alone may be insufficient to induce the required close contact. It has been suggested that a protrusive force generated by the actin cytoskeleton normal to the cell-cell contact may aid in inducing the close contact. In support of this, it has been shown that T cells can produce actin-rich protrusive structures, know as invadosomes, directed towards the APC membrane during activation.[42]

Despite this evidence, there is an inevitable difficulty in invoking cytoskeletal generated forces to explain the initial triggering event since by definition at this early time point no specific signalling to the cytoskeleton has occurred via the TCR. This suggests that the initial triggering event must be either due to a passive mechanism, such as those outlined in the kinetic segregation model, or some signal prior to TCR engagement may prime the cell, allowing it to generate the suggested mechanical force. Considering this, we focus our attention on the role that mechanical force may be playing in the events that follow TCR triggering, specifically during the formation and maintenance of the IS.

2.3.2 Mechanical force at the immunological synapse

Following the initial triggering event, the rapid polymerisation of actin that characterises the formation of the IS will inevitably induce mechanical force on the membrane receptors present at the cell-cell contact. IS formation is also characterised by the trafficking of TCR micro-clusters from the periphery of the cell contact to the centre. This motion is known to be highly dependent on a functional cytoskeleton, suggesting that mechanical force generated by the actin cytoskeleton is responsible for the active transport of micro-clusters.[43,44] The transport of TCR clusters may be crucial in governing the length and time-scales on which the TCR is able to actively signal, thus forces generated by the actin cytoskeleton may modulate the strength of signalling at the IS. In addition to this, as previously mentioned, the majority of active TCR phosphorylation occurs at the periphery of the cell, coinciding with the zone of most dynamic actin. It is unclear if this occurs due to this being the zone in which the TCR and pMHC first make contact, or whether the forces generated by the actin cytoskeleton contribute to the level of phosphorylation via the mechanisms outlined in the previous section. Drug treatments show a dependence between actin dynamics and the continuation of signalling,[30,40,41] but the exact mechanism of this dependence remains unclear.

2.3.3 The TCR is mechanosensitive

Further evidence in support of an active role for mechanical force has come from a number of experiments that suggest that the TCR can behave as a mechanosensor. Typically, in such experiments an external force is applied to the TCR and an activation response measured, for example by Ca^{2+} release. Experiments using flow induced shear forces[45] and optical tweezers[46,47] have shown that application of force specifically via

the TCR can induce an activation response, suggesting that the TCR can translate mechanical force into a biological signal. More recently, Atomic Force Microscopy (AFM) experiments using cantilever tips functionalised with pMHCs induce elevated Ca^{2+} levels in response to a small mechanical force of 50 pN. The elevated levels of Ca^{2+} could not be induced by non-specific forces and had to be coupled through the TCR.[48,49]

Further to this, there is evidence that T cells take advantage of the forces present during this interaction to increase the sensitivity of the antigen discrimination. Using a biomembrane force probe (BFP), studies have shown that applying a small force to the TCR stabilises the TCR-pMHC interaction.[50] This is counter intuitive, as conventionally applying a mechanical force to a molecular interaction will decrease the stability, decreasing the half time of the bond.[38] However, this behaviour can be explained if the TCR-pMHC bond is considered to behave as a catch-bond, that is a bond that is stabilised under force. This has been postulated to enhance antigen discrimination, with weakly binding self antigens behaving as conventional slip-bonds, and foreign antigens behaving as catch-bonds.

2.4 The cell cytoskeleton

The T-cell cytoskeleton is known to be intimately involved in T-cell activation, thus I present here a brief introduction to the relevant concepts concerning the cytoskeleton.

The cytoskeleton is composed of the actin cortex located beneath the plasma membrane, the cytoplasmic actin network, inter-mediate filaments, and microtubules. Together they provide eukaryote cells with structural support and are crucial in controlling cell shape. In this work, we focus our attention on the actin cytoskeleton. Together with the motor protein, myosin, actin represents the cells primary force generating machinery, thus to understand how forces maybe contributing to T-cell

activation, it is of vital importance that we understand the mechanism by which the actin cytoskeleton is able to generate and regulate mechanical force within the cell.

2.4.1 The actin cytoskeleton

Actin is a 42 kDa protein of 375 amino acids expressed with high abundance in all eukaryotic cells.[51] Actin exists in two forms, a globular monomer known as G-actin and a filamentous polymer know as F-actin.[52] Each actin monomer contains an Adenosine triphosphate (ATP) binding site and its binding provides the necessary free energy to induce polymerisation.[53–55]

To form filaments, G-actin monomers bound to ATP must come together to form weakly binding dimers which can then be stabilised by the addition of a third monomer. Addition of further monomers to this nucleation site leads to rapid elongation into filaments. The initial nucleation is energetically unfavourable, and hence there exist actin nucleators which can greatly increase the efficiency of filament formation which will be discussed in the following section.

The structure of the actin monomers leads to a polarity in the growth of the filament. Polymerisation continues from both ends of the filament but is favoured at the so called barbed end (+) with the addition of monomers, where as de-polymerisation occurs more readily at the opposite end of the filament, known as the pointed end (-). At the critical concentration of actin monomers, the rate of polymerisation and de-polymerisation are equal and the filament has reached a steady state, with the monomers said to be undergoing a process of tread-milling. Upon polymerisation, the ATP bound to actin is hydrolysed to form Adenosine diphosphate (ADP), destabilising the filament. The protein cofilin can accelerate depolymerisation by severing existing filaments, where as the protein profilin can accelerate polymerisation by promoting

the exchange of the ADP to ATP of newly depolymerised actin, increasing the pool of freely available monomers.

Actin filaments can form spontaneously but as discussed this is energetically unfavourable. More commonly, filaments are formed with the aid of actin nucleators, such as Arp2/3 and formins which have recently been identified to be the only nucleators in the actin cortex.[56] Arp2/3 is a protein complex that can bind existing actin filaments at a distinct angle of 70 degrees.[57] Once bound, the Arp2/3 complex serves as a nucleation site for further actin polymerisation. Formins work at the barbed end, facilitating the addition of further actin monomers creating a filament.

2.4.2 Cellular actin structures

The actin cytoskeleton is organised into a number of distinct structures, some of which are persistent in time, such as the cortex, and some that are transitory such as the lamellipodium, membrane ruffles, micro villi and fillipodia. In this section, I outline the actin structures which are important in the T-cell activation, namely the cell cortex and the lamellipodium.

The cell cortex is a thin (100 nm) structure consisting of cross-linked actin filaments that forms a layer underneath the plasma membrane in the majority of eukaryotic cells.[58] The cortex is vital in maintaining cell shape and mechanical stability. In addition to this, there is evidence that the dynamic meshwork that characterises the cortex can influence the organisation of proteins at the plasma membrane.[59,60] The cortex is primarily linked to the membrane via proteins of the ERM family, ezrin, radixin, and moesin.[61]

During cell migration and in T cells during adaptive immune response, cells form a thin actin rich protrusion known as a lamellipodium.[62,63] Forces generated by polymerising actin filaments push on the plasma membrane resulting in a thin extension of the

cell which extends over the substrate.[64] The network of filaments is dense at the leading edge with polymerisation dominated by Arp2/3 mediated branching.[65,66] In migrating cells, the lamellipodium extends in the direction of movement, defining the front of the cell. As the lamellipodium extends outwards, adhesive contacts form between the cell and substrate known as focal adhesions. At the rear of the cell, myosin-II contraction results in a forward motion of the cell.[67] Further from the leading edge, a distinct actin structure emerges known as the lamellum. Here, the filaments become less branched and increase in length leading to a more course meshwork.[67,68]

In the lamellipodium, the tension of the plasma membrane provides an opposing force to those generated by polymerising actin. The net result is a retrograde flow of actin, where individual actin monomers within the actin filament move backwards relative to the leading edge of the cell.[29] The lamellipodium is a dynamic structure and can exhibit phases of extension, contraction and stability. Governing this dynamic behaviour is a complex balance between the rate of polymerisation, the tensions within the membrane and the strength of adhesion between the cell and substrate.[62]

2.5 Measuring mechanical force on the single cell level

Given the proposed importance of mechanical force in T-cell activation it is necessary to further our understanding of the forces present during activation. This means developing tools and techniques to quantify the relevant forces. To this end, I present a summary of the currently available tools to quantify and probe mechanical force as well as a summary of how some of these tools have been applied to measure forces in T cells.

Mechanical probing of living cells depends on the compliance and the length-scale of the biological material, the frequency (time-scale) at which mechanics is characterised, as well as on the environmental and experimental conditions. Hence, a myriad of experimental tools and theoretical models adapted from soft matter physics and engineering are now available to quantify cell mechanics including mechanical force generation and cell mechanical properties. Modern instruments are capable of probing and manipulating single cells and biomolecules at forces and displacements smaller than a piconewton ($1\,\mathrm{pN} = 10 \times 10^{-12}\,\mathrm{N}$) and a nanometre ($1\,\mathrm{nm} = 10 \times 10^{-9}\,\mathrm{m}$), respectively.[2] Here I briefly describe the principle, advantages, and drawbacks of each technique.

Traction Force Microscopy (TFM) is perhaps the most commonly used technique for examining mechanical force generation in cells, owing to the simplicity of its implementation on most laser-scanning confocal microscopes. In TFM experiments, a thin (20 µm to 30 µm) elastic gel is formed on a glass cover-slip onto which proteins facilitating cell adherence can be attached.[69] Within the gel, which are typically made from PAA, fluorescent beads serve as fiducial markers and imaging of the bead positions over time during the application of cellular tractions allows the displacement of the gel to be quantified. By combining the measured displacement field with knowledge of the mechanical properties of the gel, the tractions responsible for the displacements can be calculated. Notably, TFM is the ideal technique to investigate physiological interactions of cells within a two-dimensional geometry, because the PAA can be functionalised with the protein of interest. Fluorescently-labelled proteins on the gel or integrated within intracellular structures of cells can then be simultaneously monitored due to the multi-colour ability of confocal microscopes.[70]

An alternative approach to measuring traction forces involves the use of micro fabricated arrays of pillars made from an elastic material such as silicon or

Poly(dimethylsiloxane) (PDMS).[71] The tops of the pillars serve as contact points for the cell and can be functionalised using similar methods to those used in conventional TFM. By measuring the displacement of the top of each pillar, the force acting on it can be calculated, with each pillar behaving independently. The techniques can offer resolution comparable to TFM, however, the complex topology of such an assay is not applicable to all cell types, and the influence of such a topology on cell behaviour is unclear.[72]

Quantification of force generation within cells can also be achieved using Förster resonance energy transfer (FRET) based force sensors. FRET is a single molecule technique and relies on a donor fluorophore in an excited electronic state, which transfers its excitation energy to an acceptor fluorophore in a non-radiative fashion through long-range dipole-dipole interactions. FRET force sensors typically contain two fluorescent molecules coupled by a flexible linker which extends under mechanical load. The extension of the linker results in a measurable decrease in FRET signal between the two fluorophores.[73,74] These tools allow forces to be quantified on the single molecule level within living cells and have been successfully used to measure forces in focal adhesions as well as receptor-ligand interactions[75][76].[77] Recently, a FRET force sensor was combined with super-resolution localisation microscopy, giving a spatial resolution of 50 nm.[78] Whilst this is an exciting development in the field, currently, production of force sensitive FRET probes is challenging and requires in-depth biochemical knowledge of the specific biological system. Molecular probes of this type are also limited to measuring only the magnitude of forces, whereas TFM can measure both the magnitude and directionality.[79]

Other techniques focus on quantifying the mechanical properties of cells. AFM is a high-resolution surface characterisation technique that is predominantly applied for imaging and measurements of mechanical properties but also allow the mechanical prob-

ing of biological samples.[80] AFM measurements employ a micro-fabricated cantilever equipped with a micron-sized tip to deform and interact with the sample of interest. Specifically, force spectroscopy can be employed as a single molecule tool to characterise mechanical properties and active force generation by cells with sub-nanometre and pico-newton resolution.[1] Cellular elasticity and rheology are measured by pressing the cantilever tip against the cell surface while the imposed cellular deformation (and thus force) are monitored. Considering an appropriate contact model and the geometry of the cantilever tip, this yields information about measured force versus indentation from which the elasticity of the cell is computed.[81] Force generation can be quantified by functionalising the cantilever tip with integrins or protein binding agonists expressed on the cell surface.[48,82] Moreover, AFM allows time-dependent mechanical characterisation and oscillatory tests[83] in stress-relaxation and creep experiments.[84,85]

Optical tweezers (OTs) employ the concept of light trapping to mechanically manipulate, stretch, and move cells or particles.[86,87] OTs focus collimated light that enters a medium of different refractive index resulting in a restoring force towards the center of the beam created by the light passing through the material that resists higher levels of refraction. Typically, the applied forces are in the pico-newton range and allow spatio-temporal measurements at high accuracy of displacements in the nanometre range of objects ranging in size from 10 nm to over 100 mm.[88–90] Similarly to AFM, OTs have been used to quantify force generating processes and mechanical properties of cells.[91] For instance, the adhesion energy was measured between the plasma membrane and the actin cortex by pulling particles, attached to the cell membrane, away from the cell surface with the optical laser beam.[89,90] Instrumentation of OTs with high spatio-temporal precision and accuracy can no longer be built by modifying a standard optical microscope but rather require sophisticated devices under computer control. Additionally, although optical tweezers provide a valuable tool for high precision

measurements of small forces, they have an inherent limit on the amount of force that can be applied to cells without inducing local heating, affecting cell viability and the quality of force probing.

Particle tracking micro-rheology (PTM) relies on three-dimensional tracking of fluorescent particles embedded into intracellular structures of cytoskeleton components in the cytoplasm of cells. The particles can be cell membrane permeable or injected into the cells via micro-pipette aspiration.[92] Micro-rheological analysis of movement of the particles within cells report on the existence of Brownian fluctuations of free moving beads or directed motion of trapped beads. Indeed the movement of particles within the cell is perturbed by both elastic and viscous mechanical resistances.[93] Other possible contributions could include the influence of energy-consuming active processes and macro-molecular crowding on tracer particles inside the cytoplasm. Generally PTM experiments on cells reveal a dominant elastic response at high frequencies (short time-scales) and a more viscous behaviour on small frequencies (over longer time periods).[1] Instrumentation of PTM can be achieved on a standard light-field microscope but is limited by the ability to transport the beads to the location of interest.

One promising new method that overcomes such limitations is Brillouin optical cell microscopy (BM). BM measures intracellular and extracellular hydro mechanical properties of cells.[94] It is a label-free technique that does not require physical contact with cells and quantifies changes in light scattering due to cytoskeletal modulation and cell-volume regulation. Yet, this method is sensitive to the biomechanical changes in a cell caused by factors such as polymerisation, branching and liquid-solid volume fraction, and measures only relative changes in the elastic behaviour of cells. BM is a very promising new approach whose success still needs to be proven in the field of cell biology.

2.5.1 Recent attempts to measure mechanical force during T -cell activation

Given the mounting evidence that mechanical force plays an active during T-cell activation, it is vitally important that the forces present during activation are quantified. To date, a number of research groups have begun to address this problem, applying an array of techniques. In this work I also aim to measure the forces during activation, therefore the current research provides a valuable guide by which to compare the results of the work presented here.

Bashour *et al.* made use of a pillar based system to measure forces during activation, concluding that forces were transmitted via the TCR.[95] TFM has also been applied to measure the forces generated during activation.[96] The study by Hui *et al.* concluded that forces were generated in an actin dependent manner. More recently, FRET based forces probes attached to the TCR-pMHC have shown that the TCR does experience force during activation.[97]

2.6 Aims of the thesis

The aims of the thesis are two-fold. First, I aim to develop the tools and techniques required to measure forces at sufficient temporal and spatial resolution during T-cell activation. Next, I aim to apply these tools to measure the forces experienced by the TCR during the formation and maintenance of the IS. To add to our understanding of the parameters governing force generation, I will characterise the dynamics of the actin cytoskeleton at the IS, as well as investigating the effects of the TCR-pMHC kinetics using the 1G4-TCR system. To this end, I aim to improve our understanding of the mechanical forces present at the IS and how they may contribute to the formation and maintenance of the IS.

Chapter 3

Materials and methods

In this chapter, the materials and methods used throughout the work are presented. I introduce the cell lines, culture protocols and relevant biological techniques for the preparation of the experiments and their analysis.

3.1 Cell Lines

Throughout this work, three different cells lines were used, HeLa cervical cancer cells,[98] Rat Basophilic Leukaemia (RBL) cells[99] and Jurkat E6.1-57 T-cells.[100] HeLa cells were employed as a proof of principle for the STED Traction Force Microscopy (STFM) method, as they are a classic model system and have been well characterised in previous work using TFM. Rat Basophilic Leukaemia (RBL) cells were used as a model activation system of an immune cell during STFM validation. Jurkat T-cells were used as a model of an activating CD8+ T cell for all calcium response, actin cytoskeleton characterisation and TFM experiments.

3.2 Cell culture

3.2.1 Cervical HeLa cells

HeLa cells were cultured at 37 °C in 5 % CO_2 in Dulbecco's Modified Eagle's Medium (DMEM) (Sigma Aldrich, UK) containing 10 % Fetal Bovine Serum (FBS) (Sigma Aldrich), 1 % Penicillin Streptomycin (Sigma Aldrich) and 1 % L-glutamine (Sigma Aldrich). Cells were split every two days at a volume ratio of 1:5.

3.2.2 Rat Basophilic Leukaemia cells

RBL-2H3 clone cells (CRL-2256, ATCC, USA) were cultured at 37 °C in 5 % CO_2 in Minimum Essential Media (MEM) (Sigma Aldrich) containing 15 % FBS, 10 mM HEPES (Lonza, UK), 1 % Penicillin Streptomycin and 1 % L-glutamine. Cells were split every two days at a volume ratio of 1:5. 24 hours prior to TFM experiments, adherent cells were treated with 0.05 % Trypsin-EDTA (Lonza), facilitating their detachment from the cell culture flask. Cells were then transferred to a rotating chamber at 37 °C in 5 % CO_2 to maintain their suspensions state prior to the experiments.

3.2.3 WT and 1G4-TCR Jurkat T cells

All Jurkat T-cells were cultured at 37°C in 5% CO_2 in RPMI-1640 (Sigma Aldrich) containing 10% FBS, 1 % Penicillin Streptomycin, 1 % L-glutamine, 10 mM HEPES and 1 mM Sodium Pyruvate (Gibco, UK). Cells were split every two days at a volume ratio of 1:5.

3.3 Transient transfections

3.3.1 Cervical HeLa cells

Transient transfections were required in HeLa cells to induce the expression of fluorescent paxillin-EGFP, required for the localisation of focal adhesions during STFM measurements.

Prior to transfection, HeLa cells were plated on cover-slips in 6-well plates at 3 $\times$ 10^5 cells/ml, 2 ml/well in DMEM + 10% FBS. The paxillin-EGFP plasmid DNA was a kind gift of Dr Marco Fritzsche. For each cover-slip, 2 micro-centrifuge tubes were prepared, each containing 125 µL of Opti-MEM (Gibco). To the first tube, 1 µg of DNA was added followed by 5 µL of the P3000 transfection reagent (Invitrogen,UK). To the second tube, 4 µL of the L3000 reagent (Invitrogen) was added. Both solutions were left to equilibrate for 5 min. Following this, the two solutions were combined and allowed to stand for a further 20 min to allow the DNA and transfection reagent to form complexes. The mixture was then added to each cover-slip, pipetting slowly to distribute the solution evenly over the surface. After returning to the incubator for 4 h, the medium containing the DNA and transfection reagent was removed and replaced with fresh medium. Cells were then returned to the incubator for a further 12 h or overnight to allow for the expression of the fluorescent protein. Expression was validated using a bench-top inverted microscope equipped with a fluorescent lamp.

3.4 Transductions

3.4.1 Rat Basophilic Leukaemia cells

In collaboration with Dr James Felce of the Davis Laboratory (University of Oxford, UK), RBL cell lines stably expressing Lifeact-citrine were generated using a lentiviral transduction strategy. HEK-293T cells were plated in 6-well plates at 3×10^5 cells/ml, 2 ml/well in DMEM + 10% FBS. Cells were incubated at 37°C and 5% CO_2 for 24 hours before transfection with 0.5 μg/well each of the lentiviral packaging vectors p8.91 and pMD.G and the relevant pHR-SIN lentiviral expression vector using GeneJuice (Merck Millipore) as per the manufacturer's instructions. 48 h post transfection, the cell supernatant was harvested and filtered using a 45 µm Millex-GP syringe filter unit to remove detached HEK-293T cells. 3 mL of this virus-containing medium was added to 1.5×10^6 RBL cells in 3 mL supplemented RPMI-1640 medium. After 48 h, cells were moved into 10 mL supplemented MEM and passaged as normal.

3.4.2 1G4-TCR Jurkat T cells

In collaboration with Dr Veronica Chang of the Davis Laboratory (University of Oxford, UK) we set about to create a Jurkat T-cell line that expressed a single type of TCR. The 1G4-TCR is a well studied TCR that is specific for the tumour derived NY-ESO-$1_{157^{\sim}165}$ peptide (SLLMWITQC) in complex with the HLA-A2 (A2) MHC class I molecule. 1G4-TCR expressing T cells have been used in previous studies to assess the effects of peptide affinity on T-cell response.[101,102] To ensure that the T cell expressed only the specific 1G4-TCR, it was necessary to begin with a T cell deficient in both α and β chains of the TCR, which we received as a gift from Takamasa Ueno (University of Kumamoto, Japan). This cell line, referred to as type E6.1-57, was found

to express low levels of both the TCR β chain and the co-receptor, CD4. Because the 1G4-TCR binds the MHC class I molecule, the low levels of CD4 present in the cell line allows CD8 to be added subsequently, reconstituting the cytotoxic co-receptor. To this cell, deficient in both chains of the TCR we inserted both the α and β chains of the specific 1G4-TCR. The alpha chain and beta chain of 1G4-TCR were amplified from the cDNA that was a kind gift from Vincenzo Cerundolo (University of Oxford, UK) and the PCR products were ligated into the pHLsec vector below the sequence encoding the chicken RPTPσ signal peptide using AgeI and KpnI restriction sites.[103] The insert was then sub-cloned into the pHR vector.[101] Because the cell line expressed low levels of endogenous TCR β chain, insertion of the 1G4 α and β chains would result in expression of TCR containing pure 1G4 α and β chains as well as those expressing 1G4 α and endogenous β chains. Because both α and β chains must be present to allow presentation of the TCR at the membrane, only the 1G4 α was inserted and cells expressing TCR on the membrane were negatively selected via binding of anti-CD3 epsilon antibody (UCHT1), thereby removing the population of cells expressing endogenous TCR. This process was repeated two times until a pure population was established which was then inserted with 1G4 α and β chains. FACS plots showing the expression patterns of the engineered cell line are presented in Figure 3.1, which demonstrate that the cells expressed only the specific 1G4-TCR.

In addition to this expression of the 1G4-TCR, the cell line was transduced with actin-snap, Lifeact-citrine and CD8 by methods similar to those described above.[104,105]

3.5 Protein production

The pMHC molecules required to activate the IG4-TCR Jurkat T cells were produced in collaboration with Dr Veronica Chang of the Davis Laboratory (University of Oxford, UK). The MHC-Class I molecule is composed of HLA-A2 heavy chain and β2m

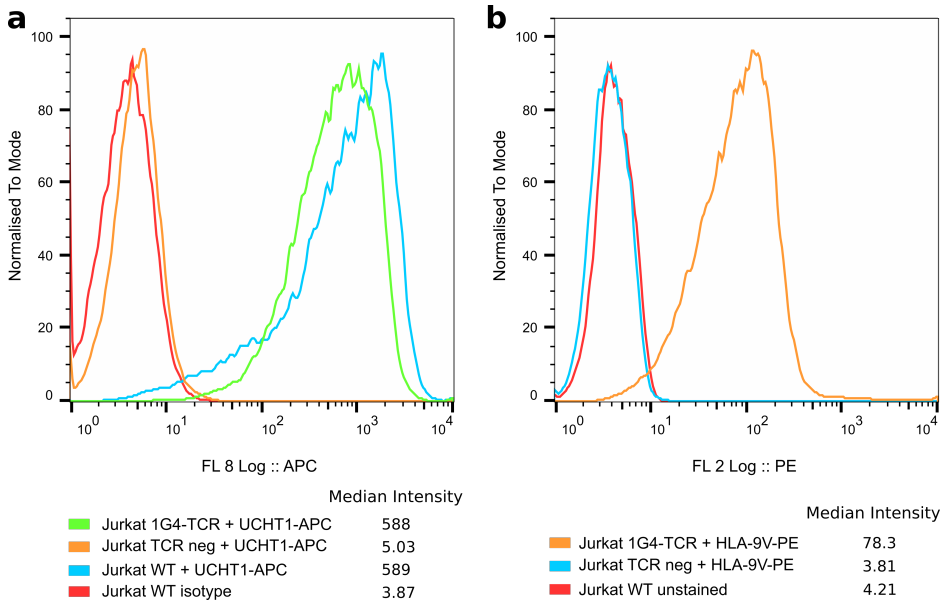


Fig. 3.1 Validation of 1G4-TCR expression - **a**) FACS plot showing the TCR expression of Jurkat T-cell expressing the 1G4-TCR compared to WT Jurkat expression. Expression is quantified via the binding of the APC labelled anti-CD3 antibody, UCHT1. The plot shows a comparable TCR expression between WT and 1G4-TCR T-cells. Additionally, it demonstrates that the cells that are TCR negative do not express any TCR. **b**) FACS plot showing the specific 1G4-TCR expression compared to WT Jurkat expression and Jurkat that contain no TCR. Expression is quantified via PE labelled HLA-9V tetrameters, demonstrating that only cells transduced with the 1G4-TCR are able to bind the HLA-9V molecule, unlike WT cells, and TCR negative cells.

light chain. The boundaries of the heavy and light chains to express were determined according to a published crystal structure PDB:1QRN.[106] Both the genes were amplified from cDNAs of the lab stock and cloned into pET28 vector (Clontech). The constructs were transformed and expressed in E. coli (strain Rosetts2 (DE3)pLysS) to make inclusion bodies, separately. Then the two inclusion bodies were mixed with peptide (either 9V - SLLMWITQV or 4D - SLLDWITQV) to refold. The refolded proteins were finally purified using size-exclusion chromatography to ensure the purity. All the purified proteins were aliquoted and fast frozen and kept at -80°C until usage.

3.6 Cell labelling

Cells were labelled using a variety of membrane permeable organic dyes coupled to SNAP ligands, including SNAP-Cell 505-Star, SNAP-Cell 647-SiR (NEB, USA).

Typically, 2 mL of confluent Jurkat T-cells were centrifuged at 1500 rpm for 1.5 min to form a pellet. The cell culture medium was discarded and the cells re-suspended in 200 µL of Leibovitz's L-15 Medium (ThermoFisher, UK). Dye was then added to the solution at a final concentration of 10 µM. The solution was then incubated at 37°C and agitated at 650 rpm for 30 min. Following incubation, cells were centrifuged and the medium discarded and replaced with a further 200 µL of fresh L15. Following a further 30 min incubation, cells were ready to use at the microscope. The labelling protocol was unchanged for all cell types and all dyes used through-out this work.

3.7 Drug treatments

Jasplakinolide (Thermo Fisher) is known to stabilise actin filaments.[107] It was used to investigate the role of actin retrograde flow during load-fail dynamics of 1G4-TCR Jurkat T cells at a concentration of 500 µM. Y27632 (Thermo Fisher) was used to investigate the role of myosin during the same load-fail events and was used at concentration of 100 µM. Both Jasplakinolide and Y27632 were added to the cells at the microscope. Because both drugs were first dissolved in DMSO (Dimethyl sulfoxide), controls were conducted where DMSO was added at the equivalent level to that present with the drug and no adverse effects were observed.

3.8 Polyacrylamide gel fabrication

PAA gel preparation has been adapted from.[108,109] Specifically, 40% acrylamide (Sigma Aldrich) and 2% bis-acrylamide (Sigma Aldrich) solutions were combined at a variety of concentrations depending on the stiffness required for the experiment (see Table 3.1). Polymerisation was initiated by adding ammonium persulfate (APS) (Sigma Aldrich) and tetramethylethylenediamine (TEMED) (Sigma Aldrich) at volume ratios

Table 3.1 Table containing the concentration of bis-acrylamide and acrylamide and the corresponding gel stiffness

Elastic Modulus (E) kPa	Acrylamide %	Bis-Acrylamide %
1	0.1	1
3	0.3	4
100	0.4	10
200	0.8	10

of 1:100 and 1:250, respectively. Once initiated, the gel solution was quickly pipetted between two cover-slips, forming a sandwich. Prior to forming the sandwich, the lower cover-slip was coated with a high density of fluorescent beads. To achieve a good coverage of fluorescent beads on the cover-slip, the glass was first acid cleaned and then coated with poly-L-lysine 0.01% (Sigma Aldrich) for 10 min. After washing and drying, a solution containing a high concentration of 40 nm red (594/620) fluorescent beads (Invitrogen) was placed onto the cover-slip for 10 min, followed by washing and drying. The top cover-slip was treated with 0.5 % (3-aminopropyl)trimethoxysilane (APTMS) (Sigma Aldrich) followed by treatment with 0.5 % glutaraldehyde (Sigma Aldrich) solution. This results in the silanisation of the glass surface which forms a covalent link with the polymerising gel, assuring firm attachment of the underside of the gel to the cover-slip. Once the sandwich was formed, the PAA gel was allowed to polymerise for 30 min at room temperature. Once complete, the top cover-slip was peeled off the gel, leaving a thin layer of gel on the activated surface. The PAA gel was then washed extensively in 100x vol/vol Phosphate-buffered saline (PBS) and stored at 4°C for no longer than 2 weeks.

3.9 Polyacrylamide gel functionalisation

PAA gel functionalisation was achieved by two different methods. One based on a biotin-streptavidin interaction and the other on the bi-functional cross-linker Sulfo-SANPAH

((sulfosuccinimidyl 6-(4'-azido-2'-nitrophenylamino)hexanoate) in combination with 365 nm ultra violet (UV) light.

For the first method, gels were fabricated using the previously described method (see Section 3.8), with the addition of streptavidin-acrylamide (Thermo Fisher) to the gel solution at a final concentration of 750 µg mL^{-1}. As the gel polymerises on addition of TEMED and APS the streptavidin-acrylamide is covalently incorporated into the meshwork of the gel leading to a distribution of biotin binding sites throughout the gel layer. After washing in PBS, the gel was placed on a drop of biotinylated protein solution, for example OKT3-biotin at a concentration of 100 µg mL^{-1}. Following 2 h incubation at room temperature, the gel was washed again in PBS and was then ready to use. Validation of protein coating was done via fluorescently labelled streptavidin (streptavidin-Alexa-488, Invitrogen) or in the case of antibody coating via a secondary antibody (goat-anti mouse IgG Oregon-Green, Invitrogen).

Alternatively, gels were functionalised using Sulfo-SANPAH. Gels were again fabricated as previously described (see Section 3.8). Once polymerised, the gels were coated with a 5 mg mL^{-1} solution of Sulfo-SANPAH and exposed to UV light at 365 nm for 10 min. Following this, the gel was extensively washed in PBS, ensuring all unbound cross-linker was removed. The gel was then placed on a drop of protein solution, fibronectin or poly-L-lysine, at a concentration of 1 mg mL^{-1} and incubated at 4 °C for 12 h. Following incubation, the gel was washed in PBS. At this point the gel could be used or in the case of poly-L-lysine coating, was incubated again with a secondary protein e.g. OKT3, at a concentration of 100 µg mL^{-1}.

3.10 Cover-slip functionalisation

Glass cover-slips functionalised with both antibodies and pMHCs were required for actin velocity quantification in both confocal and TIRF-SIM and for the calcium

response assay. For each of these experiments, the cover-slips were prepared using the same protocol.

18 mm, #1.5 cover-slips (Scientific Laboratory Supplies, UK) were first sterilised by extensive washing in ethanol. After drying, cover-slips were coated with 20 µL of a 1:4 mix of biotinylated Bovine Serum Albumin (BSA) (Sigma Aldrich) and standard BSA (Sigma Aldrich) at concentrations of 200 µg mL^{-1} and 800 µg mL^{-1} respectively, followed by incubation at room temperature for 2 h. After washing 3 times in PBS, cover-slips were coated with 20 µL of a 10 µg mL^{-1} solution of streptavidin (Sigma Aldrich) followed by a further 2 h incubation. After washing, 20 µL of a 10 µg mL^{-1} solution containing either the biotinylated antibodies, OKT3 or UCHT1, or the biotinylated pMHC, HLA-9V and HLA-4D was placed on each cover-slip as required, followed by a further incubation 2 h and washing. Note, that for negative control cover-slips, the final step was omitted.

3.11 Protein biotinylation

Protein biotinylation was required to specifically functionalise both the gel and glass surfaces. To achieve biotinylation, an N-Hydroxysuccinimidet (NHS)-ester labelling method was used that targets amine groups typically found on free lysines within the protein. All proteins to be biotinylated were first passed through a desalting column (7K Zeba Spin, ThermoFisher) to remove any buffer components that may interfere with the biotinylation reaction (e.g. Tris). The reaction was conducted in a volume of 200 µL and a protein concentration of 1 mg mL^{-1}. The pH of the solution was adjusted to pH 8 using a 1 M solution of NaOH. Biotin-NHS (EZ-Link, ThermoFisher) was added to the protein solution at a molar ratio of 10:1 and incubated for 1 h at 37 °C. Following incubation, the solution was passed through a further desalting column to remove any unbound biotin.

Table 3.2 Quantification of protein biotinylation by the HABA assay

Protein	Mole Biotin / Mole Protein
OKT3	7.7
UCHT1	1.7
HLA-9V	1.4
HLA-4D	0.9
HRP control	0.9

For each biotinylation reaction the HABA (4'-hydroxyazobenzene-2-carboxylic acid) assay was performed to insure the reaction had been successful and to quantify the level of biotin on each protein.[110,111] Table 3.2 shows the level of biotinylation of each protein compared to the control of Horseradish peroxidase (HRP), which contained 1 mole of biotin per mole protein.

3.12 Confocal microscopy

All actin dynamics measurements were performed on a Leica TCS SP8 3X microscope (Leica, Mannheim, Germany) using the Leica HC PL APO 100x/1.4 Oil STED WHITE objective. For cells labelled with the fluorescent protein citrine, or the cell permeable organic dye SNAP-Cell 505-Star, 488 nm excitation light was used and fluorescence emission was collected at around 530 nm. All conventional TFM experiments were performed on the same system using a Leica HC PL APO 63x/1.2 Water motCORR CS2 objective. For the TFM experiments red fluorescent beads were excited using 594 nm light, and fluorescence emission was collected at around 620 nm. All images were acquired on the Leica HyD detectors.

Calcium quantification experiments were carried out on a spinning disk confocal microscope combined with a 10x objective. The lower magnification objective allowed a large field of view of 700 µm x 700 µm as a trade-off for lower resolution. The calcium sensitive dye Fluo-4 AM (ThermoFisher) was excited at 488 nm. For simultaneous actin

and calcium measurements, a 20x objective was used to allow sufficient resolution of actin structures. Cells were labelled with Fluo-4 AM and SNAP-Cell 647-SiR, excited at 488 nm and 640 nm respectively.

3.13 STED microscopy

All Stimulated-Emission Depletion (STED) microscopy performed for STFM was carried out on a Leica TCS SP8 3X microscope. All live-cell experiments were done at 37°C and 5 % CO_2. The microscope was equipped with a pulsed super-continuum white-light laser (WLL, Koheras SuperK, 80 MHz) for excitation and a 660 nm 1.5 W CW STED depletion laser. SNAP-Cell 505-Star labelled G-actin was excited at 488 nm, and fluorescence emission was collected at around 530 nm. For STED imaging of the fluorescent beads, excitation laser intensities of 1-5 % of the 594 nm WLL and 30-100 % of the 660 nm STED laser and fluorescence emission was collected at around 620 nm. Laser powers were chosen to obtain a strong enough fluorescence signal as well as sufficient improvement in spatial resolution, and images were acquired at 1-5 s intervals to minimize loss of fluorescence due to photo-bleaching as well as cell phototoxic effects (of which we did not observe any in the recordings). All images were acquired on the Leica HyD detectors using time-gated detection with a time gate of 10-15 ns.[112]

3.14 Lattice-light sheet microscopy

Lattice-light-sheet microscopy (LLSM) was performed at the Advanced Imaging Centre, HHMI Janelia Research Campus, VA in collaboration with the laboratory of Prof. Eric Betzig. A 2D-array of non-diffracting Bessel beams is used to illuminate the specimen at a single plane whilst a second objective placed at the focal plane of the illumination captures the fluorescent light. To collect multiple planes, the sample is

scanned through the light sheet, and fluorescence emission collected from each frame. For a full description of the microscopy set-up see.[113]

For the Jurkat T-cell activation experiments, a 5 mm glass cover-slip (# 1 thickness, Warner Instruments, Camden, CT, USA) was mounted and secured in a custom-made steel holder attached to a xyz-piezo stage (Physik Instrumente, Karlsruhe, Germany). Fluorescently tagged Jurkat T-Cells were dispensed above the cover-slip into the media bath containing Leibovitz's L-15 medium warmed to 37 °C and in an atmosphere of 5 % CO_2. Once a cell of interest was within the focal plane of the light sheet the sample was laterally scanned through the light sheet. The total scan distance ranged from 0 µm to 15 µm at 10 ms to 40 ms exposure. Emitted photons were collected from the single excitation plane by a 1.1 NA 25x water-dipping objective (Nikon, Tokyo, Japan) and recorded on an Orca Flash 4.0 V2 sCMOS camera (Hamamatsu, Shizuoka, Japan). Cells were excited by either 488 nm nm or 560 nm wavelength laser light at [1-5 %] AOTF transmittance of [300 and 500 mW] laser power (MPB Communications, Quebec, Canada).

Following data acquisition, all images were de-skewed to correct for the 31.8 °angle of the detection objective relative to the vertical axis of the sample and run through multiple iterations of a Richardson-Lucy deconvolution algorithm. Volumetric rendering and 4D visualization was done using Amira 3D Software for Life Sciences (FEI, Oregon, USA).

Cell contact area and perimeter measurements were performed using custom-written MATLAB routines making use of the MATLAB macro 'imbinarize' to segmented each frame.

3.15 High-NA Linear TIRF-SIM microscopy

High-NA (high-numerical-aperture) eTIRF-SIM (extended total-internal-reflection-fluorescence structured-illumination-microscopy) was carried out in the lab of Prof Eric Beztrig at the HHMI Janelia Research Campus, VA using a system described in.[114] A 488 nm (Coherent, SAPPHIRE 488-500) laser (MPB Communications, 2RU-VFL-P-1000-560-B1R) was then passed through an acousto-optic tunable filter (AOTF, AA Quanta Tech, AOTFnC-400.650-TN). The beam is then expanded and sent into a phase-only modulator, which consisted of a polarization beam splitter, a achromatic half-wave plate (HWP, Bolder Vision Optik, BVO AHWP3), and a ferroelectric spatial light modulator (SLM, Forth Dimension Displays, SXGA-3DM). Light diffracted by the grating pattern displayed on SLM passes through a polarization rotator, composed of a liquid crystal variable retarder (LC, Meadowlark, SWIFT) and an achromatic quarter-wave plate (QWP, Bolder Vision Optik, BVO AQWP3), which can rotate the linear polarization orientation of the diffracted light for different wavelengths to maintain the s-polarization, thereby, maximize the pattern contrast for all pattern orientation. The desired light of ± 1 diffraction order was purified from all other high order diffraction light by a hollow barrel mask driven by a galvanometric scanner (Cambridge Technology, 6230HB), then they were imaged onto the back focal plane of the high-NA objective (Olympus Plan-Apochromat 100X Oil-HI 1.57NA) as two spots at opposite sides of the pupil. After collimated by the objective, the two beams interfered at the interface between cover-slip and the sample at an intersection angle larger than the critical angle for total internal reflection. The generated evanescent standing wave of excitation intensity axially penetrated ~ 100 nm into the sample, and was laterally modulated as a sinusoidal pattern that was a low-pass filtered and demagnified image of the grating pattern displayed on the SLM. The resulting fluorescence was collected by the

same objective, and separated from excitation light by a dichroic mirror, and finally imaged onto a sCMOS camera (Hamamatsu, Orca Flash 4.0 v2 sCMOS), where the structured fluorescence raw data were recorded. The cell samples were imaged inside a micro-incubator (H301, okolabs, Naples, Italy) maintaining the physiology conditions of 37 °C and in an atmosphere of 5 % CO_2 .

For each time point, 3 raw images were acquired at successive phase steps of 0, 1/3 and 2/3 of a period of the sinusoidal illumination pattern. This process was then repeated with the sinusoidal excitation pattern rotated by +120 °or -120 °with respect to the first orientation. Since the excitation pattern was conjugated to the grating image displayed on SLM, the phase stepping and pattern rotation could be accomplished by translating and rotating the grating image accordingly. A total of 9 raw images was acquired for a single excitation wavelength before switched to the next, and then repeated this acquisition procedure for each time point. T cell images were recorded every 50 ms, with a total cycle time of 3 s. Finally, the raw images were processed and reconstructed into SIM images by a previously described algorithm.[115]

3.16 Calcium response assay

To measure the calcium release upon T-cell triggering an assay was developed that would allow the simultaneous acquisition of single cell calcium intensity profiles for hundreds of cells at a time. Calcium response data was acquired using a spinning disk confocal microscope equip with a 10x NA=0.45 objective (Carl Zeiss AG, Overkochen, Germany) leading to a field of view of 700 µm x 700 µm. 1G4-TCR Jurkat T-cells were labelled with 4 µM of the calcium sensitive dye Fluo-4 AM (F-14201; Invitrogen) for 10 min at room temperature with 2.5 µM probenecid (P-36400; Invitrogen) in Leibovitz's L-15 medium. Cells were then washed in HBS (51558; Sigma, UK) and

medium changed to HBS containing 2.5 µM probenecid before adding to antigen coated slides. Images were recorded every 750 ms for 12.5 min using 488 nm excitation.

For experiments visualising actin as well as calcium, prior to the Fluo-4 AM labelling described above, 1G4-TCR Jurkat T-cells were labelled SNAP-Cell 647-SiR as described previously (see 3.6)

A suite of MATLAB routines known as CalQuo was written to extract, quantify and filter the calcium response profile for each cell in the time series.[116] The image stacks containing the calcium flux time-lapses are first loaded in to the software. Using a feature recognition algorithm to locate the cell coordinates each cell is coarsely segmented from the raw image.[117] Further refined segmentation to locate the cell edge is done using a level-set algorithm.[118] Once fully segmented, each cells intensity in each frame is calculated and plotted. This fluorescence intensity time trace represents the calcium flux within the cell throughout the image sequence. Next the intensity profiles are filtered into those cells that show a triggering response, indicated by a sharp rise in the fluorescence intensity, and those that remain un-triggered with their intensity at background levels. Statistics, such as the triggering time and peak width are then output by the algorithm. A detailed description of the CalQuo analysis algorithms are presented in the supplementary materials section of.[116]

3.17 Quantification of actin retrograde flow

Velocity quantification of T-cell retrograde flow measured by confocal and TIRF-SIM microscopy was analysed using two methods: Optical flow analysis and kymograph analysis.

3.17.1 Optical flow analysis

Optical flow is technique commonly used in computer vision to establish the movement between video frames. Here, we apply optical flow to measure to velocity displacement of actin between frames of time-lapse imaging. To establish the flow velocity for each cell, we first find the optical flow between each frame using a pre-implemented MATLAB algorithm.[119] This results in a displacement map linking the position of each pixel between frames. By dividing the displacement by the frame acquisition time, we achieve the actin flow velocity between each frame. This was done for all frames of the time-lapse and the results plotted in a histogram. To quantify the magnitude of flow in the lamellipodium, an area in the fluorescence image corresponding to the lamellipodium is manually segmented, followed by the plotting of a histogram containing all the velocity values from within the segmented region. A Gaussian fit in then applied to the histogram, the mean of which represents the average lamellipodial actin flow for the given cell.

3.17.2 Kymograph analysis

Kymograph analysis provides a straight forward method of assessing the flow within a time-lapse fluorescence image. For each time-lapse, a kymograph was was plotted derived from a line profile dissecting the T cell contact area. A line was then drawn which coincided with the movement of a feature within the time-lapse. In a kymograph, a feature moving at a constant velocity will appear as a diagonal line, the gradient of which represents the velocity, with steeper gradient representing slower moving features. For each cell, a minimum of three kymographs were plotted and gradient of features in the lamellipodium calculated.

3.18 Quantification of T-cell spreading

The contact area of T cells expressing fluorescently labelled actin was used a marker for activation. Confocal images of T cells on a range of surfaces were recorded 10 min after depositing of cell on the cover-slip, ensuring T cells had sufficient time to spread. Images were recorded using confocal microscopy allowing a large field of view (200 µm x 200 µm) providing adequate cell numbers. To assess the contact area of each cell, using a custom-written MATLAB routine, the image was first blurred using a Gaussian filter to remove unwanted background noise. The image was then converted into a binary image, using the pre-implemented MATLAB function, 'imbinarize'. The area of each region in the binary image corresponding to a cell was then extracted and quantified.

Chapter 4

STED-Traction Force Microscopy

In this chapter, I introduce TFM and present developments to the method with the aim of quantifying mechanical force during T-cell activation. First, I present an overview of the mathematical background to TFM, outlining the key concepts, including Fourier Transform Traction Cytometry (FTTC) and the quantification of bead displacements. Next, I discuss the advantages and limitations of classical TFM and explain how it can be improved using STED microscopy. This improvement is then demonstrated by computer simulations, followed by two biological examples of HeLa cell focal adhesions and an activating RBL cell system.

4.1 Traction force microscopy

Beginning with the pioneering work of Harris *et al.*, flexible substrates have been used to investigate cellular forces for over 30 years.[120] In a typical TFM experiment, a thin (30 µm) layer of linearly elastic, homogeneous and isotropic gel material, such as PAA is formed on a glass cover-slip, within which fluorescent beads are placed that serve as spatial markers. The top surface of the gel is functionalised with proteins that either

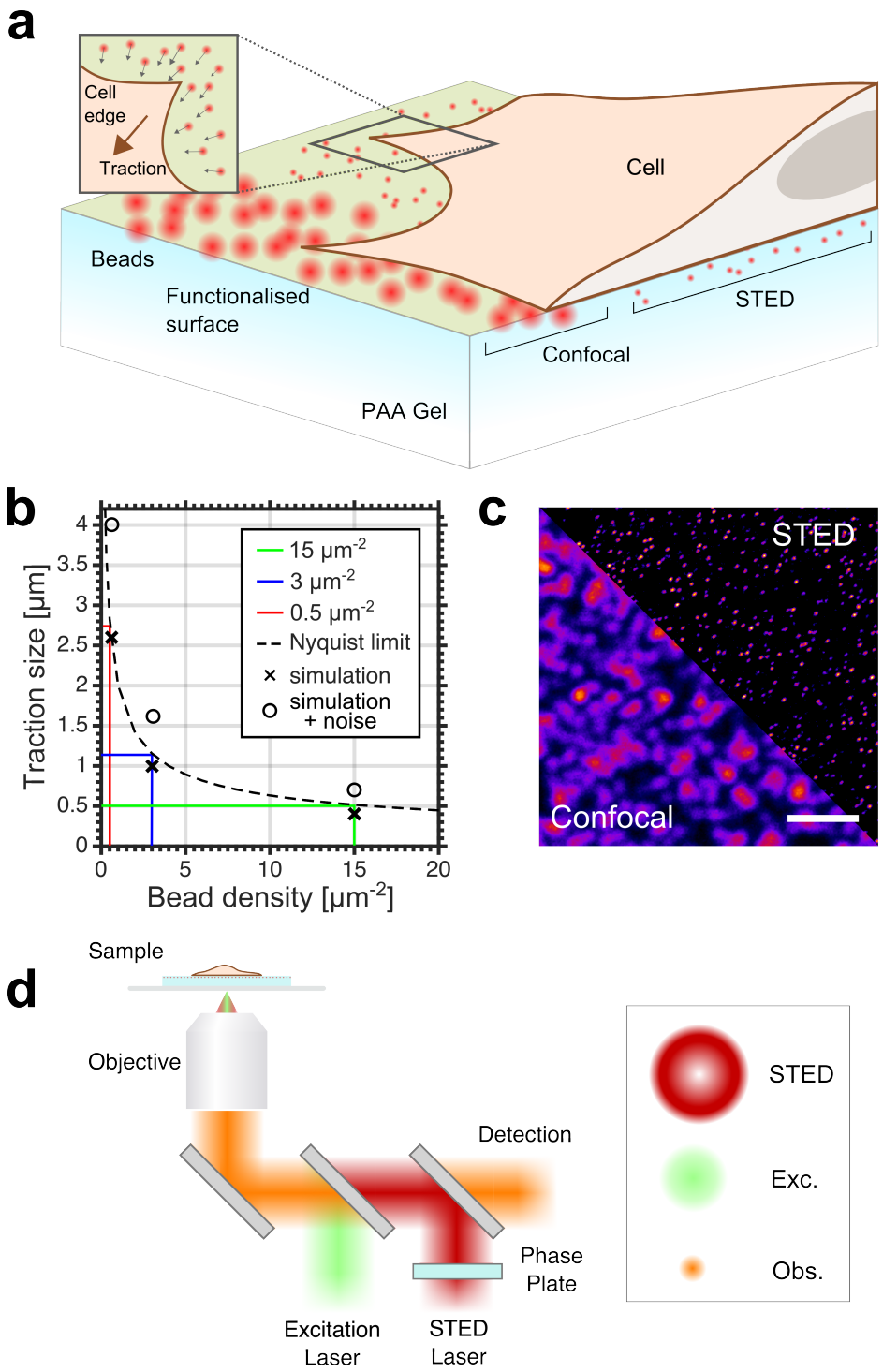


Fig. 4.1 Overview of TFM - **a**) Diagram showing a typical TFM experiment, where a PAA gel is formed on a glass cover-slip and functionalised with proteins that facilitate cell attachment. Within the gel, fluorescent beads serve as spatial markers, reporting on lateral displacement of the gel due to tangential forces at the upper surface of the gel. **b**) Theoretical relationship between the bead sampling density and the Nyquist limit of feature detection within the traction field (dashed line), with three different bead densities highlighted (red, blue, green as labelled), exemplifying that a bead density of 15 µm^{-2} would allow the recovery of tractions 500 nm in size. Crosses show the smallest recoverable tractions from simulations performed at the three bead densities shown in Figure 4.5. Open circles show the smallest recoverable traction from simulations where noise is added and regularisation used. **c**) Distribution of red 40 nm fluorescent beads imaged at a depth of 30 µm at the top surface of the gel in confocal and STED. Scale bar is 2 µm. **d**) A schematic representation of a STED microscope. A conventional confocal microscope is modified with the addition of a depletion laser. The doughnut shaped depletion laser leads to a reduction is the observed size of the Point Spread Function (PSF), resulting in a higher resolution fluorescence image.

facilitate cell adherence or stimulate cell spreading, for example fibronectin (see Figure 4.1a). Any forces generated by the cell will be transferred to the PAA gel via the protein coupling, resulting in the displacement of the gel and hence the displacement of the fluorescent beads immobilised within the gel meshwork. The bead displacements during the application of force are typically recorded by time-lapse confocal imaging. Because the gel material can be considered to undergo a linear elastic response, the displacement can be combined with the mechanical properties of the gel, specifically its elastic modulus and poisson ratio, to calculate the force per unit area or pascals ($1\,\mathrm{Pa} = 1\,\mathrm{N\,m^{-2}}$) responsible for the measured displacement.

To date, TFM has been used to measure force generation in a number of important cellular processes, including adhesion and migration.[121] There are a number of key features of TFM that make it a tool well suited to measure forces generated by T cells during activation, offering advantages over other methods. In its classical form, TFM is able to measure forces across the whole cell contact area simultaneously. This is in contrast to techniques such as optical tweezers or AFM, which only measure forces at a single point. Crucially, this means that TFM is compatible with the 2D geometry of the cell-cell interaction that defines the IS. Furthermore, TFM is able to report on the directionality and magnitude of the force, unlike other methods which can only give the magnitude of the force, for example FRET tensions sensors. Because of the widespread use of PAA, various surface chemistry and protein conjugation techniques can be used to straight forwardly functionalise the gel surface with almost any protein of interest.

Despite its suitability, there are a number of disadvantages to TFM in its classical form. TFM does not have molecular specificity, for example, if a number of different proteins are used to functionalise the gel, the relative contribution of each protein interaction to force generation will be unknown, unless they can be separated temporally.

In addition to this, classical TFM is limited to measuring forces on the micron scale.[122] Since it is well known that cellular forces are operating on the nano-meter and pico Newton scale, there is a pressing need to extend this well established technique to tackle questions at nano scale force regimes such as the mechanical force transmitted through individual TCR micro-clusters to MHC complexes during T-cell activation. In the following I extend the discussion of what limits the accuracy of classical TFM and introduce STED microscopy as a means of addressing these limitations.

4.2 Principles of Traction Force Microscopy

4.2.1 Fourier Transform Traction Cytometry

By measuring the lateral displacements of fluorescent beads placed within an elastic gel, TFM allows any tangential forces applied to the gel to be recovered. Mathematically, the gel is defined as an elastic half-space, meaning it is considered to be a plane, infinite in all three spatial dimensions.[123] In practice, the gel is of finite thickness and is attached to a cover-slip such that it can be imaged from below. For the half-space assumption to hold, the gel must be sufficiently thick such that any forces applied to the upper surface of the gel are not influenced by the rigid lower surface at the cover-slip. In practice, this means the gel can be no thinner than 20 µm-30 µm and all displacements must be kept below 1 µm.[124] It is also assumed that the direction of forces are limited to the plane of the gel and forces normal to the gel are considered negligible. By imaging the beads before and after a force has been applied, the displacement of each bead can be extracted, providing a displacement field, $\mathbf{u}(\mathbf{x})$, across the extent (two-dimensional space $\mathbf{x}$) of the substrate-cell interface. The traction field, $\mathbf{T}(\mathbf{x})$, and displacement field, $\mathbf{u}(\mathbf{x})$, are related via a convolution with the so called Green's function, $\mathbb{G}$ (Equation 4.1 and 4.2). The Green's function is a tensor which maps the

traction field to the spatial distribution of the displacements and is dependent on the elastic modulus, E, and the poisson ratio, ν (assumed to be 0.5 for an incompressible medium), of the elastic medium.[124]

$$\mathbf{u}(\mathbf{x}) = (\mathbb{G} * \mathbf{T})(\mathbf{x}) \tag{4.1}$$

$$\mathbb{G}(\mathbf{x}) = \frac{1+\nu}{\pi E}\frac{1}{|\mathbf{x}|^3}\begin{pmatrix} (1-\nu)|\mathbf{x}|^2+\nu x_1^2 & \nu x_1 x_2 \\ \nu x_1 x_2 & (1-\nu)|\mathbf{x}|^2+\nu x_2^2 \end{pmatrix} \text{ where, } |\mathbf{x}| = \sqrt{x_1^2 + x_2^2} \tag{4.2}$$

The convolution in Equation 4.1 is computationally expensive to solve but can be reduced to a simple and much less demanding product by applying a Fourier transform to both the traction field and Green's function (denoted by the hat symbol in Equation 4.3 and 4.4), which now depend on the spatial wave vector, $\mathbf{k}$.[125] Equation 4.1 and 4.3 represent the forward problem; determining the displacement field from the traction field. In the case of TFM, the problem of interest is the inverse, where the traction field must be calculated from the experimentally measured displacement field. Unfortunately, this cannot simply be achieved by inversion of Equation 4.3, as the problem is said to be ill-posed.[126] In this case, an ill-posed problem is defined as one whose solution is sensitive to noise in the initial conditions. This can be understood by considering the forward problem as a smoothing operation; any traction field applied to the elastic medium results in a smooth displacement field. However, the experimentally measured displacement field is likely to contain high frequency noise resulting from errors in recording the bead positions, which in the case of simple inversion (Equation 4.5), will result in a highly divergent traction field. This is a well known property common to inverse problems and can be resolved by introducing a technique known as regularisation.[127–129]

$$\hat{\mathbf{u}}(\mathbf{k}) = \hat{\mathbb{G}}(\mathbf{k})\hat{\mathbf{T}}(\mathbf{k}) \tag{4.3}$$

$$\hat{\mathbb{G}}(\mathbf{k}) = \frac{1+\nu}{\pi E}\frac{1}{|\mathbf{k}|^3}\begin{pmatrix} (1-\nu)|\mathbf{k}|^2+\nu k_2^2 & -\nu k_1 k_2 \\ -\nu k_1 k_2 & (1-\nu)|\mathbf{k}|^2+\nu k_1^2 \end{pmatrix} \text{ where, } |\mathbf{k}| = \sqrt{k_1^2+k_2^2} \tag{4.4}$$

$$\hat{\mathbf{T}}(\mathbf{k}) = \hat{\mathbb{G}}(\mathbf{k})^{-1}\hat{\mathbf{u}}(\mathbf{k}) \tag{4.5}$$

4.2.2 Regularisation

In the case of simple inversion, the inverse problem is solved for $\hat{\mathbf{T}}$ by minimising the residual norm, $\left\|\hat{\mathbb{G}}\hat{\mathbf{T}} - \hat{\mathbf{u}}\right\|^2$. However, as discussed, this will result in an unsatisfactory solution in the presence of experimental noise in the displacement field. Instead, the minimisation condition is modified to include a regularisation term in a technique known as Tikhonov regularisation.[130] The minimisation condition is now modified in such a way that value of the solution norm $\left\|\hat{\mathbf{T}}_\lambda\right\|^2$ is constrained, effectively filtering the high frequency noise and producing a smooth solution (Equation 4.6). The degree of smoothing is determined by the regularisation parameter, λ.

$$min\left\{\left\|\hat{\mathbb{G}}\hat{\mathbf{T}}_\lambda - \hat{\mathbf{u}}\right\|^2 + \lambda^2\left\|\hat{\mathbf{T}}_\lambda\right\|^2\right\} \tag{4.6}$$

The expression to be minimised can be solved for $\hat{\mathbf{T}}_\lambda$ for varying values of λ using the following explicit solution, which is the regularised version of Equation 4.5, in which $\hat{\mathbb{G}}^T$ represents the matrix transpose of $\hat{\mathbb{G}}$ and I is the identity matrix:[122]

$$\hat{\mathbf{T}}_\lambda = (\hat{\mathbb{G}}^T\hat{\mathbb{G}} + \lambda^2 I)^{-1}\hat{\mathbb{G}}^T\hat{\mathbf{u}} \tag{4.7}$$

The above regularisation scheme allows for a suitable solution to be found in the presence of a noise corrupted displacement field. Using this scheme presents the problem of choosing the correct regularisation parameter, λ. If λ is too small, the solution will be dominated by an overestimation of the noise. On the other hand, if λ is too large the solution will be over-smoothed and the traction field will not be representative of the data. In order to balance these two outcomes, a curve is plotted of the residual norm, $\left\|\hat{\mathbb{G}}\hat{\mathbf{T}}_\lambda - \hat{\mathbf{u}}\right\|$, and the solution norm, $\left\|\hat{\mathbf{T}}_\lambda\right\|$, for varying degrees of regularisation (see Figure 4.2b). This curve typically has a characteristic L-shape, and hence this selection method is known as the L-curve criterion.[131] The corner of the curve represents the optimum balance between fitting the data (lowest residual norm), and constraining the solution (lowest solution norm). This process is outlined in Figure 4.2d, where the under, over, and optimum regularisation is shown for the recovery of the circular traction shown in Figure 4.2a. In practice, where the optimal value for λ is not always straight forward to deduce, but is typically achieved by calculating the point on the L-curve having the highest degree of curvature.

4.2.3 Extracting the displacement field

A key determinant in the accuracy of TFM is the ability to resolve the bead displacements at the top surface of the gel. A number of methods have been employed to measure the displacements and they can broadly be separated into two categories: 1) Those that depend on tracking the motion of each individual fluorescent bead, known as Single Particle Tracking (SPT). 2) Those that rely on extracting the average displacement within subregions of the image based on a correlative method to track features within the subregion. Here, I briefly introduce examples of each method and outline their appropriate use.

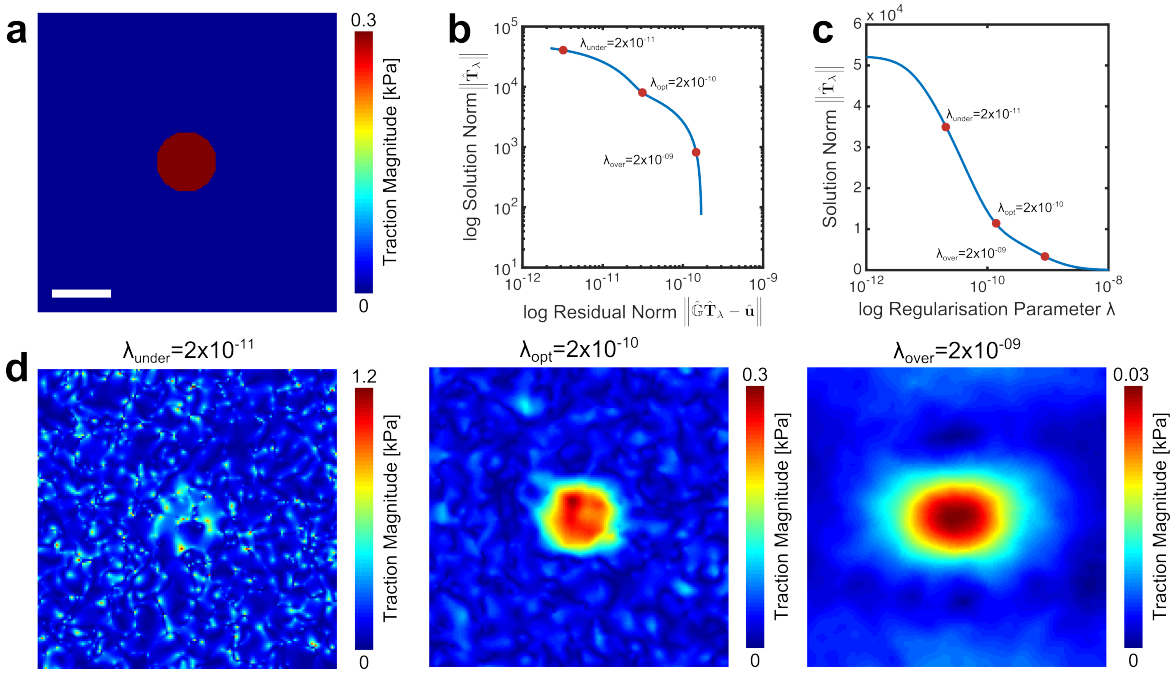


Fig. 4.2 TFM regularisation - **a**) Simulated circular traction field. Red shows regions of high traction and blue shows regions of low tractions. Scale bar is 2 µm. **b**) Residual norm plotted against the solution norm for a range of regularisation parameters, λ, for the recovery of the simulated traction field. The traction recovery for the three degrees of regularisation indicated along the line are shown in **d**). **c**) Solution norm for each value of the regularisation parameters. **d**) Recovery of the traction field for each value of the highlighted regularisation parameter: $\lambda = 2 \times 10^{-11}$ (left) shows under-regularisation, over fitting the noise in the data. $\lambda = 2 \times 10^{-09}$ (right) shows over-regularisation, underestimating the traction magnitude. $\lambda = 2 \times 10^{-10}$ (middle), shows the correct degree of regularisation, showing good agreement between the recovery and simulation.

Single particle tracking

Perhaps the most straight forward technique to extract the gel displacement is to locate and track each individual fluorescent bead, by so called SPT.[132] Typically, this is achieved by first locating each bead within the whole field of view using a feature finding algorithm. In this work, a suite of feature finding routines developed in MATLAB by Kilfoil *et al.* is used.[117] Once the coordinates of each bead have been established, the positions of the bead in the subsequent frames can be extracted. This can be achieved by various methods including nearest neighbour analysis, or correlation based analysis. For this work, a correlation based technique was implemented in MATLAB and is briefly described in the following. The algorithm fits each bead with a 2D Gaussian function, defining a model function for each bead in the field of view (see Figure 4.3a). In each subsequent frame, a spatial correlation is made between the model fit and the subregion surrounding the bead (see Figure 4.3b). The peak in the correlation indicates the position of the bead in the frame and the relative shift in the peak between frames represents the displacement of the bead. This can be done for each frame of the time-lapse, leading to a track of the bead displacement over time. To increase the robustness of this technique, the correlation function at each time point is multiplied by a 2D Gaussian function with a mean centred on the position of the bead in the previous frame, thus biasing the correlation function to bead positions close to the initial position (see Figure 4.3c,d). The width of the 2D Gaussian used to bias the correlation should correspond to the maximum expected displacement of the bead between frames.

SPT is well suited to data containing spatially complex displacements. This includes data in which nearby beads move is opposing directions, or data in which beads move small distances over short periods of time. The tracking of each individual beads ensures no information is lost in either of these cases.

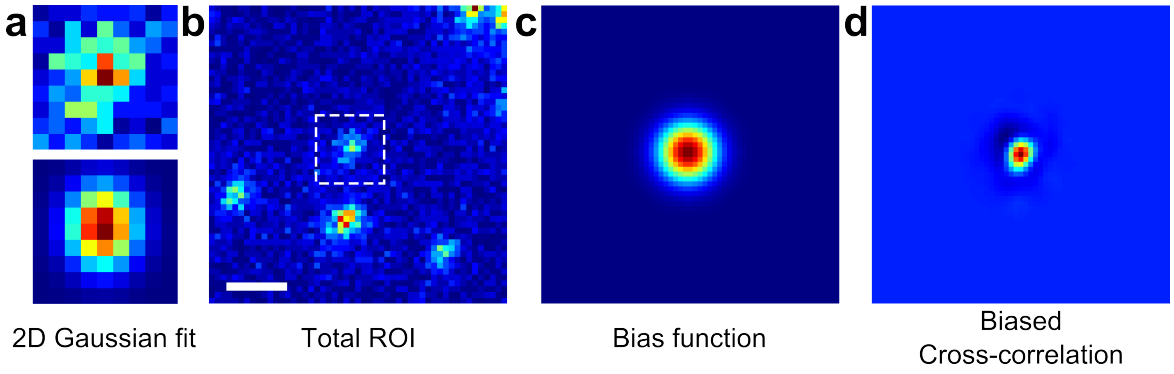


Fig. 4.3 Bead tracking method via SPT - **a**) Zoom in to the image of an individual bead (top) and resulting Gaussian fit to the bead image (bottom). **b**) Larger field-of-view image of the bead shown in **a**) (dotted square), showing the region of interest (ROI) surrounding the bead. Scale bar is 200 nm. **c**) Gaussian bias function, the width of which defines the expected bead displacement. **d**) Cross correlation of the fitted bead image **a**) and the ROI **b**) multiplied by the bias function **c**). This was performed for each frame of the time-lapse and the peak in the biased cross-correlation calculated, indicating the most likely position of the bead in each frame.

Correlation based techniques

The mostly commonly used correlative technique is known as Particle Image Velocimetry (PIV).[133,134] In PIV, the image pairs representing the stressed and unstressed gel are divided into subregions. Each subregion is then correlated with the corresponding subregion at the next time point. The peak in the spatial correlation indicates the most likely position of the second subregion relative to the first.[135] This technique relies on the uniqueness of the fluorescence distribution within the subregion to provide an accurate measure of the displacement. The subregion must also be large enough to contain sufficient spatial fluorescence fluctuations to provide a robust correlation. In practice, this corresponds to the number of resolvable beads within the subregion. Because PIV relies on analysing a subregion and not individual beads, small high frequency displacements may be lost. However, the use of a subregion makes the technique robust against noise within image. Most PIV algorithms work on an iterative scheme, whereby the subregion size is initially large to capture course displacements and is subsequently decreased in size to refine the displacement. At each new iteration, the displacement from the previous is used as an initial guess for the next.[136]

PIV is better suited to data in which many beads move in a coordinated manner and data which is free from complex, high frequency displacements in which the spatial averaging that occurs during PIV will lead to loss of information.

4.2.4 Improving TFM using STED

The accuracy of TFM is limited to two distinct ways. First, by the density of points at which the displacement can be measured within the gel. If the density of points is not sufficient, areas of the gel will be displaced without being reported by any bead movements and information is lost. Therefore, it is crucial that the density at which the displacement field is sampled is sufficiently high to reflect the spatial complexity of the force field generated by the cell. This can be formalised as a Nyquist sampling problem, whereby the spatial sampling frequency of the displacement field must be twice that of any spatial details recoverable from the displacement field (see Figure 4.1b).

Secondly, its accuracy is limited by how well the displacement of each bead can be measured. If the bead movements are too small, then the algorithms discussed previously will struggle to resolve the displacement accurately. Conversely, if the displacements are too large, the finite gel thickness may invalidate the assumption of an elastic half space with the displacements being perturbed due to the attachment of the gel to the solid substrate beneath. Moreover, elastic materials only behave in a linear manner over a finite strain range. If the gel is displaced beyond this linear regime, complex non-linear effects may be observed, contravening our linear assumption and invalidating the models outlined above.

Whilst the second problem can largely be solved by tuning the stiffness of the gel, bringing the bead displacements into a desirable range, the first problem is more fundamental. In classical TFM, this limit is imposed by the density at which fluorescent

beads can be placed within the gel. Due to the finite size PSF representing the position of each fluorescent bead, at high densities, nearby PSF begin to overlap and become difficult to resolve individually. When this occurs, their relative displacements are impossible to extract and information regarding their relative displacement is lost.

This problem was recognised by Sabass *et al.*, who developed a method of doubling the bead density by using marker beads of two different colours, allowing them to be spectrally separated. In doing so, they were able to achieve resolutions of order 1 µm allowing them to resolve the force distributions of single focal adhesions. However, this approach is ultimately limited by the spectral range of the microscope. As mentioned, the ability to simultaneously record fluorescence data from the cell simultaneously to force information is a key advantage of TFM, therefore limiting its spectral range due the bead displacement measurements is undesirable.

Here, an alternative approach is taken to increase the sampling density. Instead of spectrally separating the dense distribution of beads, the beads are spatially separate by taking advantage of the increase in resolution offered by STED microscopy, introducing STFM. By combining the conventional confocal PSF with a second spatially modulated doughnut shaped depletion PSF, STED microscopy can reduce the size of the observed PSF (see Figure 4.1c,d). Following excitation of the fluorescent molecule from the ground state by the excitation laser, the STED laser light, which is of a higher wavelength than the excitation light, stimulates the emission of a photon of the same wavelength as the STED, thus molecules exposed to the STED light do not contribute to the observed fluorescence emission. The doughnut shape of the STED beam results in only those molecules in the zero intensity area defining the centre of the doughnut contributing to the fluorescence signal, thus reducing the apparent size of the observed PSF. Note that due to the requirement to image through the gel and image live cells, other super resolution techniques would not be well suited to TFM,

with the exception of Structured Illumination Microscopy (SIM), which could offer some resolution enhancement of the beads at the top surface of the gel.[115]

4.3 Increased sampling density improves traction recovery

In order to establish the level of improvement gained by using the higher bead densities made possible by STED microscopy, I conducted computational simulations using the theoretical frame work outlined by FTTC. The simulations consisted of first constructing a circular traction field, $\mathbf{T}(\mathbf{x})$, of a defined radius and magnitude (0.3 kPa). The magnitude of the force is kept uniform across the circular traction and only tractions in the x-direction are simulated. This simulation is an approximation to the nature of force generation is focal adhesions, where a defined area of adhesion is made between the cell and the substrate, and forces are typically aligned along one axis. By multiplying the Fourier transform of the traction field with the Fourier space Green function (Equation 4.4) the corresponding displacement field $\mathbf{u}(\mathbf{x})$ was calculated assuming a gel elastic modulus of 3 kPa and a poisson ratio of $\nu = 0.5$.

The simulation exists on a discretised computational space of a certain size, in our case a 1000 x 1000 matrix, with values of T_x, T_y and subsequently u_x, u_y at each matrix element. The pixel space corresponds to real space by defining a pixel size in nanometres. To simulate the finite sampling density that characterises a real TFM experiment, the computational space is randomly sub-sampled at sampling densities that can be achieved using conventional confocal techniques and those that can be achieved using STED microscopy. At the top surface of the gel, a resolution of (80 ± 14) nm and (336 ± 68) nm can be expected for STED and confocal respectively (see Figure 4.4a,b). Simulation were conducted to establish the relationship between

the fraction of overlapping beads and the bead density for both confocal and STED resolutions (see Figure 4.4c,d). Using these simulations, three sampling densities are defined as low - 0.5 beads per µm^2, where very few PSFs overlap in confocal and STED, medium - 3 beads per µm^2, where around 70 % of PSFs overlap in confocal compared to only 10 % in STED, and high - 15 beads per µm^2, where 100 % of PSFs overlap in confocal and only 30 % in STED. Here, beads are defined as overlapping if their proximity is less than or equal to the resolution.

Sub-sampling the dense computational space leads to a sparse matrix of displacement values in the x and y directions. To recover the traction field, the use of Fourier transform necessitates the interpolation onto a regular grid of a defined mesh size. This mesh size is chosen based on the average distance between the sub-sampled points such that each grid element contains on average one displacement vector. The sub-sampled displacement field is then transformed into a traction field via Equation 4.7 where the regularisation parameter λ is chosen via the L-curve criterion outline previously. To assess the quality of the reconstruction and judge the level of information loss during the sub-sampling procedure a metric known as the Deviation of Traction Magnitude (DTM) is introduced (see Equation 4.8). A DTM of 0 represents a perfect recovery of the traction. Conversely, a DTM of -1 represents a complete underestimation of the traction.

$$DTM = \frac{\|T_{recovered}\| - \|T_{simulated}\|}{\|T_{recovered}\| + \|T_{simulated}\|} \tag{4.8}$$

For each of the sampling density, a range of tractions with increasing diameter are simulated (see Figure 4.5a). Their corresponding displacement field is then calculated and sub-sampled followed by traction recovery. The DTM for each recovery is then calculated, the results of which are shown in Figure 4.5b. It is evident that for a given sampling density there is a point at which the traction diameter becomes too small to

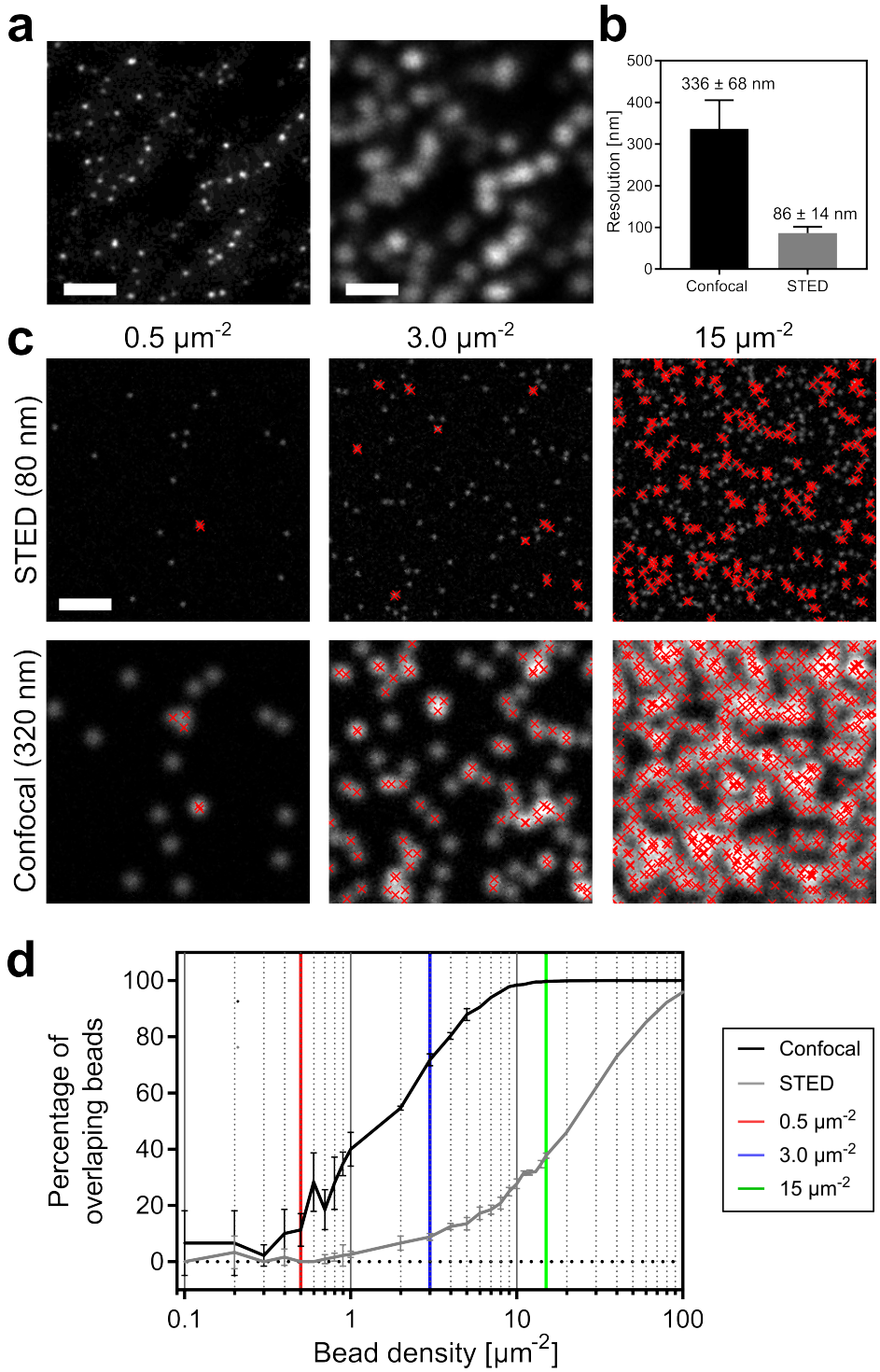


Fig. 4.4 STED and confocal bead density - **a**) Representative STED (left) and confocal (right) images of 40 nm red fluorescent beads at the top surface of a PAA gel at a depth of 30 µm imaged using a water immersion objective. Scale bar is 1 µm. **a**) Quantification of the Full Width at Half Maximum (FWHM) of a Gaussian fit applied to each bead within the image with the mean and standard deviation for each condition. **c**) Simulated bead images at differing bead densities at confocal and STED resolutions. Red crosses indicate pairs of beads that are overlapping i.e. whose proximity is less than the resolution. Scale bar is 1 µm. **d**) Quantification of the percentage of overlapping beads at a range of bead densities in confocal and STED. Highlighted in red, blue and green and the bead densities 0.5, 3.0 and 15 beads µm^2 respectively.

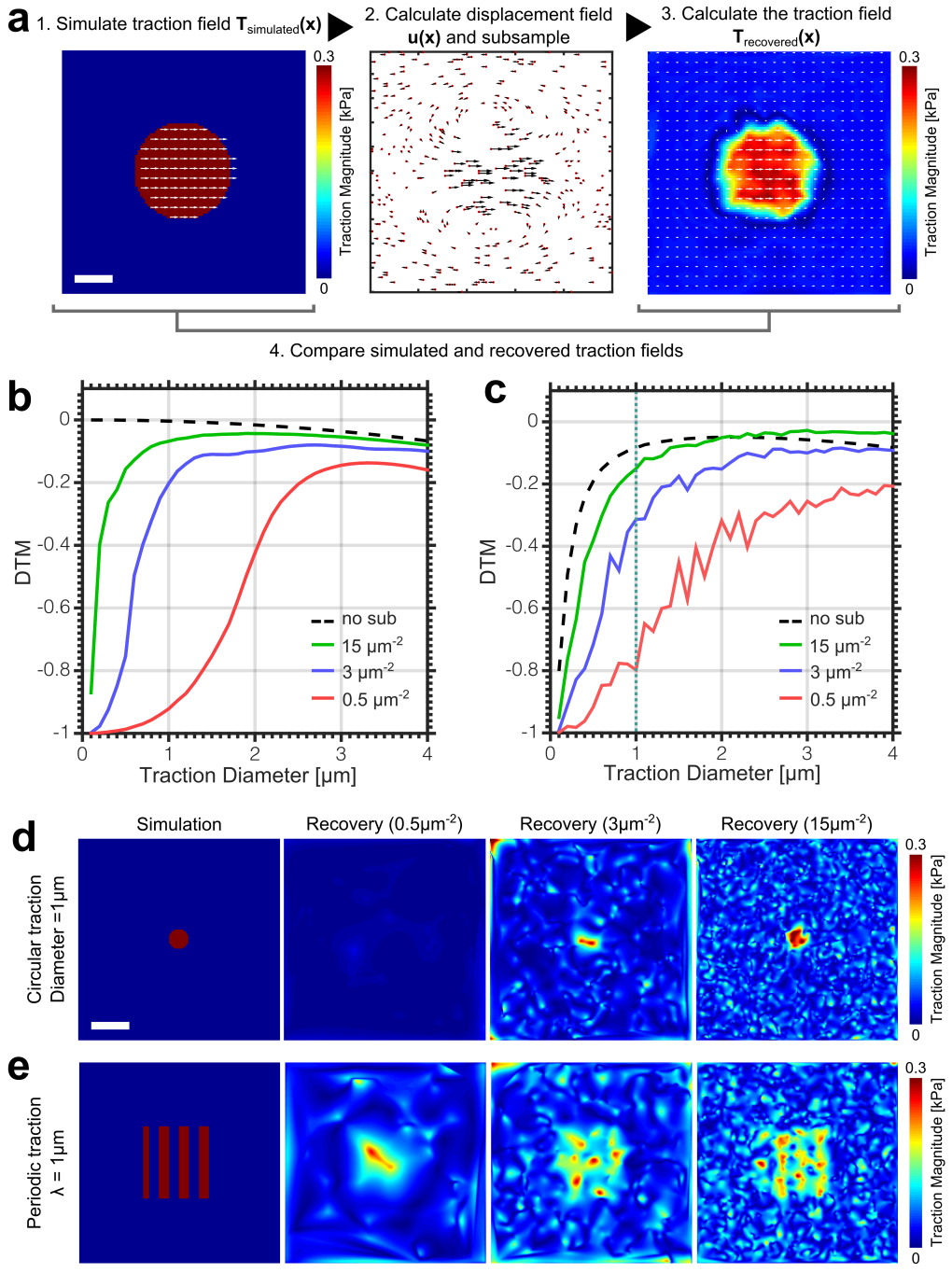


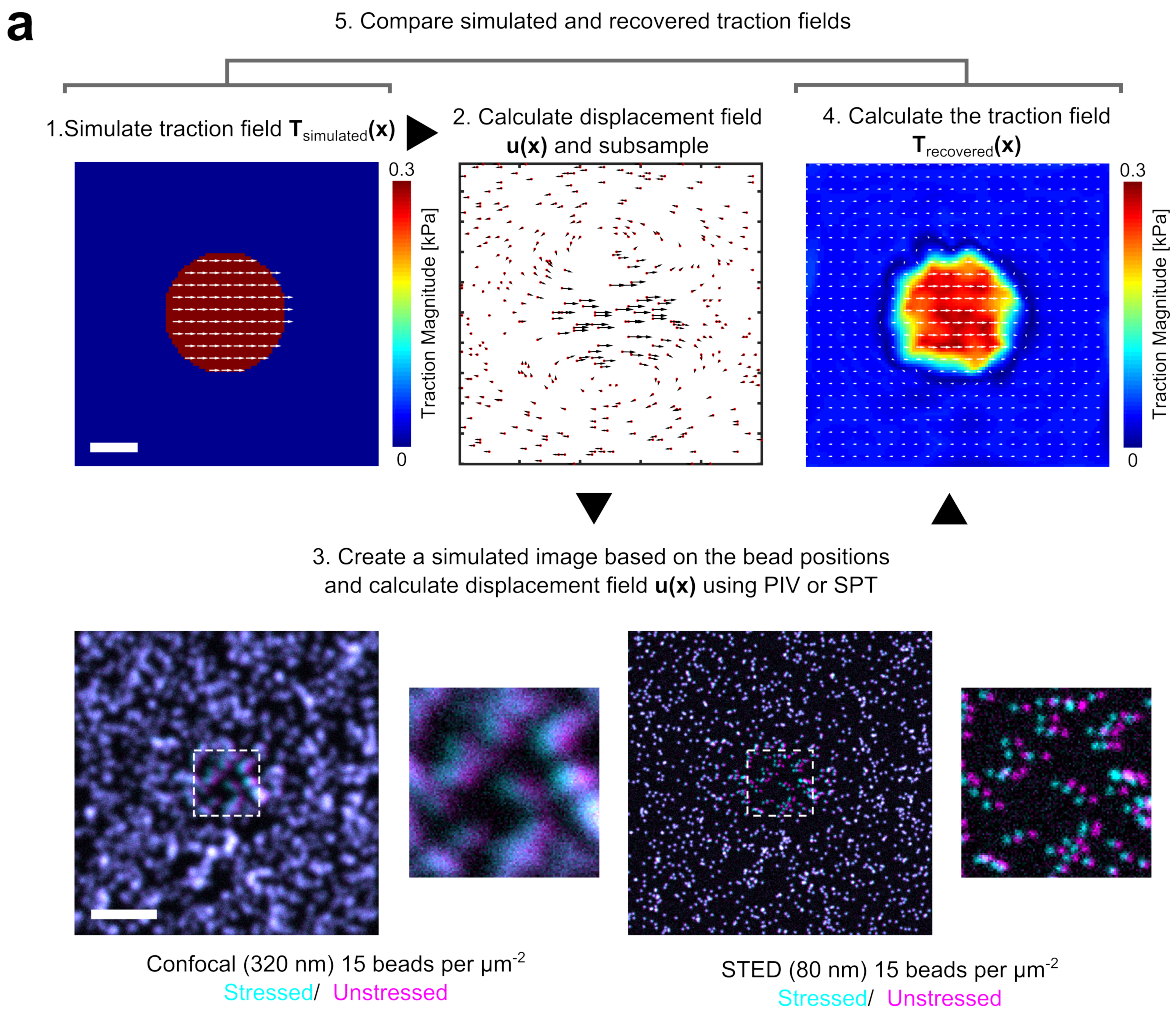
Fig. 4.5 STFM simulations - **a**) A uniform circular traction field $T_{simulated}(x)$ is simulated and the corresponding displacement field u(x) calculated (heat map; high traction magnitude warm colours, low traction magnitudes cold colours, white arrows: traction direction). The displacement field is then subsampled at a confocal and STED density (red dots: bead positions, black arrows: bead displacements), the traction field recovered $T_{recovered}(x)$ and the simulation and recovery compared by the deviation of traction magnitude (DTM). Scale bar is 1 µm. **b**) DTM for varying traction diameters at three sampling densities, confocal (red), medium STED (blue), and maximum STED (green). A DTM of 0 represents a perfect traction recovery, whereas a DTM of -1 represents a complete underestimation. Dotted line: DTM for no subsampling. Line deviates from zero at large tractions due to artefacts introduced by the finite size of the simulated gel area. **c**) Same as b with the addition of artificial noise and using the regularised solution, showing very similar dependency as **b**) except for the no subsampling case (dotted line), where regularisation masks the recovered tractions at length scales matching that of the artificial noise. **d**) Simulation and traction recovery for a 1 µm diameter circular traction zone (0.3 kPa). Scale bar 2 µm. **e**) Simulation and traction recovery for a 1 µm wavelength periodic traction pattern. Scale bar 2 µm.

be successfully recovered. Crucially, the size of traction at which this happens becomes smaller with increasing sampling density. The results shown here are in agreement with what would be expected from the Nyquist theorem for sampling and illustrates that a sampling density of 15 beads per μm^2 would allow the recovery of tractions 400 nm in diameter (see Figure 4.1b).

The same simulation is performed in Figure 4.5c, but now with the addition of Gaussian distributed noise with a width equal to the 10 % of the maximum displacement. Because the displacement field has been corrupted with noise the regularisation scheme described above must be used, with the regularisation parameter chosen by the L-curve criterion. Despite the addition of noise, the conclusions drawn from Figure 4.5b are unchanged. To further illustrate the effect of sampling density on traction recovery two traction patterns are presented, one circular, and one a periodic series of parallel tractions (see Figure 4.5d,e). In each case, it is evident that increasing the sampling density improves the traction recovery, giving a better agreement with the simulation.

Next, to establish the effect of the displacement algorithm on traction recovery, both SPT and PIV are tested using the simulation procedure outlined above. The displacement field is calculated and sub-sampled as before, but now the sparse displacement vectors are replaced by a PSF representing the initial and final displaced positions (see Figure 4.6). The bead images are simulated at both STED and confocal resolutions and at a bead density of 15 beads per μm^2, producing two image pairs simulating a reference and displaced gel for two different resolutions of beads, 320 nm and 80 nm.

By first applying SPT to track the bead displacements, it is evident from the confocal image that there is a high level of overlapping PSF as outlined previously, making it challenging to identify the position of each individual bead (see Figure 4.6a). In the STED case, the majority of beads can be individually resolved, giving a good



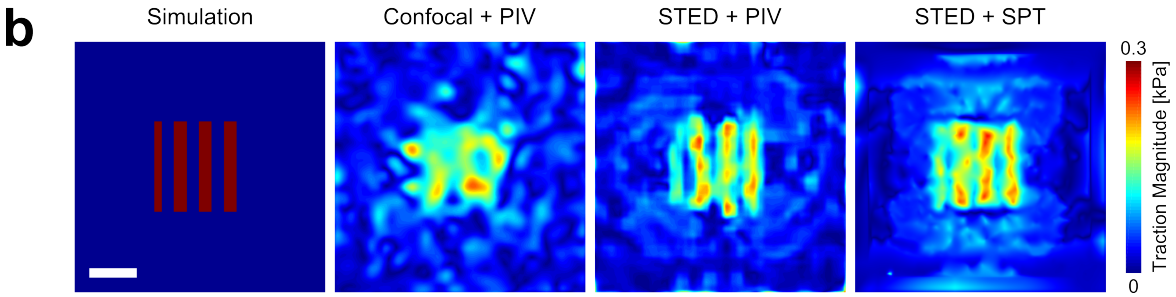


Fig. 4.6 Comparing traction recovery using PIV and SPT - **a**) A traction field $T_{simulated}(x)$ is simulated and the corresponding displacement field u(x) calculated (heat map; high traction magnitude warm colours, low traction magnitudes cold colours, white arrows: traction direction). The displacement field is then sub-sampled at 15 beads per µm^2 (red dots: bead positions, black arrows: bead displacements). A pair of fluorescent bead images (stressed-cyan and unstressed-magenta) are simulated using the random bead positions and displacements. Bead positions are replaced with PSFs at resolutions corresponding to confocal (320 nm) and STED (80 nm) (inset: zoom in of boxed region). PIV and SPT are used to extract the bead displacements which are then transformed into the recovered traction field $T_{recovered}(x)$ and the simulation and recovery are compared by the Deviation of Traction Magnitude (DTM) and the Normalised Least Square Error (NLS). Scale bar is 2 µm. **b**) Simulation and traction recovery for a 1 µm wavelength periodic traction pattern (0 - 0.3 kPa) using PIV (confocal and STED) and SPT (STED only). Scale bar is 2 µm.

Table 4.1 Comparing traction recovery using PIV and SPT - Quantification of the difference in traction recovery using PIV and SPT in combination with confocal and STED imaging. Traction recovery is compared using the Deviation of Traction Magnitude (DTM) and the Normalised Least Square Error (NLS).

	PIV		SPT	
	Confocal	STED	Confocal	STED
DTM	-0.22 ± 0.02	-0.23 ± 0.01	n/a	-0.18 ± 0.05
NLS	0.48 ± 0.08	0.25 ± 0.01	n/a	0.27 ± 0.04

representation of the displacement field. By extracting the displacement field, the corresponding traction field can be calculated and compared with the simulation, as was done previously (see Figure 4.6b). At this density it is clear that STED offers an advantage as the confocal images prohibits any accurate tracking of displacement and hence no traction field can be recovered.

Next, a PIV algorithm is used to recover the displacements from the simulated images. In this case, there is no requirement to resolve the beads individually, therefore it is possible to extract a displacement field and hence a traction field, for both the confocal and STED image pairs. On visual inspection of the recovered traction fields, it is clear that PIV in combination with STED shows a better agreement with the simulation compared to confocal. Note, that in both cases, the interrogation window size used for the PIV algorithm was the same (20 pixel). To quantify this improvement the DTM and normalised least square error (NLS) is shown in Table 4.1 for both resolutions and algorithms. Note that for PIV, the DTM cannot detect the spatially more accurate force field in the case of STED compared to confocal, and therefore the method of the NLS is employed to compare the results upon SPT and PIV reconstruction.

4.4 STFM experimental optimisation

Before applying STFM to a biological system, it was necessary to optimise a number of experimental conditions, including the distribution of fluorescent beads within the gel, as well as the STED imaging conditions.

The fluorescent beads required to track the displacement of the gel are typically added to the un-polymerised acrylamide/bis-acrylamide mixture at a given ratio. As the gel polymerises the beads are immobilised within the gel matrix and remain in place. Whilst this is an effective methods of adding beads to the gel, it results in a distribution of beads throughout the thickness of the gel. This is undesirable as only beads at the top surface are useful for measuring forces. In addition, out of focus light from beads that are not at the top surface contribute to a high level of signal background, making high contrast imaging of the beads at the top surface challenging. This becomes especially problematic when high bead densities are used, as is required for STFM. To alleviate this, this typical strategy is modified to ensure beads are only present at the top surface of the gel.[137] To achieve this, the cover-slip used to form the top of the gel sandwich is first functionalised with poly-L-lysine followed by a coating of fluorescent beads, creating a dense and uniform layer of beads on the cover-slip. When the sandwich is formed, the beads are captured within the gel solution as it polymerises, resulting in a dense layer of beads that is restricted to the top layer of the PAA gel.

Because STED microscopy is here used as a confocal-based technique, it can be performed at any focal plane within the sample. This is a key requirement for TFM, where imaging is performed at a focal plane at the top surface of the PAA gel and away from the cover-slip. Because the PAA gel has a refractive index that differs significantly from glass (around n=1.33), using an oil objective optimised for glass will lead to

optical aberrations and result in reduced signal and STED resolution when imaging at top of the gel (Figure 4.7a,b,c,d). It is therefore desirable to minimise these aberrations by limiting the thickness of the gel to around 30 µm to reduce scattering losses while maintaining sufficient thickness to avoid problems with the assumption of gel linear elasticity and effects of the glass surface. In addition to this, an objective immersion medium should be used which is well matched to the refractive index of the gel. Using a water immersion objective is found to work well in this case, exhibiting minimal spherical aberrations and allowing a 4-fold resolution enhancement using STED at a depth of 30 µm (see Figure 4.4a).

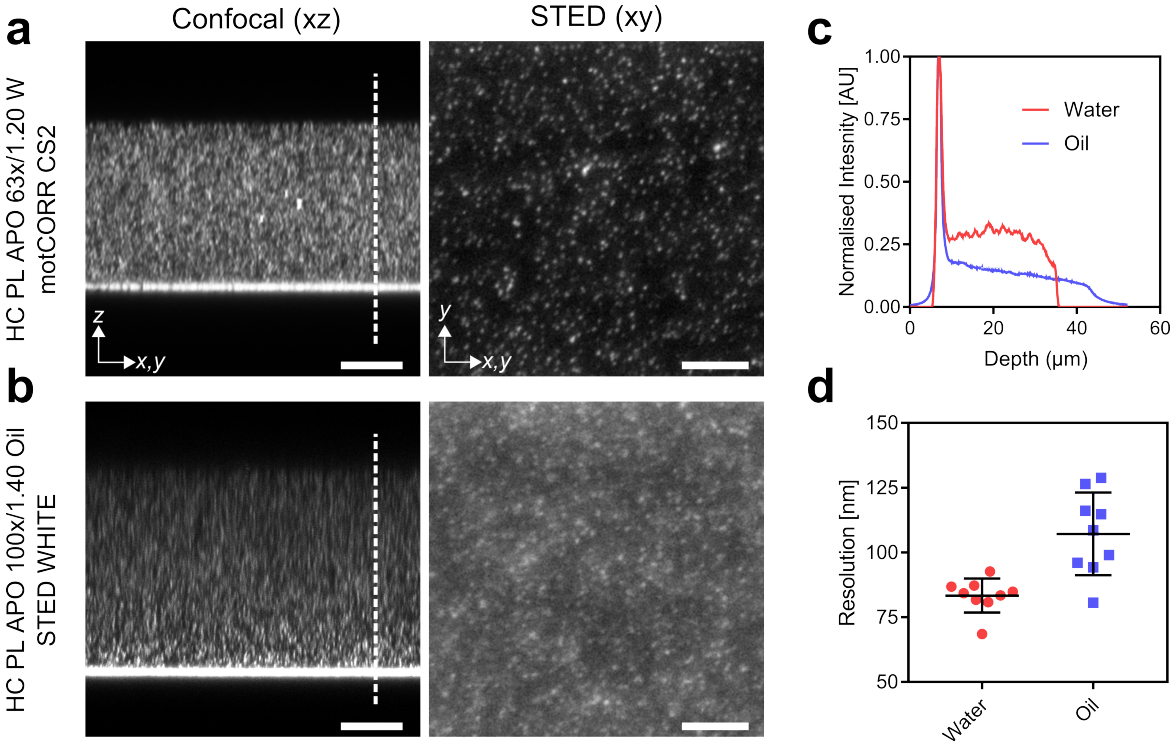


Fig. 4.7 Microscope objective characterisation - **a,b**) PAA gel cross-section (left) showing the distribution of the fluorescent marker beads acquired using the **a**) Leica HC PL APO 63x/1.2 Water motCORR CS2 and **b**) the Leica HC PL APO 100x/1.4 Oil STED WHITE Objective. Scale bar is 10 µm . The corresponding STED image (right) taken at a depth of 30 µm within the gel. Scale bar is 2 µm. (c) Normalised intensity of the fluorescent signal as a function of depth within the gel. Signal decays linearly with depth using the oil objective, whereas the signal is maintained even to a depth of 30 µm using the water objective. (d) Comparison of the obtained STED resolution at a depth of 20 µm using both the oil and water objectives. STED resolution is improved by using the water objective, presumably because of the reduced spherical aberrations which better maintain the intensity distribution of the STED depletion doughnut. Error bars are standard deviations from the mean.

4.5 STFM of HeLa cell focal adhesion

Simulations demonstrate that STED can improve the accuracy of TFM. However, this result is only of interest if the increased accuracy can be observed in a practical biological experiment. HeLa cell focal adhesions are chosen as an initial proof of principle as they have been previously well characterised using TFM.[121,127,138] Focal adhesions form when certain cells come into contact with a solid substrate, serving as anchoring points for the cell, mediating transmission of mechanical force generated by the cell cytoskeleton tangential to the substrate. Focal adhesions have a well defined molecular architecture, and thus they can be readily visualised at the interface between an adherent cell and the substrate. Of interest here is that focal adhesions form force generating structures that can be validated by the presence of a fluorescent signal. Without such a molecular marker of force, it would be difficult to ascertain where forces would be expected at the cell interface. In addition to this, focal adhesions range from a few microns to hundreds of nanometre, thus mimicking the previously presented simulation conditions, where the traction diameter was varied and the success of traction recovery quantified.

To quantify the force transmitted by each focal adhesion, the gel is imaged under tension when the cell is attached to the gel substrate and secondly when the cell has detached and the gel has returned to a relaxed equilibrium state. The displacements of the gel during the relaxation will report on how much force was being applied by the cell to the gel. To allow the cell to attach, the gel is first functionalised with fibronectin. This protein, found in the Extra Cellular Matrix (ECM), facilitates the adherence of the HeLa cell to the PAA gel via the interactions of integrins on the cell surface. Detachment of the cell from the gel is carried out by the addition of the protease, trypsin.

To assess whether a more accurate traction map can be ascertained using STFM, bead images are recorded in STED and confocal before an after cell detachment, as well as the positions of the adhesions via fluorescently tagged paxillin-EGFP, a protein which localises to the adhesion. Here, because the same area of the cell is imaged in both STED and confocal, it necessitates that only one bead density can be used. Thus, the ability of STED to resolve more detail in the traction field over confocal at a single high bead density is being tested. The experiment is analogous to the simulations presented in Figure 4.6, where STED combined with PIV outperformed confocal and PIV.

Figure 4.8 shows the results of this process. A cell adhering to a 40 kPa PAA gel formed focal adhesions at the periphery of the contact area. It is evident that at a bead density of 5 beads per μm^2 there are a considerable number of overlapping beads in the confocal images, nevertheless, the movement of the gel after trypsinising the cell is evident (see Figure 4.8c). In contrast, STED imaging of the same region of the gel leads to far fewer overlapping beads and hence the displacement is more apparent, particularly in areas where small displacements of the gel combine with high bead densities (see Figure 4.8d). Using PIV, in analogy to the simulations, the traction field can be recovered for each pair of stressed and unstressed images in both STED and confocal (see Figure 4.8e,f). On visual inspection, it is apparent that the STED tractions are in better agreement with the fluorescent distribution of focal adhesions. This is confirmed by taking line profiles of selected areas within the traction field (see Figure 4.8g).

4.6 STFM of RBL cell activation

The persistent motivation in developing STFM is to apply these techniques to measure forces in immune cells, specifically T cells. As discussed for the specific case of T cells,

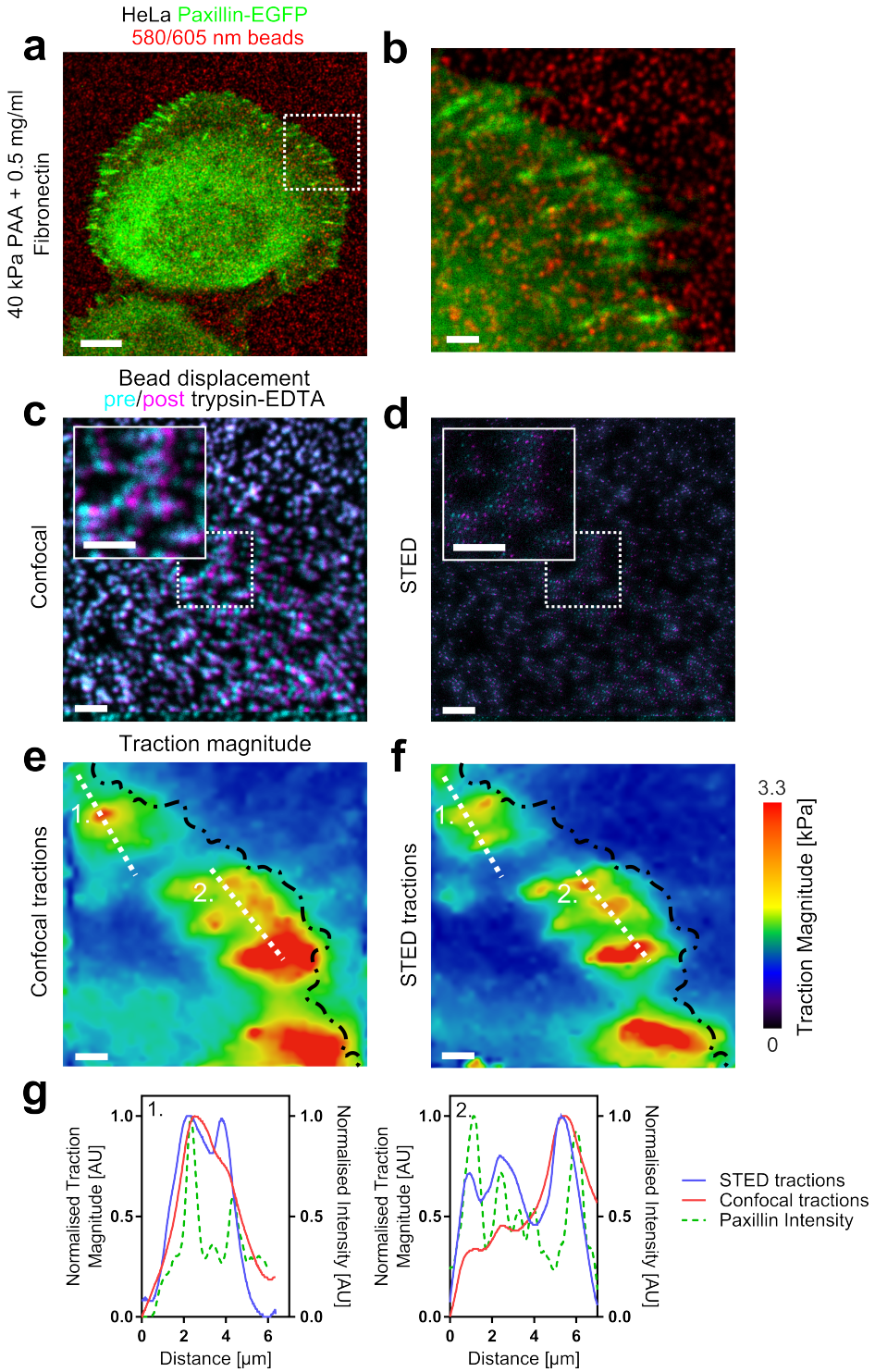


Fig. 4.8 STFM applied to HeLa cell focal adhesions. **a**) Representative fluorescent image of HeLa cell expressing paxillin-EGFP (green) adhering to a 40 kPa PAA gel coated with fibronectin and loaded with 40 nm red-fluorescent beads (red). Scale bar is 10 µm. **b**) Zoom in of inset marked in **a**). Scale bar is 2 µm. **c,d**) Confocal **c**) and **d**) STED fluorescent bead image of gel area under the cell, before (cyan) and after (magenta) trypsin-EDTA treatment. Scale bar is 2 µm. Inset – Zoom in of dotted square region. Scale bar is 2 µm. **e,f** Traction magnitude calculated from the measured confocal **e**) and STED **f**) recordings of the bead displacements. Scale bar is 2 µm. Black dotted line represents cell boundary. **g**) Line profiles showing the traction magnitude and the corresponding fluorescent intensities across the focal adhesions for STED (blue) and confocal (red) imaging. The dashed green line represents the fluorescence intensity distribution of paxillin.

receptor-ligand interactions at the plasma membrane during cell-cell contacts occur on the precise level of single proteins. In contrast, focal adhesion are highly order structures consisting of hundreds of proteins which collectively transmit mechanical force to the substrate. Because of the qualitative different in the nature of force generation between these two cells types it is necessary to examine if STFM can enhance force measurements in immune cells.

To this end, a well studied receptor-ligand interaction of the innate immune system is chosen as a further proof of concept. RBL cells express high levels of the Fcϵ receptor-1 (FcϵR1) on their plasma membrane. FcϵR1 binds IgE with high affinity (equilibrium constant $K_a = 10^{10}$ M^{-1}, off-rate $k_{off} = 10^{-5}$ s^{-1}), and the interaction results in activation of the RBL cell.[99,139] The interaction of RBL cells and a glass cover-slip coated in immobilised IgE results in rapid spreading and adherence to the surface. To measure the forces mediated via the IgE-FcϵR1 interaction during cell spreading,RBL cells are allowed to interact with a 3 kPa gel loaded with 40 nm red-fluorescent beads and coated with the antibody, IgE (see Figure 4.9a).

To visualise the dynamic spreading of the RBL cell contact with the IgE coated gel, actin filaments were labelled with Lifeact-citrine (see Figure 4.9b). On inspection, the beads beneath the cell were seen to move elastically in a directed manner, indicating forces being applied by the cell to the compliant gel beneath via the FcϵR1-IgE interaction. To once again examine the increase in accuracy made possible by STFM, bead displacements during RBL cell activation were recorded at two different densities (low - 0.4 beads per µm^2 and high - 2.2 beads per µm^2), with each density recorded in both STED and confocal (see Figure 4.9c). Note, low density is defined as the maximum trackable bead density by confocal, and high density as the maximum trackable density of our current STED experiments. Bead sampling values in the scenario of high density STED were a moderate and robust choice considering the

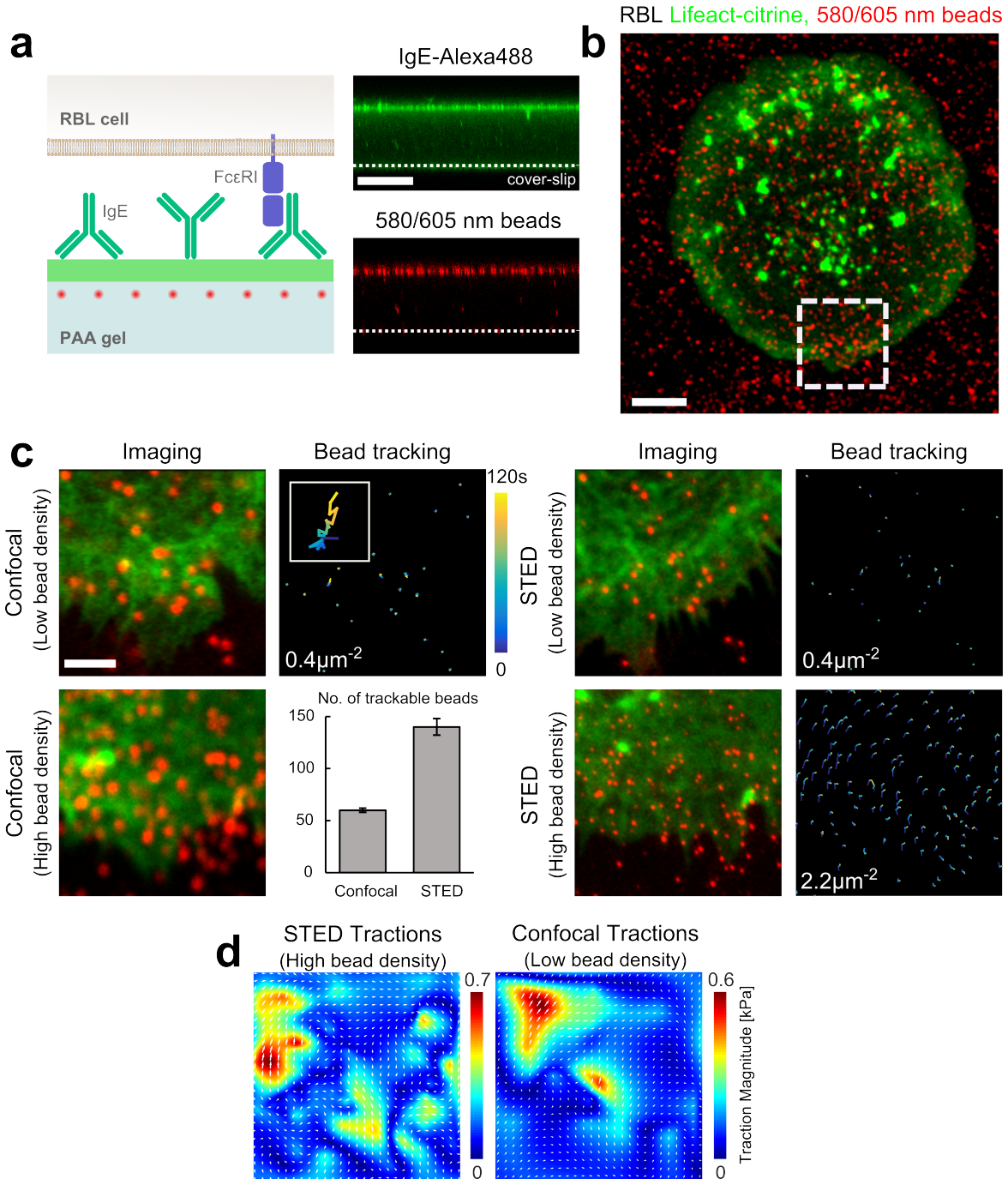


Fig. 4.9 STFM applied to RBL cell activation **a**) Gel functionalisation. (Left) Scheme: The roughly 30 µm thick PAA gel layer (light blue) was loaded with 40 nm nm-large red fluorescent beads (red dots) and surface-coated with poly-L-lysine (light green) followed by attachment of IgE (green). (Middle, right) Confocal z-x profile images of the gel cross-section showing concentration of Alexa488 labelled IgE (green, middle) and red fluorescent beads (red, right) at the top surface of the gel. Scale bar 30 µm. **b**) Representative confocal image of fluorescent F-actin (Lifeact-citrine) expressing RBL cell (green) interacting with IgE coated 3 kPa PAA gel loaded with the red fluorescent beads (red). Scale bar 10 µm. **c**) Time-lapse imaging of the spreading cell edge results in the displacement of the beads within the gel, monitored for different conditions as labelled. (Left panels) Confocal images of fluorescent F actin (green) and confocal or STED images of red fluorescent beads (red) at a certain time point together with the temporal displacement tracks of the beads (time colour-coded as labelled), for low ($0.4\,\mu m^{-2}$) and high ($2.2\,\mu m^{-2}$) bead density. Scale bar 2 µm. For confocal at high bead density (lower left) no bead tracks could be resolved; instead a bar chart is shown, quantifying the ability to successfully locate and track beads in the high density confocal case compared to the high density STED case (total number of beads: 140 STED, 60 confocal). **d**) Recovered traction field for the high density STED tracking of **c**) (left) and extrapolated low density effective confocal tracking (right) with force colour-coded in kPa.

experimental optical conditions and needs of the biological specimen. However, they were below the computationally predicted possible advances of STFM.

In each case, bead displacements were quantified using SPT. SPT was favoured over PIV in this scenario as the motion of the beads was spatially complex, unlike those resulting from focal adhesions, where many beads move in a spatially coherent manner. In the low density case, applying the SPT algorithm described in section 4.2.3 allowed the displacements of all beads within the field of view to be measured in both the confocal and STED image sequences. In the high density case, confocal imaging resulted in a significant number of overlapping PSFs, preventing reliable bead tracking. However, on applying the STED beam, beads were resolved individually and the tracking was successful. In all cases, bead tracks were interpolated onto a regular mesh and the corresponding traction field calculated using the appropriate degree of regularisation as chosen again by the L-curve criterion. In the high density case, only the STED imaging yielded a traction field. To directly compare the effect of sampling density on the ability to accurately recover the traction field of the same cell, beads in the high density STED case were randomly deleted until the bead density was equal to that attainable by confocal tracking (see Figure 4.9d). From this, it is clear that this reduces the information content present in the displacement field, and hence reduces the fine detail in the traction field.

4.7 Summary

In this chapter, I have described how TFM can be improved by combining with the fluorescence optical super-resolution technique, STED. This has been shown via simulations and in two biological system: focal adhesions and an activating RBL cell. The development of STFM represents an important improvement of a well used technique. However, the experimental validation of STFM failed to reach the

improvements predicted by simulations (see Figure 4.5). This was primarily due to the limited spatial resolution of STED at the top surface of the gel, which made imaging at the higher bead densities of $15\,\mu m^{-2}$ challenging. Spherical aberrations induced by the difference in refractive index of the gel and the glass resulted in degradation of the STED depletion beam, limiting the resolution enhancement. This should be addressed in future work with the addition of adaptive optics to correct detrimental aberrations to the STED beam and improve resolution at the top surface of the gel, allowing experiments to approach the resolution enhancements outlined by simulations.[140,141]

Whilst STFM can improve the overall spatial accuracy of force recovery, it does this at the expense of photo-stability and temporal resolution. Because of the higher laser powers required for STED, the level of photo-bleaching observed is higher compared to confocal, suggesting STFM is not well suited to measuring force generation over long periods of time, unless low frame rates are used. In addition to this, the increase in resolution of STED requires scanning at smaller pixel sizes and longer dwell times, resulting in a reduced frame rate compared to confocal. Again, this indicates that STFM is better suited to systems in which force generation occurs on the time scale of minutes.

Chapter 5

T-cell force generation

In this chapter, I apply the tools and techniques acquired in chapter 4 to measure the mechanical force generated during T-cell activation, specifically those forces present during the formation and maintenance of the IS. During IS formation, the T cell is known to form a symmetric actin lamellipodial structure that is believed to be responsible for force generation.[4] Here, using the 1G4-TCR Jurkat T-cell system, the kinetics of the interaction between the TCR and the pMHC can be modulated, allowing the relationship between force generation, the dynamics of the actin cytoskeleton and the kinetics of the antigen during activation to be investigated.

First, to validate that the engineered 1G4-TCR Jurkat T-cell system was able to be stimulated by the desired range of antigens, the activation response to the kinetically different anti-CD3 antibodies, OKT3 and UCHT1, and the pMHCs, HLA-9V and HLA-4D, was systematically assessed using a calcium release assay (see Figure 5.1). Next, the calcium release assay was combined with a quantification of the response of the actin cytoskeleton to the range of antigens, highlighting the importance of actin polymerisation and cell spreading as a marker for activation. Because force generation at the IS is likely to be actin dependent, our investigations of the actin cytoskeleton

were extended, employing LLSM to demonstrate the global rearrangements of actin that characterise IS formation and maturation, followed by the use of confocal microscopy and TIRF-SIM to quantify the antigen dependence of actin retrograde flow and the distribution of actin velocity at the IS. Finally, TFM was applied to measure the antigen dependence of mechanical forces generation at the IS, over both short and long time-scales. Lastly, specific pharmacological agents were used to highlight the cytoskeletal processes responsible for the measured forces.

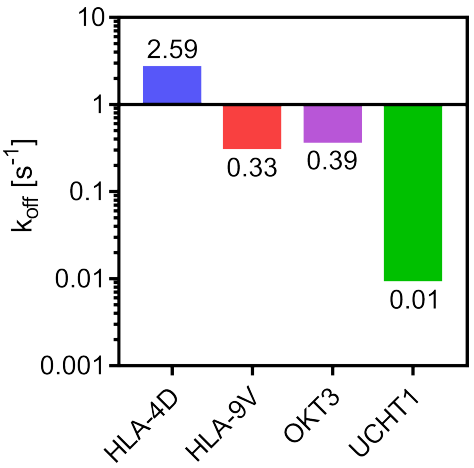


Fig. 5.1 1G4-TCR kinetics - Graph showing the k_{off} rates of the 1G4-TCR specific pMHC, HLA-9V and HLA-9V, as well as the anti-CD3 antibodies, OKT3 and UCHT1. Data reproduced from.[101,142]

5.1 1G4-TCR Jurkat T-cell calcium response is antigen dependent

A key marker for TCR triggering is the release of Ca^{2+} from the ER. To assess the activation response of the engineered 1G4-TCR Jurkat T-cells, a calcium response assay was developed that allows the recording of simultaneous calcium response curves for hundreds of cells at a time at single cell resolution and high frame rates (Figure 5.2a,b). The cells were exposed to four different surfaces, coated with the anti-CD3 antibodies UCHT1 and OKT3, and the pMHCs, HLA-9V and HLA-4D, as well as a negative

control which was not coated with any antigen. Using the calcium sensitive dye, Fluo-4 AM, the intracellular levels of calcium could be monitored over time. Following acquisition of 1000 frames, at a frame rate of $1.3\,s^{-1}$, images were analysed via the custom-written MATLAB software package, CalQuo.[116] The software located the positions of each cell and extracted the fluorescence intensity in each frame, producing an intensity response curve for each cell, allowing filtering of the data based on the nature of the response curve.

5.1.1 1G4-TCR Jurkat T-cell triggering is antigen dependent

For all cover-slip conditions, the calcium response of the cells fell into three distinct categories. Cells showed either a single peaked response, an oscillatory response characterised by multiple peaks separated in time, or no peaks at all. In the following I refer to these responses as: single, oscillating and non-triggering, respectively. In addition to this, cells that show either a single or oscillating response are referred to collectively as triggered. Figure 5.2c displays representative intensity curves for each calcium response. Note, the elevated levels of calcium observed at the end of the recording are due to the addition of ionomysin, which stimulates the release of calcium.[143] This was used as a control to assess the calcium fluxing ability of each cell.

Firstly, it was evident that all surfaces induced a large fraction, around 80 %, of the cells to display some form of calcium response, with very few showing no elevated levels of calcium on coming into contact with the glass surface. Surprisingly, this was also true for the negative control, which despite having no specific interaction with the TCR was able to induce a calcium flux, suggesting that TCR triggering is able to occur in a ligand independent manner in this system.

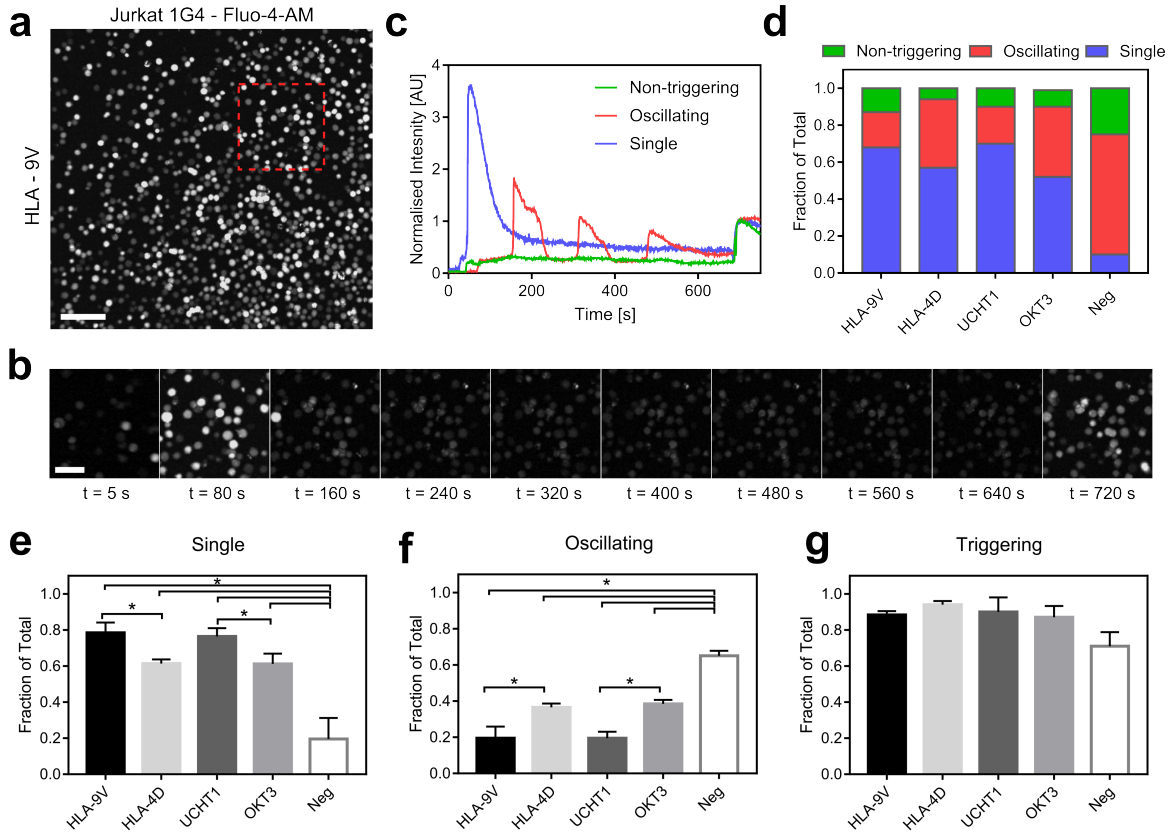


Fig. 5.2 1G4-TCR Jurkat T-cell calcium release - **a**) Representative image of 1G4-TCR Jurkat T-cell calcium response on contacting an antigen coated glass cover-slip, visualised by the calcium sensitive dye Fluo-4 AM. Scale bar is 100 µm. **b**) Montage showing the Fluo-4AM intensity variation over time of 1G4-TCR Jurkat T-cell on contacting an antigen coated glass cover-slip. Scale bar is 50 µm. **c**) Representative calcium response curves for the three categories of response, non-triggering (green), oscillating (red) and single (blue). **d**) Summary of the fractions of each calcium response for each antigen. **e,f,g**) Individual plots forming **d**) showing the fraction of single peaked, oscillating, and triggering (single and oscillating) cells for each antigen. $*$ denotes a p-value of <0.05, N = 200 cells for each antigen condition. Error bars represent the standard deviation on the mean of two repeats.

Whilst no significant difference was observed in the number of triggering cells across all surfaces, the nature of calcium response was antigen dependent (see Figure 5.2d). Comparing the two pMHC coated surfaces, the number of single peaked responses was significantly higher for the higher affinity HLA-9V ($k_{off} = 0.33\,s^{-1}$) peptide compared to HLA-4D ($k_{off} = 2.59\,s^{-1}$)[101] (p-value < 0.05, see Figure 5.2e). Further to this, there was a corresponding decrease in the fraction of oscillatory responses for HLA-9V compared to HLA-4D (p-value < 0.05, see Figure 5.2f). The anti-CD3 coated surfaces displayed a similar pattern, with the higher affinity UCHT1 ($k_{off} = 0.01\,s^{-1}$) giving an increased fraction of single peaks compared to OKT3 ($k_{off} = 0.39\,s^{-1}$) and a corresponding decrease in the number of oscillating cells (p-value < 0.05 in both cases).[142] The negative control surfaces showed significantly higher numbers of oscillating cells than any of the antigen coated surfaces (p-value < 0.05).

In general, these results indicate that the 1G4-TCR Jurkat T-cells are able to be stimulated by the specific pMHCs. The results suggest that higher affinity antigens lead to more single peaked responses which agrees well with previous observations.[102]

5.1.2 Actin spreading follows single calcium peak

T-cell activation is also characterised by rapid polymerisation of actin, which increases the contact area between the cell and the activating surface. To investigate the role of the calcium response, specifically the difference between the oscillating and single peaked response, on the actin cytoskeleton, the calcium assay is extended to include time-lapse imaging of actin simultaneously to calcium. To explore whether the actin cytoskeleton of oscillating and single peaked cells induces spreading, the experiments were performed with the extremes of the previous measurement. The HLA-9V coating showed the greatest fraction of single peaked responses, whilst the cover-slip with no antigen showed the greatest portion of oscillating responses.

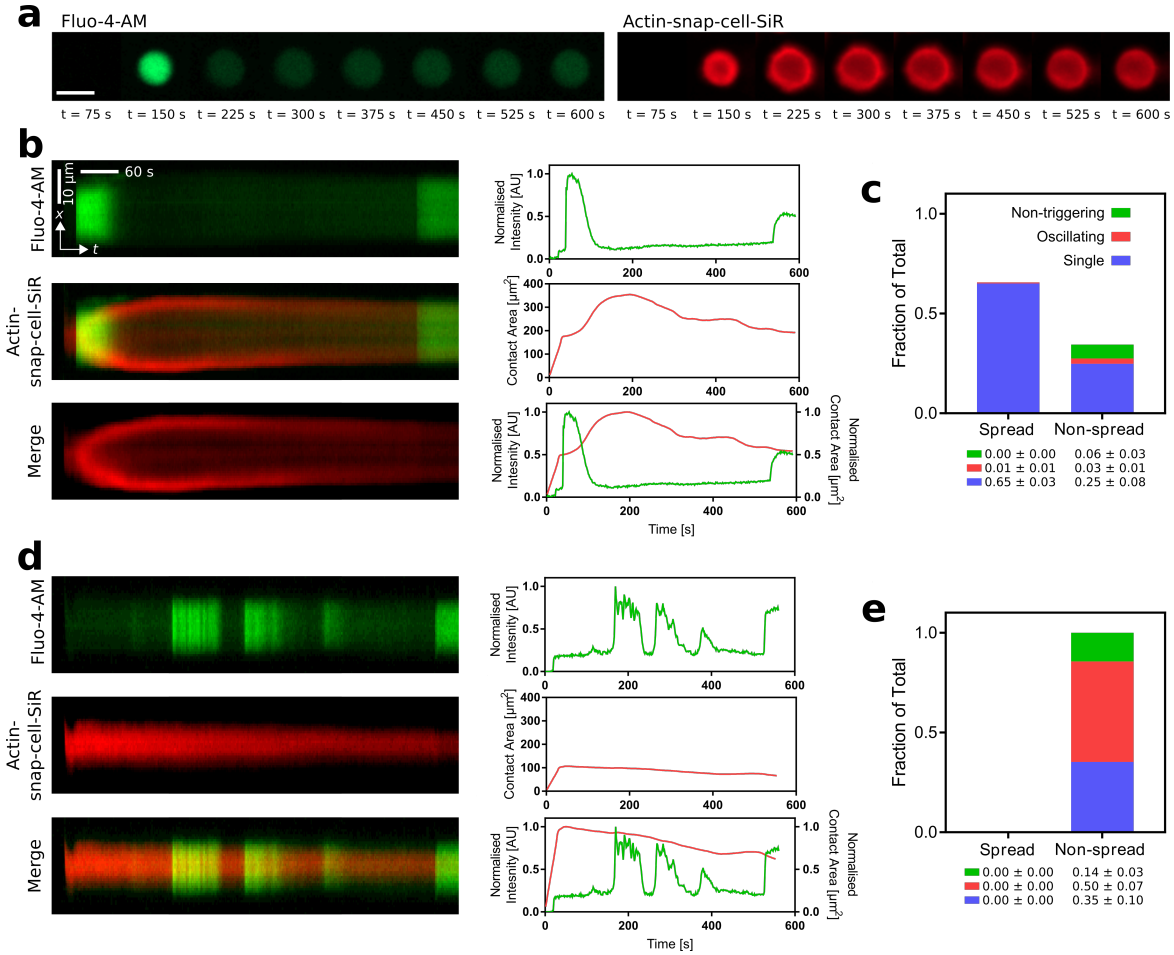


Fig. 5.3 Simultaneous actin and calcium response - **a**) 1G4-TCR Jurkat T-cells interacting over time with a glass surface coated with HLA-9V, labelled with Fluo-4 AM (left) and actin-snap-cell-SiR. Scale bar is 20 µm. **b**) Left - Kymograph showing Fluo-4 AM intensity (upper) and actin distribution (middle) over time during the interaction of a 1G4-TCR Jurkat T-cell with a surface coated with HLA-9V. The lower image shows a merge of the two. Right - Quantification of the Fluo-4 AM intensity (upper) and quantification of the cell contact area over time. The lower plot shows a merge of the two. **b**) Systematic quantification of the fraction of spreading and non-spreading cells as measured by actin distribution on contact with a HLA-9V coated surface, with the fraction of single, oscillating and non-triggering cells denoted in each case, as measured by calcium response. N = 100 cells. Errors are the standard deviation of the mean of two repeats. **d**) Left - Kymograph showing Fluo-4 AM intensity (upper) and actin distribution (middle) over time during the interaction of a 1G4-TCR Jurkat T-cell with an uncoated surface. The lower image shows a merge of the two. Right - Quantification of the Fluo-4 AM intensity (upper) and quantification of the cell contact area over time. The lower plot shows a merge of the two. **e**) Systematic quantification of the fraction of spreading and non-spreading cells as measured by actin distribution on contact with an uncoated surface, with the fraction of single, oscillating and non-triggering cells denoted in each case, as measured by calcium response. N = 100 cells. Errors are the standard deviation of the mean of two repeats.

Figure 5.3b shows a kymograph of a representative cell interacting with a surface coated with HLA-9V. The kymograph is formed of a line profile taken through the centre of the cell contact area. The calcium response (shown in green), can be seen to increase rapidly soon after contact is made with the surface. As expected, the actin signal (shown in red) begins to spread, as shown here by a broadening of the kymograph signal. Also visible in the actin channel is the high intensity actin signal at the periphery of the contact combined with a region of low intensity at the centre. The high intensity region represents the spreading lamellipodium, thus combined with the calcium response, this provides good evidence that there is a strong activation response from the cell. This can also be seen by quantifying the size of the cell contact area which is seen to increase rapidly after the initial contact (see Figure 5.3b). Following a period of stability, the contact area decreases. Interestingly, by combining the calcium response and contact area quantification, it is possible to see that the increase in intracellular calcium occurs prior to the increase in contact area, suggesting that the rapid polymerisation responsible for the increased contact area is not required to induce the initial increase in calcium. This supports the concept that initial triggering of the TCR occurs independently of rearrangements of the actin cytoskeleton. To quantify the fraction of spreading and non-spreading cells, the whole population (N = 100 cells) was systematically analysed, correlating the calcium response with the actin behaviour. Figure 5.3c shows the results of this quantification for HLA-9V, indicating that the majority of spreading cells show a single peaks of calcium.

Figure 5.3d shows the response of a representative cell on the negative control surface. In contrast to the cell interacting with surface bound HLA-9V, the calcium response is seen to oscillate and no actin spreading is observed. This is confirmed by quantifying the contact area, which remains constant throughout the calcium oscillations. Figure 5.3e shows the results of quantifying the fraction of spreading and

non-spreading cells across the whole population on the uncoated surface, revealing that the majority of cells show an oscillating response and no cells spread on the surface.

This is an intriguing result, as elevated calcium levels are good evidence that the TCR is being triggered. However, it suggests that in the case of oscillations, signalling downstream of the TCR is curtailed such that no actin spreading is observed. Since actin polymerisation is not induced in cells with calcium oscillations, it may be the case that actin polymerisation is necessary to stabilise the TCR-pMHC interaction, allowing signalling to continue. Note that in this assay, no calcium is present in the cell medium suggesting the observed calcium flux is derived from the ER.

5.2 Global actin reorganisation during T-cell activation

Next, the novel microscopy technique known as LLSM was used to further characterise the sequence of events that follows initial contact of the T cell with the activating surface.[113] By illuminating with a thin sheet of light, as opposed to the point illumination used for confocal microscopy, LLSM can rapidly scan through the sample, allowing 3D imaging at unprecedented temporal resolution, allowing the whole 3D volume of the cell to be recorded in a few seconds (see Figure 5.4a). The high acquisition speeds possible using LLSM were desirable since the calcium assay indicates that the initial triggering event and actin polymerisation occur within a few seconds of contact with the surface.

Figure 5.4b shows a Jurkat T cell with fluorescently labelled actin interacting with a surface coated with OKT3. The 3D imaging allows the cell to be visualised from any orientation at all time points. Here, we see the cell from an oblique angle and simultaneously from below at the basal plane. From the sequence of images it

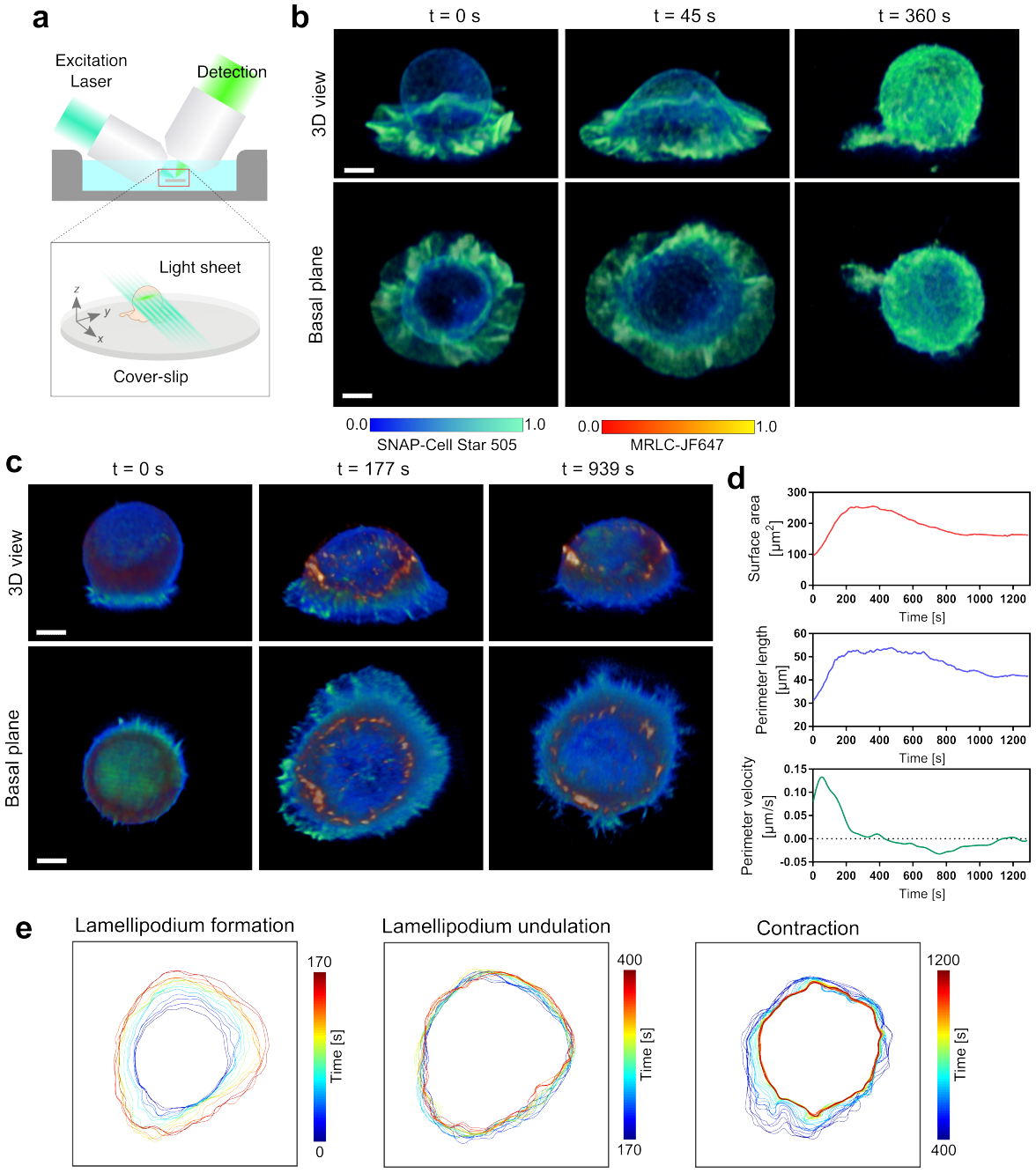


Fig. 5.4 Global actin reorganisation measured by LLSM - **a**) Schematic illustrating the LLSM setup. The first objective creates a Bessel beam scanned in the y-direction creating a sheet of light, while a second objective perpendicular to the first collects the fluorescence emission while the sample is scanned in the x-direction by a piezo stage. **b**) Actin labelled activating T-cell as imaged by LLSM shown in a 3D view (upper) and at the basal plane (lower). Scale bar is 2 µm. **c**) Actin and myosin labelled activating T-cell as imaged by LLSM shown in a 3D view (upper) and at the basal plane (lower). Scale bar is 2 µm. **d**) Quantification of the contact surface area (upper), perimeter length (middle) and perimeter velocity (lower) over time. **e**) Cell perimeter plotted over time during lamellipodium formation (left), lamellipodium undulation (middle) and contraction (right).

is apparent that during the initial contact with the surface the cell is spherical in shape but within a few seconds forms the actin rich lamellipodium. As the contact area increases, the cell shape changes, becoming less spherical and more flat. After a period of undulation of a few minutes, the cell is seen to round up and the contact area between cell and surface decreases. Therefore, as was observed in the calcium experiments, the T-cell cytoskeleton exhibits three distinct phases during activation (see Figure 5.4d,e). The first is characterised by a spherical cell undergoing rapid spreading of actin. This is followed by a stabilisation of the contact area, a reduction in cell height and undulation of the lamellipodial structure. Lastly, the contact area contracts and the cell body returns to a spherical shape.

By visualising myosin IIA in addition to actin, we are better able understand the orchestrated events of the cytoskeleton during activation (see Figure 5.4c). The image sequence again shows an initially spherical T cell which rapidly spreads forming the lamellipodium. As the contact between cell and substrate matures, myosin IIA appears to cluster, forming a ring above the point of contact. The ring like structure of myosin IIA, which is found not at the basal plane but at a height of 2 µm to 5 µm, persists throughout the undulation phase and continues throughout contraction.

Taken together, the LLSM imaging shows the extremely dynamic nature of the T cell during activation, suggesting that actin and myosin work together to orchestrate the reorganisation of the cell.

5.3 Actin retrograde flow velocity is antigen dependent

The preceding experiments demonstrate how the T-cell calcium response is antigen dependent, and that actin spreading follows a single peak of calcium. Given this

modified actin behaviour on negative and activating surfaces, it is unclear whether the dynamics of actin itself is dependent on the antigen presented. This is an important consideration, as previous studies have shown that the dynamics of the TCR at the IS is highly dependent on the actin cytoskeleton, specifically at the periphery of the IS where new TCRs come into contact with pMHCs at the surface. It is interesting to speculate whether actin can adjust its dynamics depending on the kinetics of the TCR interaction, that in turn modulates T-cell signalling. Modulating actin dynamics is also likely to influence the forces generated at the IS. Thus, it is crucial to understand whether any feedback exists between the antigen presented to the cell and the dynamics of the actin cytoskeleton. To investigate this, the actin flow velocity in the lamellipodium of 1G4 Jurkat T-cells was systematically quantified on different surfaces coated with one of the same four antigens as previously used for the calcium assay, namely, the anti-CD3 antibodies OKT3 and UCHT1 and the pMHCs, HLA-9V and HLA-4D.

Velocity quantification was achieved using two methods. First, by extracting kymographs using line sections drawn across the cell contact, velocity can be calculated by a linear fit to the intensity distribution at the edge of the cell in the kymograph (see Figure 5.5e). The linear fit represents tracking a feature as it moves through the lamillipodium, and the gradient of the fit yields the velocity of the feature. Secondly, an optical flow algorithm was applied to validate the kymograph analysis.[136] Optical flow is a commonly used technique in computer vision for analysing the movement between frames of a video sequence (see section 3.17.1). By assuming a constant pixel intensity between frames, optical flow attempts to find the flow, or shift, of each pixel that best maintains the condition of constant brightness. This results in a pixel by pixel velocity map between each frame of the time-lapse (see Figure5.5b,c). By plotting the distribution of velocities at the periphery of the cell, the mean velocity for each cell was quantified (see Figure 5.5d).

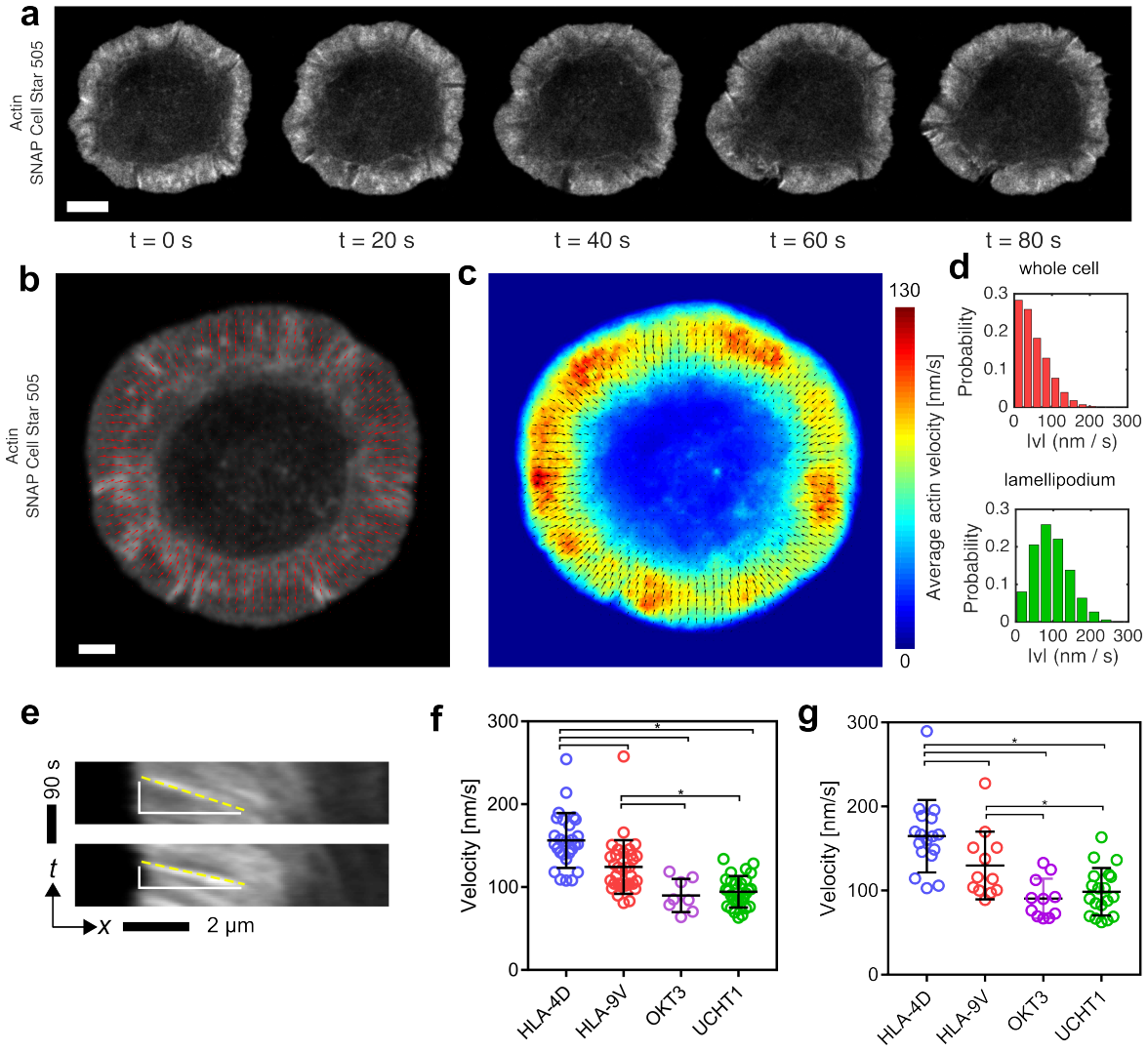


Fig. 5.5 Actin retrograde flow velocity - **a**) Montage showing Actin labelled 1G4-TCR Jurkat T-cell interacting with a surface coated in HLA-9V over time. Scale bar is 5 µm. **b**) Vector map (red arrows) showing actin velocity distribution across the cell contact overlaid with fluorescent image of actin as quantified by optical flow. Scale bar is 2 µm **c**) Vector map (black arrows) showing actin velocity distribution across the cell contact overlaid with corresponding velocity magnitude with high velocity in red and low velocity in blue. **d**) Histogram showing the distribution of magnitude of velocity for the whole cell contact area (upper) and the lamellipodium (lower). **d**) Kymograph analysis of actin retrograde flow in the T cell lamellipodium. Slope of the dashed yellow line represents the velocity of the actin flow. **f**) Quantification of actin flow using kymograph analysis for HLA-4D, HLA-9V, OKT3 and UCHT1. **g**) Quantification of actin flow using optical flow analysis for HLA-4D, HLA-9V, OKT3 and UCHT1. $*$ indicates a p-value of < 0.05. N $\sim$ 10 cells per condition.

Figure 5.5f,g shows the results of the quantification for both the kymograph and optical flow analysis. Strikingly, the velocity quantification reveals a dependence on the presented antigen. The pMHC HLA-4D shows the highest flow velocity, followed by HLA-9V. UCHT1 and OKT3 show the slowest actin velocity. This result suggests that the kinetics of the antigen-TCR interaction can indeed modulate the turnover dynamics of the actin cytoskeleton, providing evidence of feedback between the two systems. However, at this stage the nature of coupling is unclear. The antigens presented to the cell are immobilised on the glass cover-slip. Therefore, on binding to the TCR, the antigen will provide an opposing force to any forces generated by the cytoskeleton. The opposing force will only be present for the time that TCR-antigen interaction remains in place. Given this consideration, it is possible to interpret the results of the flow speed analysis. Antigens such as HLA-4D, having a high k_{off} will be applying a force via the TCR for a shorter time than HLA-9V. This results in a lower opposing force in the case of HLA-4D compared to HLA-9V. The lowering of opposing forces leads to an increased flow speed within the cytoskeleton. However, this interpretation does not extend to the anti-CD3 antibodies, where despite having a significantly different k_{off}, UCHT1 and OKT3 have very similar flow velocities.

5.4 Actin velocity distribution at the IS

Confocal microscopy is a diffraction limited technique, hence the maximum resolvable details are around 250 nm in size. Electron microscopy has repeatedly demonstrated that structures that form the ultra-structural organisation of the actin cytoskeleton are significantly smaller than this, thus to fully understand the complex distribution of actin during activation it was necessary to employ super resolution optical imaging techniques. To capture the dynamics of actin at sufficient temporal and spatial resolution we utilised TIRF-SIM.[114] This technique combines the super resolution technique SIM, with TIRF

illumination, to achieve high resolution (80 nm) in a narrow imaging volume close to the cover-slip to a depth of 150 nm. Because TIRF-SIM is a wide-field technique, acquisition speeds can be far higher than that of a conventional laser-scanning confocal technique, making it extremely well suited to study the dynamics of actin in the close contact formed at the IS. To further increase our ability to resolve the complex structure of actin, cells were labelled using Lifeact-citrine, specifically tagging F-actin, avoiding the background associated with free actin monomers that can mask details within the F-actin structure.

Figure 5.6a shows a representative cell labelled with Lifeact-citrine spreading on a surface coated with the pMHC, HLA-9V. The fine structure within the cytoskeleton at the interface is now much more apparent as compared with confocal images of the equivalent process (see Figure 5.5a). The structure can be divided into three zones. At the periphery, the actin forms a dense mesh-work representing a lamellipodial structure. Close to the centre of the contact, the network becomes less dense and individual bundles of filaments are distinguishable. At the centre of the contact, only a very sparse actin network exists.

Now, applying optical flow to the time-lapse imaging the velocity distribution can be extracted across the cell contact, as was done previously for the confocal imaging (see Figure 5.6b,c,d). By analysing the magnitude of the velocity in each of the three zones of actin, it is clear that not only are the zones structurally different but also have differing actin flow speeds (see Figure 5.6e). As expected, the dense lamellipodial network at the periphery contains the most dynamic actin, while the inner lamella network moves more slowly. The actin at the centre of the contact is largely static. Thus, the variation of actin velocity as a function of the distance from the centre of the cell contact can be plotted (see Figure 5.6f). This can be further illustrated by plotting a kymograph of a radial line from the centre of the cell (see Figure 5.6f). The

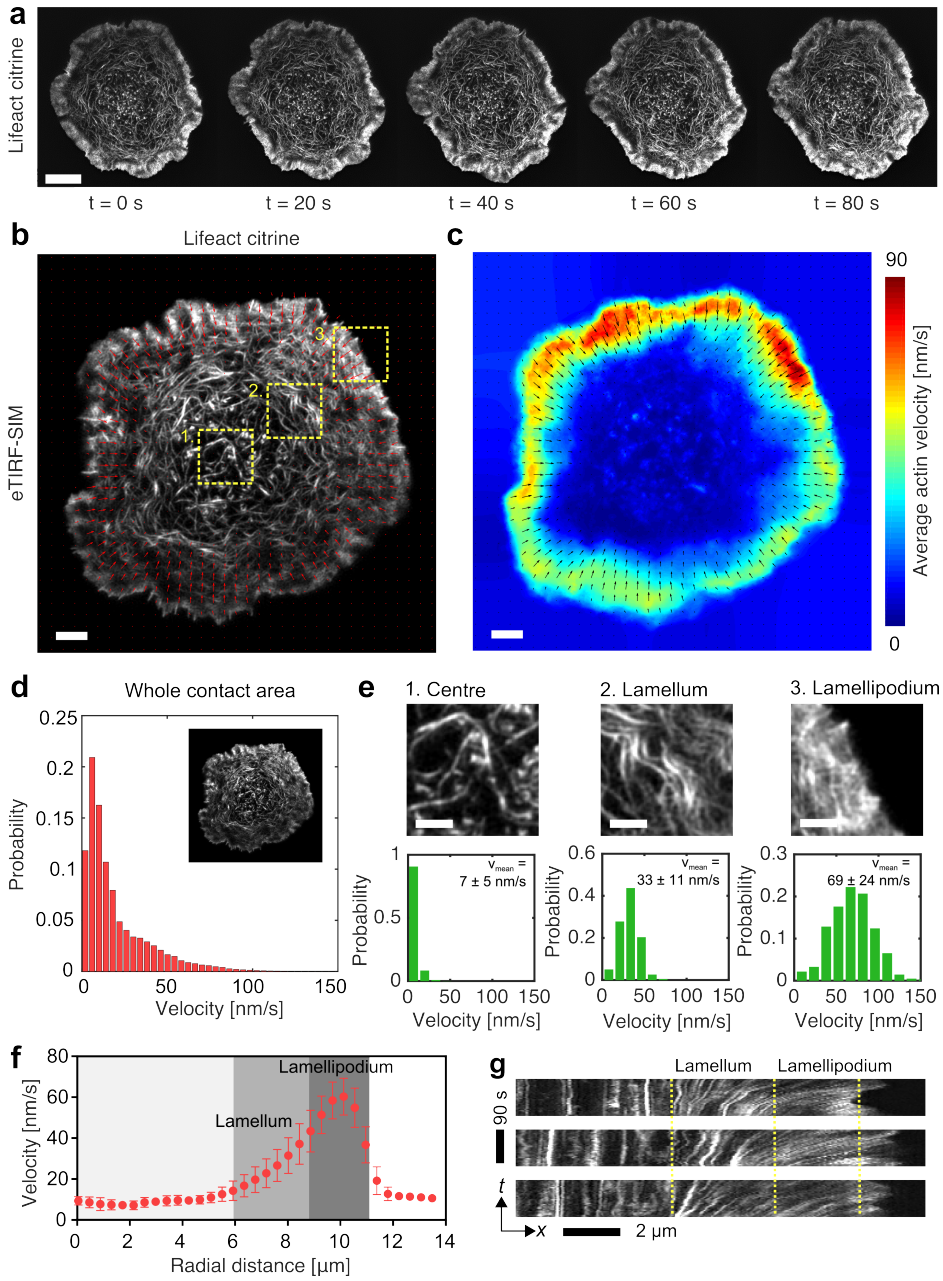


Fig. 5.6 Actin distribution and velocity measured by TIRF-SIM - **a**) Montage showing F-actin labelled 1G4-TCR Jurkat T-cell imaged by TIRF-SIM interacting with a surface coated in HLA-9V over time. Scale bar is 5 µm. **b**) Vector map (red arrows) showing actin velocity distribution across the cell contact overlaid with fluorescent image of actin as quantified by optical flow. Scale bar is 2 µm **c**) Vector map (black arrows) showing actin velocity distribution across the cell contact overlaid with corresponding velocity magnitude with high velocity in red and low velocity in blue. **d**) Histogram showing the distribution of magnitude of velocity for the whole cell contact area. **e**) Image and histogram showing the distribution of magnitude of velocity for the 1. the centre of the contact area, 2. the lamellum and 3. the lamellipodium. Scale bar is 1 µm. **f**) Actin velocity distribution across the contact area as quantified by optical flow, showing the highest velocity at the periphery, coinciding with the lamellipodium. Error bars represent the standard deviation of the mean velocity distribution in 5 cells.**d**) Kymographs showing the variation of actin flow across the contact area in the lamellum and lamellipodium. Steeper features represent lower velocity.

differing flow velocity measured here agrees well with previous measurements of actin flow at the IS.[40] In addition to this, the identification of three distinct zones of actin is supported by measurements of the motion of micro-clusters at the IS.[43] This suggests that force generation is not uniform across the IS, indicating instead that the periphery of the cell is a region of high force and that the actin-poor central region is low in force generation.

5.5 Force generation at the IS

The data presented up to now characterises in detail the nature of the actin cytoskeleton during the activation of T cells. I have shown that the flow speed of actin within the lamellipodium is dependent on the the antigen presented to the cell, suggesting there is feedback between the TCR present on the membrane of the cell and the actin cytoskeleton which flows beneath the membrane. The exact mechanism of feedback is unclear and indeed what links the TCR to the actin cytoskeleton also remains unclear in this study as well as in the literature as a whole. Measuring the velocity of actin is an indirect measure of force generation. Thus to access the forces that signalling molecules, specifically the TCR, are exposed to as a result of the actin flow, we must employ TFM.

5.5.1 Polyacrylamide gel functionalisation

Before being able to measure the forces generated at the IS it was necessary to optimise the interactions of T cells with the PAA surface required for TFM.

Firstly, the gel was functionalised via methods similar to those used to functionalise the glass cover-slips required for the velocity quantification (Figure 5.7a). Using a gel solution containing streptavidin-acrylamide resulted in a final PAA gel having

free streptavidin binding sites for biotin at the upper surface. This allowed the same previously biotinylated antigens to be used to functionalise the top surface of the gel. The binding of the antigen was validated by coating the gel with streptavidin-488, which binds to free biotins on the antigen, thus allowing their distribution to be visualised (see Figure 5.7b). For comparison of antigen coverage, an image showing the distribution of antigen on a glass cover-slip is presented in Figure 5.7c.

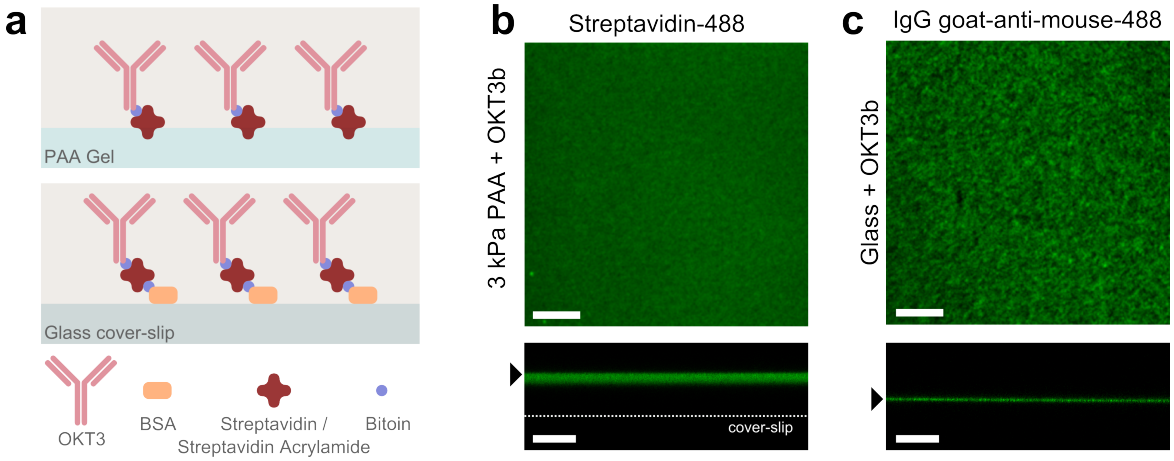


Fig. 5.7 Distribution of antigen on glass and PAA gel - **a**) Schematic summarising the functionalisation scheme of the gel and cover-slip. Streptavidin-acrylamide within the PAA gel allows the binding of biotinylated antigen to the top surface of the gel. The glass cover-slip is first coated with biotinylated BSA, allowing the binding of streptavidin and subsequent binding of biotinylated antigen. **b**) Distribution of biotinylated OKT3 (OKT3b) on a 3 kPa gel, as measured by the distribution of Streptavidin-Alexa488. Upper image shows xy-image and lower shows a xz cross-section. Black arrow indicates focal plane of upper image, scale bars are 5 µm and 20 µm respectively. **c**) Distribution of biotinylated OKT3 (OKT3b) on a glass cover-slip, as measured by the distribution of IgG-goat-anti-mouse-Alexa488. Upper image shows xy-image and lower shows a xz cross-section. Black arrow indicates focal plane of upper image, scale bars are 5 µm and 20 µm respectively.

To examine whether the functionalised gel would induce activation in 1G4 Jurkat T cells, the surface of the gel was functionalised as described and cells labelled with actin-SNAP Cell 505 allowed to interact with the gel. As a measure of activation, the contact area of the cell and the gel surface was quantified. As has been demonstrated previously (using the calcium assay and subsequent actin quantification), the increase in cell contact area is a reliable read out of successful initiation of activation.

The quantification of spreading was carried out for four surfaces. Firstly, 3 kPa PAA gels coated with OKT3b, and for comparison, uncoated gels. Secondly, uncoated cover-slips and those coated with OKT3 to serve as negative and positive controls.

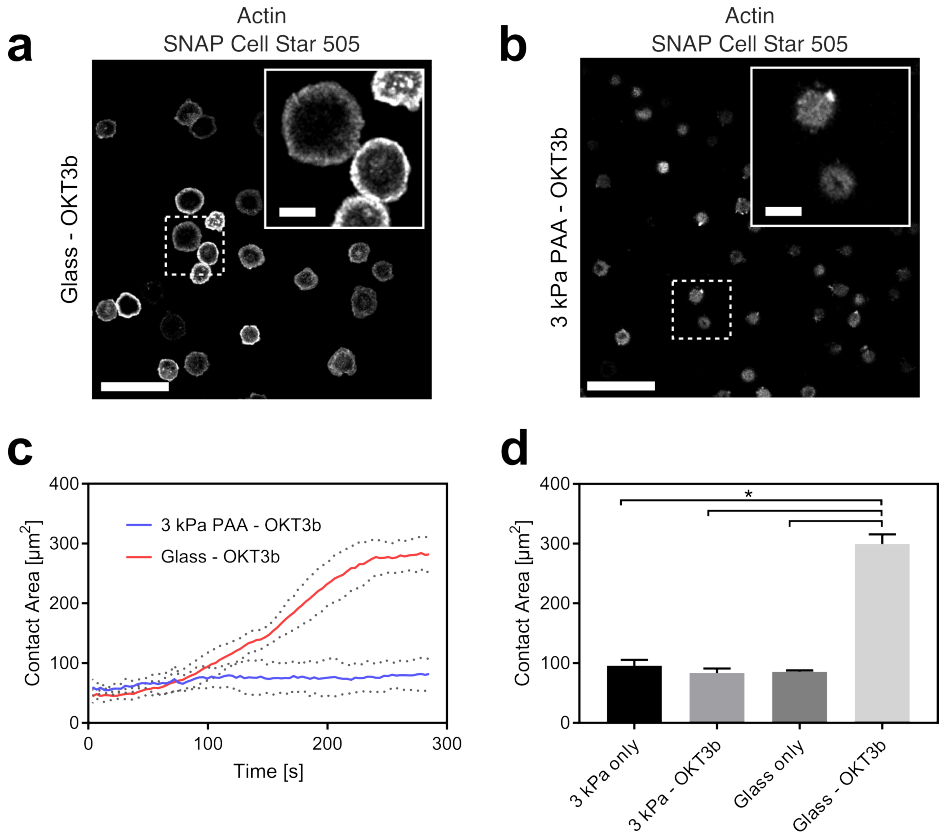


Fig. 5.8 Quantification of 1G4-TCR Jurkat T-cell spreading - **a**) Representative image of 1G4-TCR Jurkat T-cells spreading on a glass surface coated with OKT3. Scale bar is 50 µm. Inset shows zoom of dash line box, showing the dense ring of actin representing the lamellipodium of the spread T cell. Scale bar is 10 µm. **b**) Representative image of 1G4-TCR Jurkat T-cells on a gel surface coated with OKT3. Scale bar is 50 µm. Inset shows zoom of dash line box, showing the limited spreading of cell as compared to **a**). Scale bar is 10 µm. **c**) Quantification of T cell contact area of spreading and non-spreading cells over time. Each condition is the average of 10 cells. **d**) Quantification of T cell contact area is response to interaction with an uncoated 3 kPa gel, a gel coated with OKT3, an uncoated glass surface and a glass surface coated with OKT3. $*$ indicates a p-value of < 0.05. N $\sim$ 100 per condition.

The stiffness of 3 kPa was chosen such that the surface is of the same stiffness as a typical cell, thus mimicking the mechanical environment during a real T cell-APC interaction.[96] Figure 5.8a,b shows representative images of cells interacting with the glass cover-slip coated with OKT3, and the PAA gel coated with OKT3. On visual inspection, it is clear that the contact area of the cells on the glass cover-slip is greater compared to the gel. This can be further illustrated by analysing the dynamics of the cell spreading in both cases, with cells on the gel showing no increase in contact area over the course of 300 s. In contrast, cells on the glass cover-slip rapidly increase in contact area (see Figure 5.8c). Figure 5.8d shows the quantification of the cell contact area under each condition. It is clear from the results that the gel coated with OKT3b does not induce spreading. The contact area of the OKT3b coated and uncoated gel, as well as the uncoated glass is below 100 µm^2, in contrast to the glass cover-slip coated with OKT3b, which has a significantly higher contact area of over 300 µm^2. Despite the surface concentration of the antigen being comparable the gel does not induce activation (see Figure 5.7b,c). This presents a problem for the TFM measurement, as without successful activation, the forces present during IS formation and maintenance cannot be quantified. Thus, it was necessary to explore a range of parameters that may have been preventing activation.

There is evidence that the activation response of T cells is mechanosensitive, and this can be modulated by the stiffness of the substrate.[144] To examine whether substrate stiffness was influencing the T cell's ability to respond to the antigen coated gel, the spreading experiments were repeated for gels of 100 kPa and 200 kPa. Figure 5.9a shows the contact area of cells on the three different stiffness' and coated glass for comparison. For all three gels, no significant difference is observed in the contact area of the cell, again showing a contact area of below 100 µm^2 in all three cases.

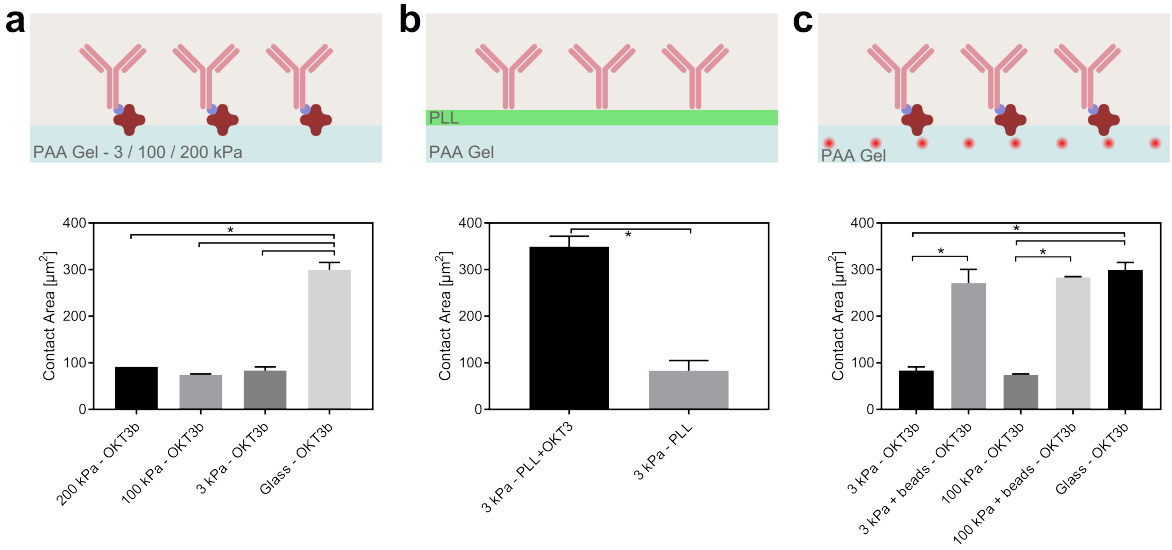


Fig. 5.9 Optimisation of 1G4-TCR Jurkat T-cell spreading - **a**) Upper - Schematic summarising the functionalisation scheme of the gel of different stiffness. Lower - Quantification of T cell contact area in response to interaction with a 200 kPa, 100 kPa, 3 kPa gel coated with OKT3. Glass coated with OKT3 is displayed as a positive control. **b**) Upper - Schematic summarising the functionalisation scheme of the gel functionalised with PLL and OKT3. Lower - Quantification of T cell contact area in response to interaction with a 3 kPa gel coated with PLL and OKT3 compared to a gel functionalised with PLL only. **c**) Upper - Schematic summarising the functionalisation scheme of the gel containing fluorescent marker beads. Lower - Quantification of T cell contact area in response to interaction with a 3 kPa gel containing no beads, a 3 kPa gel containing beads, a 100 kPa gel containing no beads and a 100 kPa gel containing beads. All are coated with OKT3. Glass coated with OKT3 is displayed as a positive control. $*$ indicates a p-value of < 0.05. N $\sim$ 100 cells per condition.

In the study by Hui *et al.* using TFM to measure forces during activation, the gel was first functionalised with Poly-L-Lysine (PLL) and subsequently coated with OKT3.[96] This method induced spreading, and allowed force generation to be quantified. Figure 5.9b shows the results of repeating this functionalisation scheme, resulting in spreading on the PLL + OKT3 gel at a level comparable to that observed on glass. Gel coated in PLL alone did not induce significant spreading.

In the previous experiments, the PAA gels did not contain the fluorescent beads necessary for a TFM experiment. To examine whether the addition of fluorescent beads to the gel would influence spreading, experiments were repeated now inserting fluorescent beads into the gel at the density necessary for the TFM experiment. This was done for a 3 kPa and 100 kPa gel. Figure 5.9c shows the contact areas of cells on the gel containing the fluorescent beads. Surprisingly, both the 3 kPa and 100 kPa gels induced spreading at a level comparable to the glass cover-slip. To explain this results,

it was necessary to examine more closely how the antigen is distributed on the surface of the gel when fluorescent beads are present.

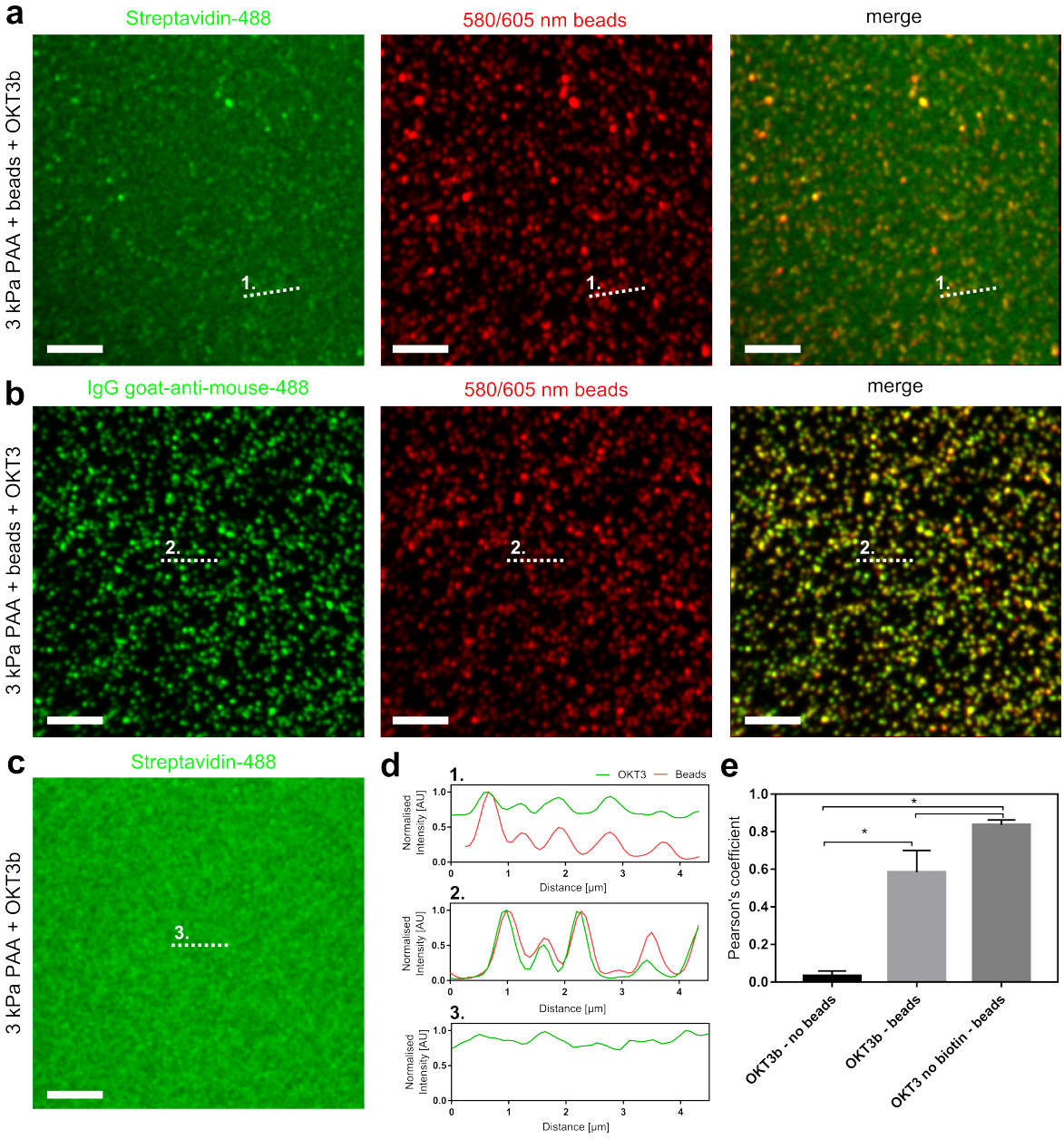


Fig. 5.10 Surface protein distribution - **a**) Left - Surface distribution of biotinylated OKT3 on a 3 kPa PAA, indicated using streptavidin-Alexa488, Middle - Distribution of fluorescent beads at the top surface of the gel. Right - merge of two images. Scale bar is 5 µm. **b**) Left - Surface distribution of non-biotinylated OKT3 on a 3 kPa PAA, indicated using IgG goat-anti-mouse-Alexa488, Middle - Distribution of fluorescent beads at the top surface of the gel. Right - merge of two images. Scale bar is 5 µm. **c**) Left - Surface distribution of biotinylated OKT3 on a 3 kPa PAA containing no fluorescent beads. Scale bar is 5 µm. **d**) Line profiles showing the distribution of antigen and beads for all three cases. **e**) Quantification of the co-localisation between beads and OKT3 in all three cases, using the Pearson's correlation coefficient. Note for the gel containing no beads, the correlation is calculated using the distribution of OKT3 an a random bead image, acting as a negative control for correlation. Error bars represent the standard deviation. $*$ indicates a p-value of < 0.05. N = 5 images per condition.

Figure 5.10 shows the distribution of OKT3 (green) for three different PAA gels. Figure 5.10a shows a gel containing beads, where it is evident that there is a good coverage of the surface, with most of the surface covered in a homogeneous layer of OKT3b. However, closer examination indicates that there are regions of increased OKT3b concentration and these regions coincide with the positions of the beads within the gel. These results suggest that the fluorescent beads are in some way influencing the distribution of the OKT3b. This becomes clearer when the gel is functionalised with an OKT3 that has not been biotinylated. Without biotinylation, the antibody will not be able to bind to the gel via the streptavidin-acrylamide, thus any binding observed must be non-specific. Figure 5.10b shows the resulting gel, indicating a clear co-localisation between the areas of high OKT3 concentration and the beads. If a gel is fabricated omitting the beads, as shown in Figure 5.10c, the distribution of OKT3 is homogeneous. The level of co-localisation between OKT3 and the beads can be quantified in all three cases by Pearson's correlation analysis, supporting our initial conclusion that the protein is non-specifically binding to the area of the gel containing the fluorescent beads (see Figure 5.10e).

Combining this conclusion from those drawn from the spreading experiments, it suggests that activation on the gel requires the antigen to be pre-clustered on the surface. In support of this, experiments investigating the effect of antigen surface distribution have shown the surface concentration of antigen to be an extremely important determinant of activation.[145] Thus, it suggests that the clustering effect of the beads results in an antigen distribution of sufficiently high density to induce activation. Note, this systems depends on the antigen as the sole molecule to maintain a contact between the cell and the substrate. This is an artificial scenario, since in a real T-cell-APC interaction, there are a number of molecules which contribute to the adhesive contact, including integrins such as LFA-3 and the co-receptors CD2, CD28

and CD4/8. However, since here forces experienced by the TCR-pMHC interaction are of primary interest, is it necessary to activate the T cell via the TCR interaction alone, something which is readily achievable on glass.

The mechanism responsible for the clustering of the antigen on gels containing beads in unclear. However, I speculate that it may be caused by the process by which the beads are loaded into the gel. As described previously, the beads are first attached to a glass cover-slip using PLL. This cover-slip forms half of the sandwich required to polymerise the PAA gel. During polymerisation, it is possible that PLL remains attached to the beads as it becomes incorporated within the gel meshwork, resulting in a local concentration of PLL surrounding the bead, which could explain the observed non-specific binding of the antigen surrounding the beads.

5.5.2 Gradual force generation

As was evident from the T-cell spreading experiments, combining OKT3 and PLL on the gel can induce spreading, whilst PLL alone does not (see Figure 5.9b). This method was used by Hui *et al.* to functionalise gels to measure forces during T-cell activation in a similar series of experiments to those presented here.[96] Here, the measurements conducted by Hui *et al.* were repeated, allowing verification and comparison of the behaviour of the two systems.

First, T cells were allowed to interact with a 1 kPa gel functionalised with PLL in combination with OKT3. As expected, spreading of the cell was observed (see Figure 5.11). After recording the interaction of the cell and the gel for 10 minutes, the forces were quantified by analysing the displacement of the beads via the PIV algorithm and forces calculated via FTTC (see Figure 5.11b,d,e,f). By quantifying the forces over time, it is possible to see how the forces present at the contact increase in magnitude and are focused in a ring around the periphery of the cell. By integrating the traction

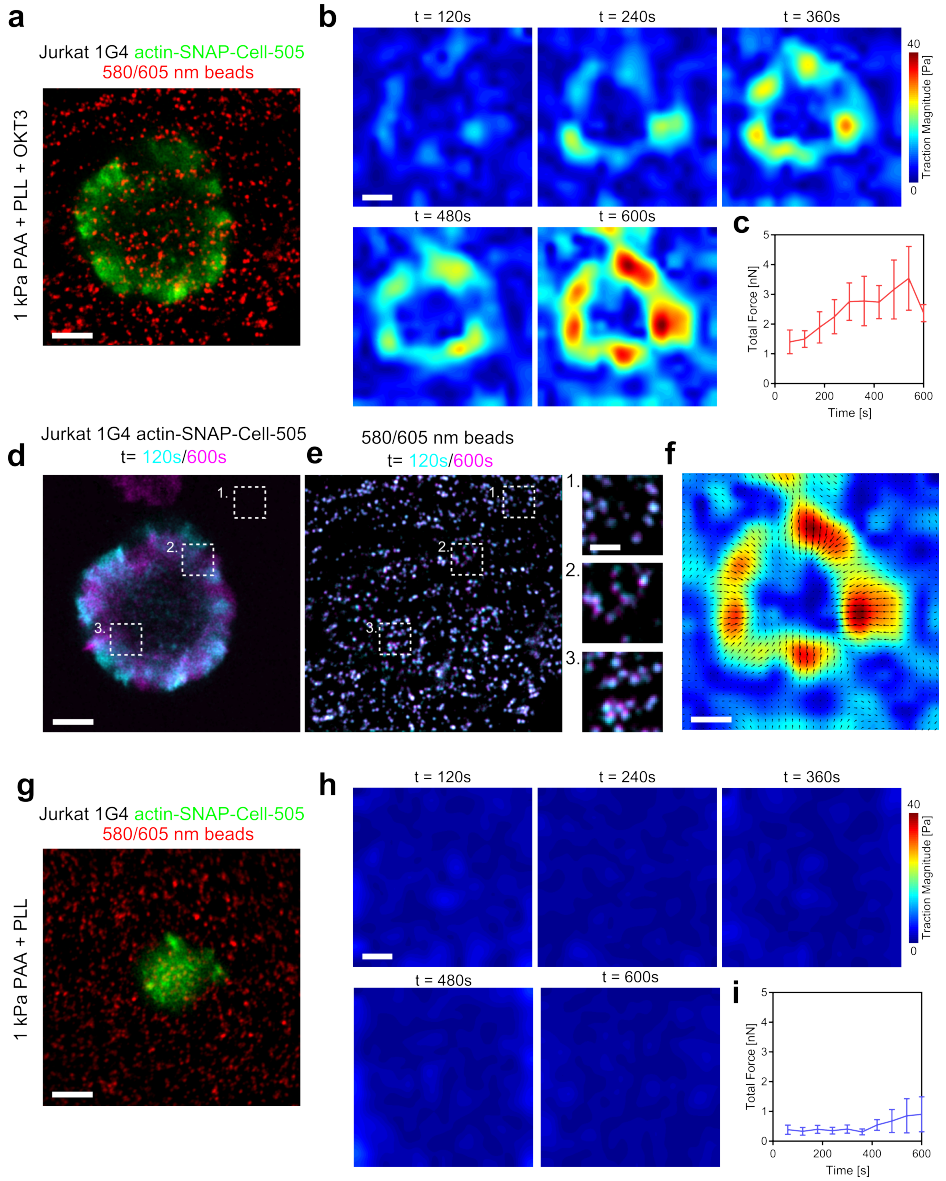


Fig. 5.11 Force induced by PLL and OKT3 - **a**) Actin labelled 1G4-TCR Jurkat T-cell activating on a gel coated in PLL and OKT3 and filled with red fluorescent beads. Scale bar is 5 µm. **b**) Magnitude of tractions developed by the T cell during activation on a PLL and OKT3 coated gel, with areas of high traction shown in red and low traction showing in blue. Scale bar is 5 µm. **c**) Quantification of the total force generated by the activating T cell as a function of time. Error bar shows the standard deviation and mean of 5 cells. **d**) A temporal projection of the actin distribution at the initial (cyan) and final (magenta) time point in the measurement. **e**) Left - A temporal projection of the bead distribution at the initial (cyan) and final (magenta) time point in the measurement. Right - Zoom in of the regions 1,2,3 indicated by dashed line boxes. The beads at the periphery (2,3) show a displacement towards the centre of the contact, where as beads outside the contact area (1) show little relative displacement between the two time points. **f**) Magnitude of the total tractions developed by the T cell during activation on a PLL and OKT3 coated gel, with areas of high traction shown in red and low traction showing in blue. Black arrows indicate the traction vectors. Scale bar is 5 µm. **g**) Actin labelled 1G4-TCR Jurkat T-cell activating on a gel coated in PLL only and filled with red fluorescent beads. Scale bar is 5 µm. **h**) Magnitude of tractions developed by the T cell during activation a gel coated with PLL only, with areas of high traction shown in red and low traction showing in blue. Scale bar is 5 µm. **i**) Quantification of the total force generated by the activating T cell as a function of time. Error bar shows the standard deviation and mean of 5 cells.

over the cell contact area we obtain the total force applied by the cell. Plotting the total force over time (Figure 5.11c) again it can be seen how the force generated by the cell increases as the contact with the gel surface matures. In contrast to this, on a gel functionalised with PLL alone, no force generation was observed over the duration of the recording (Figure 5.11g,h,i).

This result is in agreement with those attained by Hui *et al.*,[96] demonstrating that the system is behaving in a similar manner. The results indicate that T cells do indeed generate mechanical force during activation. The forces shown here are generated over the time-scale of minutes, pushing inwards towards the centre of the cell contact. Whilst this in an interesting results, the molecular interactions responsible for transferring the force to the gel are unclear. Because the surface is functionalised with both OKT3 and PLL, it is likely that the forces are being mediated by the PLL interaction, whilst cell signalling is specifically induced by the OKT3 (as no spreading or force is observed on gels coated in PLL alone). Because of this complexity, it is challenging using this system to determine the forces directly experienced by the signalling molecules, that is the antibody-TCR interaction, or pMHC-TCR interaction. Because of this difficulty, I returned to the gel functionalisation method that induced activation using only anti-CD3 antibodies or pMHCs to establish more directly the forces experienced by the antigen-TCR interaction at the IS.

5.5.3 Load-fail dynamics

As can be seen from Figure 5.12a, functionalising the gel with antigen in the presence of beads induces activation, resulting in spreading of the T cells on the gel surface. By tracking the displacement of the beads over time, this time using the SPT algorithm, it was clear that forces were also being transferred to the gel under these conditions (see Figure 5.12b). However, the nature of the bead displacements were different to

those observed in the previous experiments using PLL in combination with OKT3. It was evident on visual inspection that the beads are undergoing a very specific type of motion. At the periphery of the cell, in the region of the lamellipodium, the beads move in the direction of the actin flow towards the centre of the cell. After a few seconds, the beads abruptly return to their original position. This elastic bead motion has previously been observed in a study of traction forces generated by neuronal growth cones, where the motion was termed 'load-fail' dynamics.[146] The authors of the study interpret the events as follows. The gel is first loaded with force via a molecular interaction between the cell and the gel, hence the bead displacement undergoes a slow loading phases. This is followed by a failing event, where the interaction between the cell and the substrate is ruptured, causing the gel to elastically return to its equilibrium position.

This motion can be more clearly visualised and quantified if the track is projected along its major axis. This was done by applying a linear fit to the track and projecting each vector of the track onto the unit vector defined by the linear fit (see Figure 5.12c,d), resulting in a plot of the load-fail motion (see Figure 5.12e). It should be noted that not all beads moved in this way, with some remaining stationary over the duration of the measurement (see Figure 5.12f).

The load-fail trace indicates that the time-scale of the forces observed here are on the order of seconds. This is much shorter than those observed on the gel coated with PLL and OKT3, which were on the order of minutes (see Figure 5.11). This difference in time-scale suggests that a different cellular process is responsible for the force generation in each case. The gels used in the load-fail experiment were only functionalised with OKT3, suggesting that the forces observed are being transmitted via the OKT3-TCR interaction. This was in contrast to the experiments using PLL, where it is unclear which molecular component is responsible for force transmission.

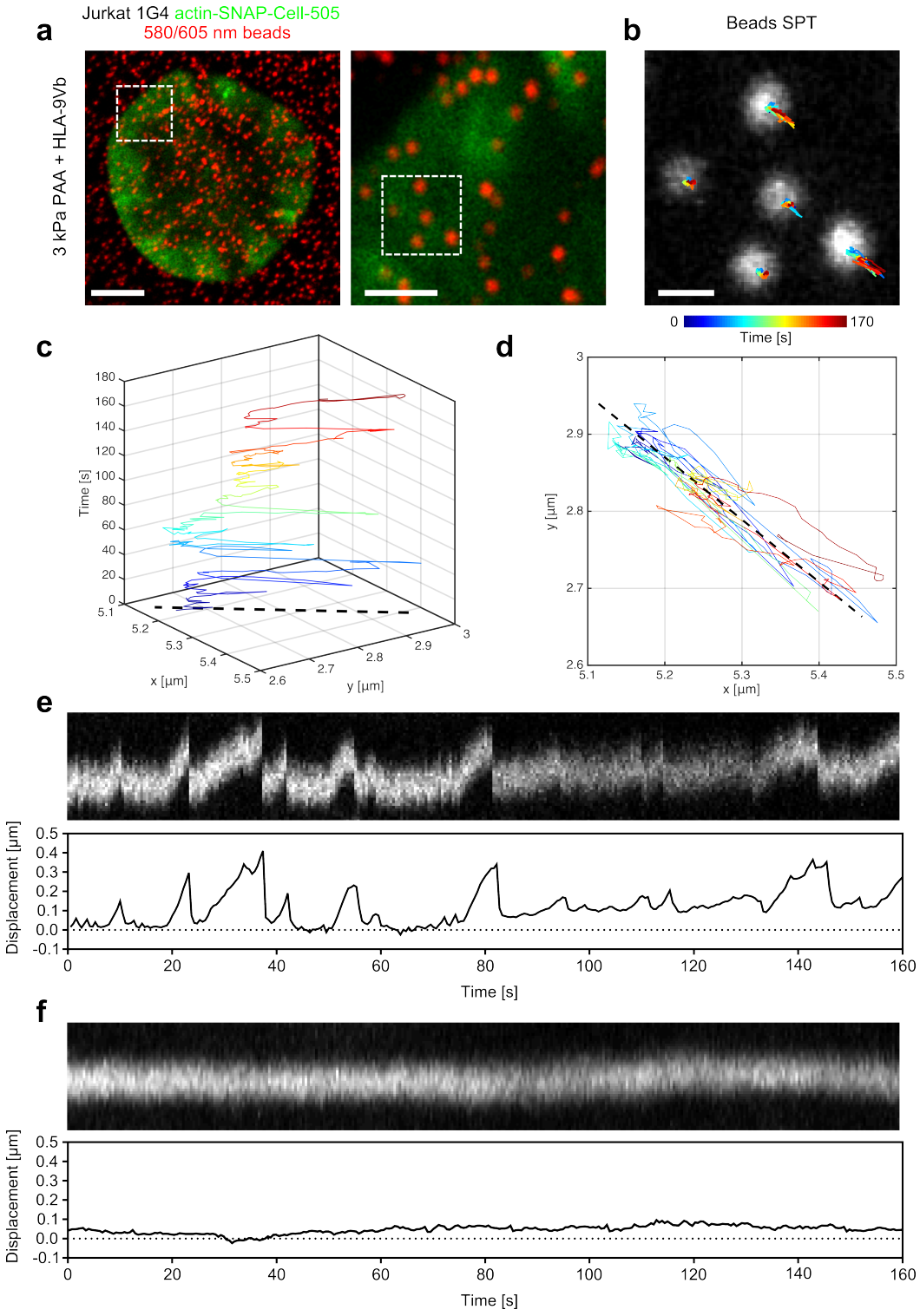


Fig. 5.12 Load-fail dynamics of 1G4-TCR Jurkat T-cells - **a**) Left - Actin labelled 1G4-TCR Jurkat T-cell activating on a gel coated with HLA-9V and filled with red fluorescent beads. Scale bar is 5 µm. Right - Zoom in of dashed region left. Scale bar is 2 µm. **b**) Zoom in of dashed region **a**)-right showing SPT of the beads within the gel. Tracks are temporally colour coded from initial time point in blue to final time point in red. Scale bar is 0.5 µm. **c**) 3D representation of a representative bead track. The xy displacement of the bead is shown expanded along the third temporal axis. Again, the track is colour coded from initial time point in blue to final time point in red. The dashed line at t= 0 represents a linear fit to the track. **d**) Temporal projection of the bead track colour coded in the same way and showing again the dashed line representing the linear fit. **e**) Upper - kymograph of the fluorescent image showing the load-fail events over time. Lower - the corresponding cumulative bead displacement as calculated by SPT projected onto the linear fit displayed in **c**) and **d**). **f**) Equivalent to **e**) but for a bead showing no displacement.

This result provides the necessary condition to measure the forces directed through the TCR at the IS, allowing an investigation of the relationship between force generation and antigen kinetics.

Next, the previous measurements were extended to systematically quantify the load-fail dynamics in response to each of the four antigens. For each bead, SPT was used to quantify the bead displacements. Each load-fail event was then segmented from the track and parametrised. The load region was fit using a linear model and values of the gradient (v), load time (dt) and load displacement (dx) extracted (see Figure 5.13a,b). This was done systematically for bead tracks across all antigens and the results plotted in histograms (see Figure 5.13c,d,e and f).

Given the difference in binding kinetics of each antigen, specifically the difference in k_{off}, we would expect each pMHC or antibody to be bound to the TCR for differing times. Under the current load-fail model, this would result in a difference in the observed load time, dt, since the antigens with higher k_{off}, for example HLA-4D, are able to sustain the loading phase for a shorter period of time than for example, UCHT1. This would also result in a reduced displacement of the bead during the loading phase and hence a reduction in dx. By analysing Figure 5.13, HLA-4D, OKT3 and UCHT1 show an exponential-like distribution of dt, while HLA-9V is more peaked. This is also evident in the distributions of dx and v, which shows again HLA-4D, OKT3 and UCHT1 showing an exponential distribution, while HLA-9V is peaked. The data does not show a clear pattern, but in general the median values for each of the three parameters are similar. Given that the binding kinetics of UCHT1 and HLA-4D differ by order 100 (see Figure 5.1), it is apparent that the data cannot be explained by the kinetics of the antigen alone. Notably, exponential distributions suggest a random dissociation process while peaked Poisson-shaped distributions arise from non-random dissociation processes that are not linear in time. Intriguingly, the

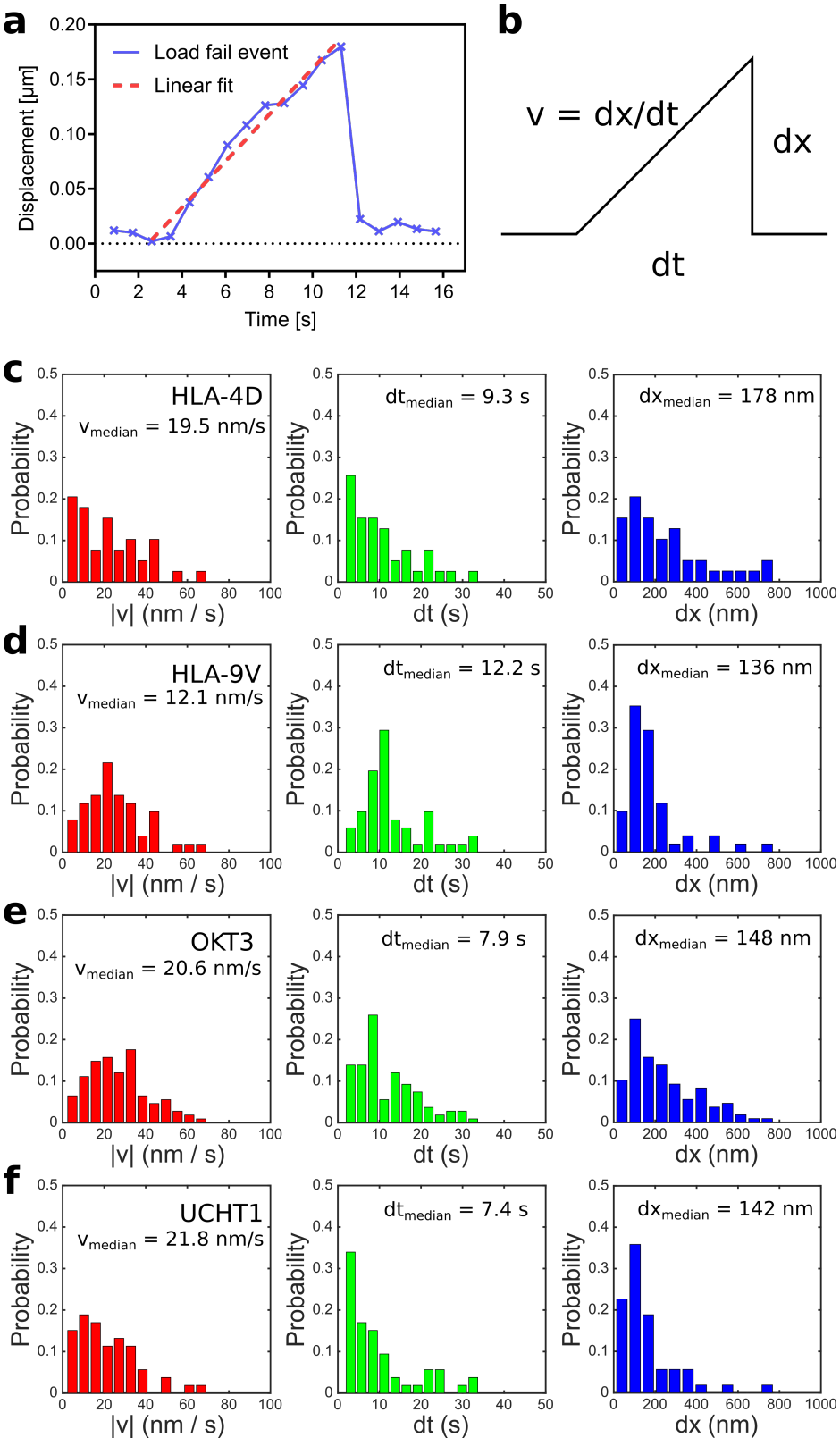


Fig. 5.13 Load-fail dynamics across all antigens - **a**) Plot showing a representative load-fail event (blue), superimposed with a linear fit over the load region. **b**) Parametrisation of the load-fail event, where dt is load time, dx is the load displacement and v is the load velocity dx/dt. **c,d,e,f**) Quantification of load-fail dynamics across all four antigens, HLA-4D, HLA-9V, OKT3 and UCHT1. In each case a histogram is plotted of v, dt, and dx. Data acquired from ∼ 10 cells per condition, with an average of 5 load-fail events per cell.

distributions of the length-scales displayed consistently Poisson-shaped distributions with a comparable median value while the time-scales dynamically changed, suggesting that the length-scale is constant for the different antigen peptides. This means that the distance at which TCR-pMHC complexes are interacting are constant at the IS. Constant length-scales for the agonists may have profound effects on signalling such as Zap70 recruitment and the spatial-temporal organisation of the IS. However, more statistics are required to draw firmer conclusions from this data.

Up to now, a quantification of the load-fail events is given in terms of the velocity, v, the time-scale, dt, and the length-scale, dx. In principle, given our knowledge of the elastic properties of the gel, this should be sufficient information to calculate the force required to cause such an event. However, as was recognized by Chan et al.,[146] the theoretical treatment of such events is challenging. If every load-fail event is considered to be an independent force generating event, then each can be modelled as a point force acting tangentially to the gel surface. This represents a classical problem in elastic theory, known as the Cerruti Problem.[147] Since we are only interested in the 1D case, where the point force acts along the line of the displacement, the force-displacement relationship can be simplified along the axis of the load fail event (see Appendix A), resulting in the following equation:

$$u_1(x_1, 0, 0) = \frac{F(1+\nu)}{E\pi x_1} \tag{5.1}$$

This equation can be rearranged to obtain the magnitude of the point force at the origin, F,

$$F = \frac{E\pi x_1 u_1}{(1+\nu)} \tag{5.2}$$

where E and ν are the elastic modulus and the poisson ration respectively, x_1 is point along the axis of the force where the strain $u_1(x_1, 0, 0)$ is measured. To accurately

calculate the point force, F, the distance between the application of the point force, which defines the origin (i.e. $x = 0$) and the position at which the displacement is measured, must be known. In the current experimental system, the position at which the displacement of the gel is measured is defined by the position of the bead. Thus to calculate the force, the position of the point force in relation to the bead must be known. In our system, given the clustered distribution of the antigen around the beads (see Figure 5.10), it is reasonable to assume that the point force is being applied at the position of the bead. In the current formulation of the Cerruti problem, this results in $x_1 = 0$, i.e. the point at which the displacement is measured coincides with the point of application of the point force. This presents a problem, as the relationship governing the force and displacement (Equation 5.2), implies that if $x_1 = 0$ then $F = 0$. This highlights a failing in the classical theory, where if we look at Equation 5.1, $u_1(x_1 = 0, 0, 0)$ becomes infinite which is not representative of the physical system. While there have been attempts to address this problem with the field of elastic theory, it remains an active area of research beyond the scope of the work presented here, thus for the purposes of this analysis, we must rely on the current parametrisation of load-fail events.[148,149]

5.5.4 STFM load-fail dynamics

The preceding data showing force generation on both long and short time-scales utilised classical TFM, only using confocal microscopy. Figure 5.14a,b and c demonstrates the use of STFM applied to measure load-fail dynamics. While the higher resolution offers improved ability to localise and track the beads, the higher laser powers result in a higher rate of photo-bleaching, meaning that after 100 s recording, the fluorescence intensity has reduced by more than half, making accurate tracking of the beads challenging (see Figure 5.14d). In comparison to confocal, recordings for the same

length of time, the fluorescence intensity had only reduced by around 10 %. For the case of load-fail dynamics, the measurement relies on being able to measure at high frames rates for an extended period of time, therefore in this case, confocal microscopy is still favoured.

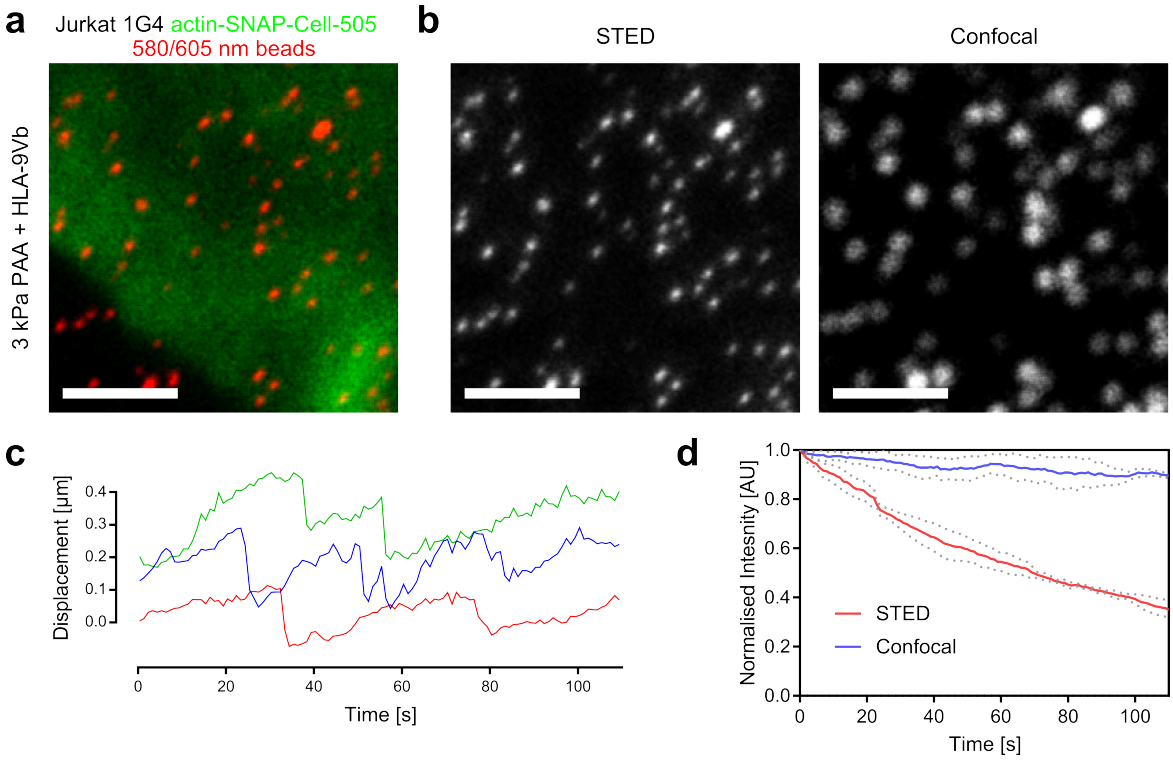


Fig. 5.14 Load-fail dynamics of 1G4-TCR Jurkat T-cells measured by STFM - **a**) Actin labelled 1G4-TCR Jurkat T-cell activating on a gel coated with HLA-9V and filled with red fluorescent beads imaged by STED microscopy. Scale bar is 2 µm. **b**) Side by side comparison of the distribution of beads imaged by STED (left) and confocal (right). Scale bar is 2 µm. **c**) SPT of STED imaged beads, showing load-fail events. **b**) Quantification of photo-bleaching of the red fluorescent bead images as imaged by STED and confocal. Both intensity traces are normalised to the initial intensity. Error bars are the standard deviation of the mean of 5 measurements in each case.

5.5.5 Load-fail dynamics is dependent on actin flow, but not myosin IIA

The directionality of the beads undergoing load-fail dynamics correlates with the motion of the actin cytoskeleton, suggesting it is the retrograde flow of actin that is responsible for the observed forces. To validate this, cells interacting with the gel were treated with the actin perturbing drug, Jasplakinolide.[107] Jasplakinolide selectively

stabilises actin filaments, preventing filaments from growing or shrinking, thus stopping retrograde flow. On treating the cell with the Jasplakinolide, the flow of actin stops immediately as expected, as can be seen in Figure 5.15b. By analysing the motion of the beads before an after treatment it is apparent that the load-fail dynamics is also inhibited, in support of the hypothesis that it is the retrograde flow of actin that is responsible for the load-fail dynamics (see Figure 5.15c).

Studies have shown that myosin IIA may also contribute to force generation and the organisation of molecules at the synapse.[25,40] To examine whether myosin IIA was contributing to the observed load-fail dynamics, cells were treated with the Rho-kinase (ROCK) inhibitor, Y27632. As can be seen from Figure 5.15e and f, the actin flow and load-fail dynamics are unaffected following the addition of Y27632, suggesting that myosin IIA does not play a role in the forces responsible for the load fail-dynamics. Note, that the results of these experiments do not rule out the role of myosin in the observed gradual generation of force. Further experimentation would be required to establish the molecular events driving the gradual generation of force at the IS.

5.6 Summary

In this chapter, I have first validated the activation response of the engineered 1G4-TCR Jurkat T-cell system, using the release of calcium as an indicator of the level of triggering induced by a range of antigens. The results confirmed that the 1G4-TCR Jurkat T-cell can be activated by the desired range of antigens and demonstrated an antigen dependence of the calcium response, with more strongly binding antigens inducing more single peaked responses and weakly binding antigens tending to produce an oscillating calcium release. The calcium response was then linked to the response of the actin cytoskeleton, indicating that a single peaked calcium response is associated with actin polymerisation and cell spreading, where as an oscillating response was not

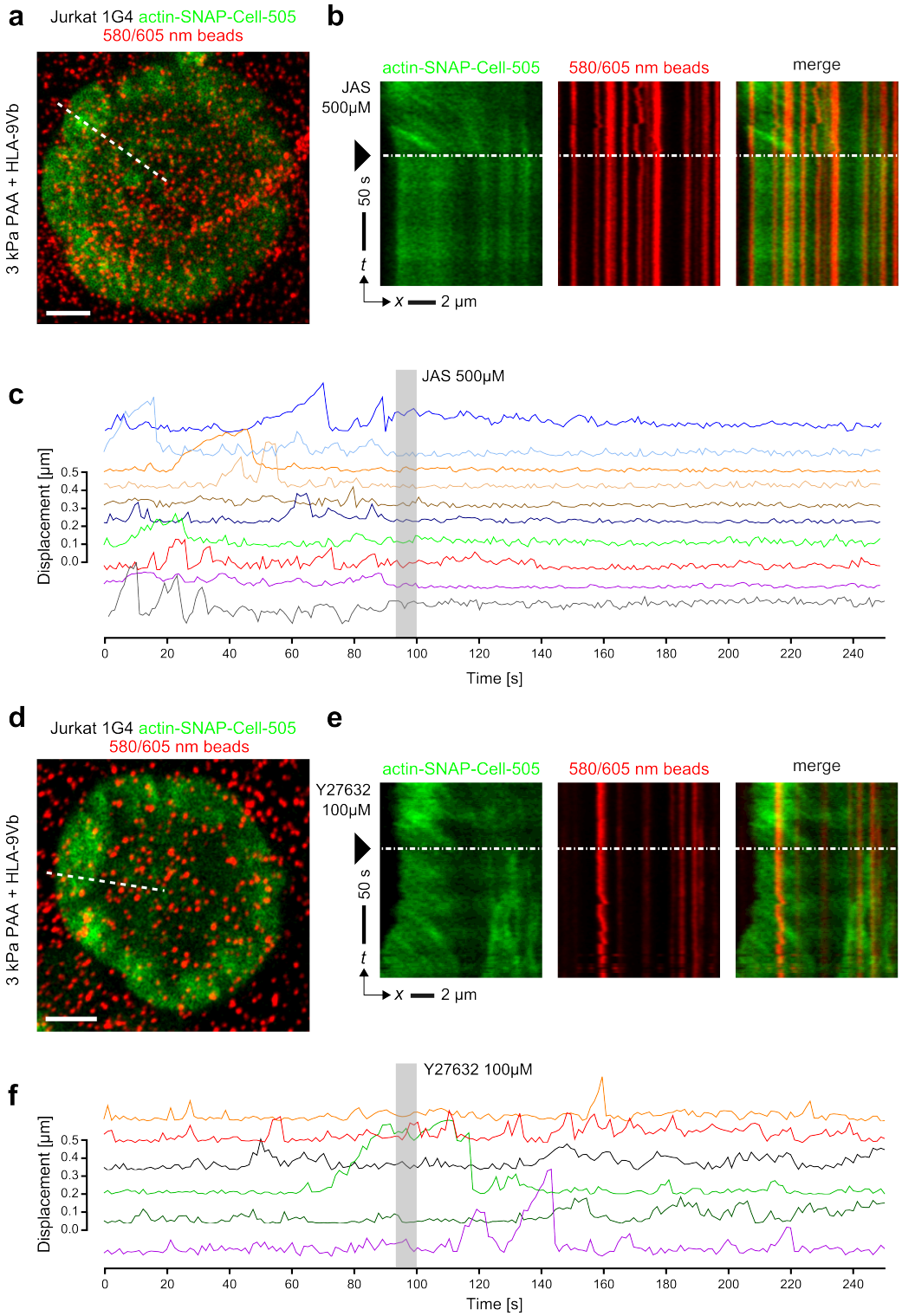


Fig. 5.15 Jasplakinolide and Y27632 treatment during load-fail dynamics- **a**) Actin labelled 1G4-TCR Jurkat T-cell activating on a gel coated with HLA-9V and filled with red fluorescent beads. Scale bar is 5 µm. **b**) Kymograph showing the actin (left) and bead (middle) dynamics before and after addition of 500 µM Jasplakinolide. The time point of addition of the drug is denoted by the black arrow and white dashed line. **c**) Load-fail plot showing bead dynamics before and after addition of Y27632 as measured by SPT. **d**) Actin labelled 1G4-TCR Jurkat T-cell activating on a gel coated with HLA-9V and filled with red fluorescent beads. Scale bar is 5 µm. **e**) Kymograph showing the actin (left) and bead (middle) dynamics before and after addition of 100 µM Y27632. The time point of addition of the drug is denoted by the black arrow and white dashed line. **f**) Load-fail plot showing bead dynamics before and after addition of Y27632 as measured by SPT.

associated with any change in the actin cytoskeleton. This characterisation makes clear an important link between calcium signalling and actin rearrangement. From this point on in the chapter, the activation response is primarily measured by analysing the behaviour of actin.

Next, by analysing the global rearrangements of actin during T cell activation using LLSM, I was able to observe in all three spatial dimensions how the events following the initial contact of a T cell with an activating surface can be divided into three phases. The first stage is characterised by a rapid spreading of the T cell on the surface and formation of the actin-rich lamellipodium. This is followed by a stabilisation of the contact area and undulation of the lamellipodium. Finally, the contact area decreases in size and cell rounds up to its original spherical state, retracting the lamellipodium. These results confirm the drastic nature of actin reorganisation during IS formation, giving further support to the concept that generation of mechanical force by the actin cytoskeleton is necessary for the successful initiation and maintenance of the IS.

I next sought to quantify in more detail the dynamics of the actin cytoskeleton within the IS, specifically investigating whether the retrograde flow velocity of actin was dependent on the kinetics of the antigen presented to the cell. To do this, I employed kymograph and optical flow analysis to systematically quantify actin retrograde flow velocity in the lamellipodium of activating cells. This revealed a dependence on the antigen, with weakly binding antigens resulting in faster flow velocity. This is an interesting result, as it provides indirect evidence of a coupling between the TCR and the cytoskeleton, suggesting that weakly binding antigens immobilised on the cover-slip provide less mechanical resistance to the flow of actin, resulting in faster retrograde flow. In addition to these measurements, I employed TIRF-SIM microscopy to analyse the distribution and organisation of actin across the IS. This revealed three structurally distinct zones of actin: the periphery is occupied by a dense meshwork of actin forming

the lamellipodium, agreeing with my observations from confocal microscopy. Closer to the centre of the IS there exists a more coarse network of actin, resembling what is commonly referred to as the lamellum in migrating cells. In the centre of the IS the actin is even more coarse. The three zones of actin also differ in their actin flow velocity, with the fastest flow observed in the lamellipodium. This result agrees well with previously published work,[40] and suggests that given the coupling between the actin and TCR indicated by the previous measurement, that the forces that the TCR experiences may be dependent on the radial distance at the IS.

To firmly establish the level of force generation at the IS, I employed TFM to directly measure the forces experienced by the TCR during activation. This was first demonstrated using a PAA gel functionalised with PLL and the antigen, OTK3. In this scenario, mechanical force generation could be measured, which increased gradually as the IS matured, agreeing well with previous measurements.[96] However, due to the presence of PLL, it was unclear which molecules were experiencing mechanical force. Thus, I optimised the activation protocol to allow T cell spreading in the presence of antigen alone. This revealed a strikingly different pattern of force generation, in the form of load-fail dynamics. Concentrated under the lamellipodium, load-fail events consisted of a gradual displacement of a bead in the direction of the actin flow, followed by a sudden elastic return to equilibrium. By treating with actin and myosin perturbing drugs, it was evident that the load-fail events are likely dependent on the flow of actin, but are independent of the myosin contraction. The interpretation of the load-fail events measured for the four antigens remains challenging due to complex and poorly understood couplings involved in the transfer of force from the actin cytoskeleton to the PAA. In total there are three couplings to consider. The first is the link between the antigen and the gel, which in the load-fail case is maintained by a biotin-streptavidin link, and can be assumed to be comparatively stable. The next link is the coupling of

primary interest, that is the binding between the antigen and the TCR. The third is the link that exists between the TCR and the actin cytoskeleton. This is perhaps the least understood coupling and the most difficult to interpret. Under a fail event, any one of these couplings could in theory be rupturing, therefore without further investigation, the exact mechanism causing the load-fail event is unknown. However, the length-scales of the load-fail data appeared to be constant for the different antigen peptides. Constant length-scales for the agonists may have profound affects on signalling such as Zap70 recruitment and the spatial-temporal organisation of the IS. Further investigations will be required to more firmly establish these conclusions.

Chapter 6

Discussion

6.1 Summary

In the first part of the thesis I developed and implemented the tools necessary to measure the mechanical forces present during T-cell activation. To this end, I have increased the spatial resolution of the well established technique of TFM using the super resolution technique STED, increasing the sampling density of the displacement field 5-fold and increasing the accuracy and resolution within the traction field. The capabilities of STFM have been demonstrated using computer simulations and in two biological examples, namely HeLa cell focal adhesions and activating RBL cells. This represents an important advance in the accuracy of a widely used technique. As previously discussed, the increased resolution gained from STFM is better suited to biological systems in which force generation is on the time scale of minutes, allowing the use of reduced frame rates and hence limiting the effects of increased photo-bleaching and scan times associated with STED. While being able to observe a higher level of detail within the fluorescent bead images, facilitating the tracking of a higher number of beads than confocal imaging would allow, these limitations ultimately meant that

STFM was not yet well suited to measuring forces generated by T cells where bead displacements had to be measured over long periods of time. However, the key concept of STFM is to increase accuracy by increasing sampling, thus the technique can be taken forward using a microscopy modality that overcomes the limitations presented by STED. One such technique is SIM,[150] where an increase in spatial resolution is gained without the loss of temporal resolution and photo-bleaching. Whilst the increase in spatial resolution is not as dramatic as STED, it could prove a useful combination in future work (see Future Work).

In the second part of the thesis I used TFM to quantify the forces during T-cell activation. Before quantifying forces it was necessary to characterise the activation response of the 1G4-TCR Jurkat T-cell system. Quantifying Ca^{2+} release and actin spreading in response to an array of antigens with differing binding kinetics, showed differences in the activation response, with more strongly binding antigens showing increased single peak calcium responses and actin spreading. I then examined the global cytoskeletal changes that occur on activation using LLSM, and extended this using TIRF-SIM to investigate how the flow rate of the actin cytoskeleton is dependent on the antigen presented to the T cell. This revealed a feedback between the antigen and actin retrograde flow velocity, with strongly binding antigens resulting in a slower velocity.

Whilst these results indirectly show that the actin cytoskeleton is applying a force to the TCR-antigen interaction, there remained a need to directly measure the forces. Here, I applied TFM to measure the force generation of T cells under various conditions. In the presence of PLL in combination with an antigen such as OKT3, a gradual generation of force was observed at the IS, developing over the period of minutes. In contrast, when the cell was exposed to antigen alone, the force generation observed using TFM was strikingly different. Here, we observed fast load-fail events

mediated by the TCR-antigen interaction. Quantification of load-fail events for all antigens showed consistent dynamics across all antigens. Using drugs to stabilise actin filaments resulted in an arrest of the actin flow and the load-fail events, indicating their dependence on the retrograde flow of actin at the IS. Deactivating myosin did not appear to hinder the load-fail events.

Taken together, the results indicate that there is indeed force generation at the IS and it is spatially and temporally complex. At the periphery, where actin is most dynamic, undergoing retrograde flow at around $100\,\mathrm{nm\,s^{-1}}$, we observe load-fail events. This suggests that in this region, the TCR-MHC interaction is experiencing mechanical force on the second time-scale. Because of the theoretical difficulties presented by the Cerruti problem, it is not possible at this stage to explicitly calculated the forces experienced by the TCR. Despite this, it is apparent that the qualitative nature of the force generation is very different from those observed when PLL is present. In contrast to the observed load-fail dynamics, when antigen is combined with PLL, we observed a slow generation of force across the IS, indicating a global contraction of the cell as the IS matures. These results agree with the measurement of actin during the calcium assay and using LLSM, which all showed a period of spreading, stability and then contraction. The results also agree well with previous measurements of force, particularly those by Hui *et al.*. However, whilst their findings also showed an actin dependence, the nature of the gel functionalisation likely meant that any load-fail events were obscured. Whilst using PLL appears to mask certain details, it may be indicative of the true T cell-APC interaction, where the adhesion between the two cells is mediated by an array of molecules, including LFA-1-ICAM1 and LFA-3-CD2. These interactions, which are more numerous than the TCR-MHC interaction, may serve to transmit the gradual forces, leading to a contraction of the IS as the contact matures.

Simultaneously, fast load-fail event transmit the forces necessary to traffic the TCR micro-clusters to the centre of the IS.

Given the difference in affinity between the antigens presented to the T-cells, and the difference observed in the actin retrograde flow, one would expected to see differences in the load-fail events for different antigens. This was not the case, with no significant difference observed. Interestingly, a consistent length-scale was evident across all antigens, suggesting that despite differences in affinity, the TCR is bound to the antigen for a consistent length scale. This may have important implications for the level of signalling induced by each antigen. However, the interpretation of these results are challenging due to the complex nature of coupling between the gel substrate and the actin cytoskeleton. While drug treatments indicate that it is indeed actin flow that is responsible for the load-fail events, the exact molecular mechanism controlling the dynamics in unclear. To investigate this further two strategies should be followed. The first would be to combine TFM measurements with imaging of the TCR itself. In doing so, the localisation of the load-fail event and the TCR could more firmly be established and correlated. If the location of the TCR remains fixed to the position of bead, it suggests that the failing event is caused by a rupturing of the coupling between the cytoskeleton and the TCR. Conversely, if the TCR is displaced in the direction of the actin flow following a fail event, it suggests that it is the rupturing of the coupling between the TCR and the antigen that is taking place. Further to this, to investigate the nature of coupling between the TCR and the actin cytoskeleton, pharmacological agents that disrupt this coupling should be used. One such drug is, NSC 668394, an inhibitor of ezrin, a molecule crucial in linking the actin cytoskeleton to the membrane. It is known that NSC 668394 treatment reduces membrane tension by decreasing the number of molecular links between the membrane and cortex.[151] Thus, if the TCRs experience a force due to a frictional coupling between the membrane

and the cytoskeleton, NSC 668394 might serve to decrease this coupling, leading to an increased membrane-cortex distance, and a decrease in the observed force. This would shed light on the nature of coupling between actin and the TCR.

As outlined in chapter 2, a number of roles have been suggested for mechanical force during activation, including during triggering and IS formation and continuation. Whilst the results presented here do not directly support any specific model, they do suggest that any model of activation must at least be robust to the presence of mechanical force. That is to say, if they do not actively use mechanical force, they must be able to act successfully under the influence of mechanical force.

6.2 Future work

There are a number of possible extensions to the work presented in this thesis. In this section I discuss those extension, beginning with the work on STFM.

As previously mentioned, a limiting factor of STFM is the increased photo-bleaching and scan times required using STED. This is problematic for some systems, including the T-cell measurements presented in this work where long measurement times are needed. Whilst this could be remedied by improving the stability of the fluorescent beads, another solution could be the use of SIM in an analogous role to STED, offering an increase in spatial resolution compared to confocal microscopy, potentially less photo-bleaching and allowing faster image acquisition owing to it being a wide-field, as opposed to a scanning technique.[150] Nevertheless, photo-bleaching will also for SIM set an ultimate limit, since several image frames have to be recorded to create a final image. Further, optical aberrations due to imaging deep into the gel might distort the quality of the SIM recordings. This will need to be tested.

Throughout this work, I have only considered those forces acting tangential to the PAA gel surface. For all cases where TFM has been applied throughout the work, this

appears to have been a reasonable assumption given that no defocusing of the bead imaging was observed due to forces normal to the PAA surface. However, TFM has been widely implemented to measure forces normal to the gel surface by measuring the displacement of the beads in all three spatial directions.[152] TFM has also been extended to measure forces of cells embedded within 3D matrices.[138] In all cases, the accuracy of force recovery is limited in the same way as the 2D case, where the finite PSF limits sampling density and hence traction accuracy and resolution. In a straightforward extension of 2D STFM, by using a technique that increases the optical resolution in all three spatial dimensions, the accuracy and resolution of 3D-TFM could also be improved. One such technique is 3D-STED, where the depletion PSF is extended to the axial direction, allowing resolutions of below 100 nm in all directions,[153] allowing higher sampling and hence higher accuracy.

In addition to extension of the STFM method, there are a number of directions in which to take the work presented in chapter 5.

As mentioned, further work is required to establish the molecular mechanism underlying the observed load-dynamics. This would involve quantification of the TCR dynamics during the formation of the IS on the PAA gel as well as the use of further specific pharmacological agents to pinpoint the components of the cytoskeleton contributing to force generation. In addition to this, the forces generated in the presence of PLL and antigen are on a different time scale to the load-fail events, suggesting a different molecular mechanism underlying their generation. LLSM imaging identified the formation of a ring of myosin above the IS as the contact developed. This provides tentative evidence that myosin contraction may be responsible for the global contraction of the IS on the time scale of minutes. To firmly establish this, pharmacological agents targeting myosin activity such as Y27632 or blebbistatin, should be used in combination with TFM to examine their effects on force generation.

In this work, I have focused on force generation via the TCR-antigen interaction. As previously discussed, there are a number of other important molecular interaction that occur during activation. Of particular interest is the role of integrins, for example the LFA-1-ICAM1 interaction. Recent work has shown that forces generated by actin present at the T cell-APC contact can induce a conformational change and hence activation of the integrin LFA-1.[154] Crucially, this study examined the mobility of the molecules on the surface of APC, finding that decreased mobility led to an increase in integrin activity. This provides evidence that not only is the cytoskeleton of the T cell important during activation, but also that of the APC. Using the TFM system, one could investigate what forces LFA-1 is exposed to during IS formation by functionalising the gel surface with ICAM-1. In this way, one could establish how integrins react to and contribute to force generation at the IS.

Two peptide loaded MHC molecules that interact with the 1G4-TCR were used in this study, in addition to the anti-CD3 antibodies, UCHT1 and OKT3. Other studies involving the 1G4-TCR have used a wider array of peptides specific to the 1G4-TCR.[101] To strengthen the conclusions drawn from this work, one could extend the current study of actin flow velocity and force generation in response to a wider array of antigens with intermediate binding kinetics to the ones used here.

6.3 DPhil Publications

M.P. Clausen, H. Colin-York, C. Eggeling, M. Fritzsche. Measuring the membrane-cortex distance in living cells by super-resolution microscopy., **Journal Physics D** (under review)

H. Colin-York, C. Eggeling, M. Fritzsche. Dissecting mechanical force in living cells by super-resolved traction force microscopy, **Nature Protocols** (Accepted).

H. Colin-York, D. Shrestha, J. H. Felce, D. Waithe, E. Moeendarbary, S.J. Davis, C. Eggeling, and M.Fritzsche. Super-resolved Traction Force Microscopy (STFM)., **Nano Letters**, 16 (4), pp 2633–2638, DOI: 10.1021/acs.nanolett.6b00273, 2016.

H. Colin-York, V. T. Chang, J.H. James, E. Betzig , C. Eggeling, D. Li, and M. Fritzsche. Cortical actin patterning drives antigen-stimulated granule secretion. **Nature Cell Biology** (under review).

D. Gutowska-Owsiak, M. Fritzsche, J. B. de la Serna, E. I. Podobas, M. Leeming, H. Colin-York, C. Eggeling, and G. Ogg. Orchestrated control of filaggrin-cytoskeletal scaffolds underpins skin barrier formation., **Journal of Allergy and Clinical Immunology** (under review)

M. Fritzsche, D. Li, H. Colin-York,V. Chang, J. H. Felce, G. Charras, E. Betzig, and C. Eggeling. Dynamic pattern formation drives actin cortex assembly., **Nature Comm**, (Accepted).

M. Fritzsche, R. Fernandes, V.T. Chang, H. Colin-York, M.P. Clausen, J.H. Felce, S. Galiani, C. Erlenkämper, A.M. Santos, J.M. Heddleston, D. Waithe, J. Bernadino de la Serna, B.C. Lagerholm, T.-L. Liu, T.L. Chew, E. Betzig, S.J. Davis, and C. Eggeling. Cytoskeletal actin dynamics shape a ramifying actin network underpinning immunological synapse formation., **Science Immunology** (under review).

M. Fritzsche, R.A. Fernades, H. Colin-York, A. M. Santos, S.F. Lee, B.C. Lagerholm, S.J. Davis and C. Eggeling. CalQuo: automated, simultaneous single-cell and population-level quantification of intracellular Ca 2+ responses., **Scientific Reports**, 5:16487, DOI: 10.1038/srep16487, 2015.

References

[1] Emad Moeendarbary and Andrew R. Harris. "Cell mechanics: Principles, practices, and prospects". In: *Wiley Interdisciplinary Reviews: Systems Biology and Medicine* 6.5 (Sept. 2014), pp. 371–388. DOI: 10.1002/wsbm.1275.

[2] Marco Capitanio and Francesco S. Pavone. "Interrogating biology with force: single molecule high-resolution measurements with optical tweezers." In: *Biophysical journal* 105.6 (Sept. 2013), pp. 1293–303. DOI: 10.1016/j.bpj.2013.08.007.

[3] G. Bao and S. Suresh. "Cell and molecular mechanics of biological materials." In: *Nature materials* 2.11 (Nov. 2003), pp. 715–725. DOI: 10.1038/nmat1001.

[4] William A Comrie and Janis K Burkhardt. "Action and Traction: Cytoskeletal Control of Receptor Triggering at the Immunological Synapse." In: *Frontiers in immunology* 7 (2016), p. 68. DOI: 10.3389/fimmu.2016.00068.

[5] A Weiss et al. "Signal transduction by lymphocyte antigen receptors." In: *Cell* 76.2 (Jan. 1994), pp. 263–74. DOI: 10.1016/0092-8674(94)90334-4.

[6] Kenneth Murphy. *Janeway's Immunobiology*. 8th. New York: Garland Science, 2012.

[7] David R Fooksman et al. "Functional anatomy of T cell activation and synapse formation." In: *Annual review of immunology* 28 (2010), pp. 79–105. DOI: 10.1146/annurev-immunol-030409-101308.

[8] Bernard Malissen and Pierre Bongrand. "Early T Cell Activation: Integrating Biochemical, Structural, and Biophysical Cues". In: *Annual Review of Immunology* 33.1 (Mar. 2015), pp. 539–561. DOI: 10.1146/annurev-immunol-032414-112158.

[9] Jennifer E. Smith-Garvin, Gary A. Koretzky, and Martha S. Jordan. "T cell activation." In: *Annual review of immunology* 27.1 (Jan. 2009), pp. 591–619. DOI: 10.1146/annurev.immunol.021908.132706.

[10] P. Anton van der Merwe and Omer Dushek. "Mechanisms for T cell receptor triggering." In: *Nature reviews. Immunology* 11.1 (Jan. 2011), pp. 47–55. DOI: 10.1038/nri2887.

[11] A Ullrich et al. "Signal transduction by receptors with tyrosine kinase activity." In: *Cell* 61.2 (Apr. 1990), pp. 203–12. DOI: 10.1016/0092-8674(90)90801-K.

[12] Jonathan A Cooper and Hong Qian. "A mechanism for SRC kinase-dependent signaling by noncatalytic receptors." In: *Biochemistry* 47.21 (May 2008), pp. 5681–8. DOI: 10.1021/bi8003044.

[13] Simon J Davis and P Anton van der Merwe. “The kinetic-segregation model: TCR triggering and beyond.” In: *Nature immunology* 7.8 (Aug. 2006), pp. 803–9. DOI: 10.1038/ni1369.

[14] Veronica T Chang et al. “Initiation of T cell signaling by CD45 segregation at ’close contacts’”. In: *Nature Immunology* 17.5 (Mar. 2016), pp. 574–582. DOI: 10.1038/ni.3392.

[15] John R. James and Ronald D. Vale. “Biophysical mechanism of T-cell receptor triggering in a reconstituted system.” In: *Nature* 487.7405 (July 2012), pp. 64–9. DOI: 10.1038/nature11220.

[16] Susan E Levin and Arthur Weiss. “Twisting tails exposed: the evidence for TCR conformational change.” In: *The Journal of experimental medicine* 201.4 (Feb. 2005), pp. 489–92. DOI: 10.1084/jem.20050179.

[17] Susana Minguet et al. “Full Activation of the T Cell Receptor Requires Both Clustering and Conformational Changes at CD3”. In: *Immunity* 26.1 (2007), pp. 43–54. DOI: 10.1016/j.immuni.2006.10.019.

[18] Xiaoshan Shi et al. “Ca2+ regulates T-cell receptor activation by modulating the charge property of lipids”. In: *Nature* 493.7430 (Dec. 2013), pp. 111–115. DOI: 10.1038/nature11699.

[19] Yanping Huang and Ronald L Wange. *T cell receptor signaling: Beyond complex complexes*. July 2004. DOI: 10.1074/jbc.R400012200.

[20] Stefan Feske. “Calcium signalling in lymphocyte activation and disease”. In: *Nature Reviews Immunology* 7.9 (Sept. 2007), pp. 690–702. DOI: 10.1038/nri2152.

[21] Darrell J. Irvine et al. “Direct observation of ligand recognition by T cells.” In: *Nature* 419.6909 (Oct. 2002), pp. 845–9. DOI: 10.1038/nature01076.

[22] C Wülfing et al. “Kinetics and extent of T cell activation as measured with the calcium signal.” In: *The Journal of experimental medicine* 185.10 (May 1997), pp. 1815–25. DOI: 10.1084/jem.185.10.1815.

[23] Janis K Burkhardt, Esteban Carrizosa, and Meredith H Shaffer. “The actin cytoskeleton in T cell activation.” In: *Annual review of immunology* 26 (Jan. 2008), pp. 233–59. DOI: 10.1146/annurev.immunol.26.021607.090347.

[24] Sudha Kumari et al. “T cell antigen receptor activation and actin cytoskeleton remodeling.” In: *Biochimica et biophysica acta* 1838.2 (Feb. 2014), pp. 546–56. DOI: 10.1016/j.bbamem.2013.05.004.

[25] Yan Yu, Alexander A. Smoligovets, and Jay T. Groves. “Modulation of T cell signaling by the actin cytoskeleton”. In: *Journal of Cell Science* 126.5 (Mar. 2013), pp. 1049–1058. DOI: 10.1242/jcs.098210.

[26] Marcus Lettau, Jennifer Pieper, and Ottmar Janssen. “Nck adapter proteins: functional versatility in T cells”. In: *Cell Communication and Signaling* 7.1 (2009), p. 1. DOI: 10.1186/1478-811X-7-1.

[27] Timothy S Gomez et al. “Formins regulate the actin-related protein 2/3 complex-independent polarization of the centrosome to the immunological synapse.” In: *Immunity* 26.2 (Feb. 2007), pp. 177–90. DOI: 10.1016/j.immuni.2007.01.008.

[28] Jun F Allard et al. “Mechanical modulation of receptor-ligand interactions at cell-cell interfaces.” In: *Biophysical journal* 102.6 (Mar. 2012), pp. 1265–1273. DOI: 10.1016/j.bpj.2012.02.006.

[29] Patricia T Yam et al. “Actin-myosin network reorganization breaks symmetry at the cell rear to spontaneously initiate polarized cell motility.” In: *The Journal of cell biology* 178.7 (Sept. 2007), pp. 1207–21. DOI: 10.1083/jcb.200706012.

[30] Rajat Varma et al. “T cell receptor-proximal signals are sustained in peripheral microclusters and terminated in the central supramolecular activation cluster.” In: *Immunity* 25.1 (July 2006), pp. 117–27. DOI: 10.1016/j.immuni.2006.04.010.

[31] Tal Ilani et al. “T cell antigen receptor signaling and immunological synapse stability require myosin IIA.” In: *Nature immunology* 10.5 (May 2009), pp. 531–9. DOI: 10.1038/ni.1723.

[32] A. Grakoui et al. “The Immunological Synapse: A Molecular Machine Controlling T Cell Activation”. In: *Science* 285.5425 (July 1999), pp. 221–227. DOI: 10.1126/science.285.5425.221.

[33] Kaushik Choudhuri et al. “Polarized release of T-cell-receptor-enriched microvesicles at the immunological synapse”. In: *Nature* 507.7490 (Feb. 2014), pp. 118–123. DOI: 10.1038/nature12951.

[34] Tadashi Yokosuka et al. “Newly generated T cell receptor microclusters initiate and sustain T cell activation by recruitment of Zap70 and SLP-76.” In: *Nature immunology* 6.12 (Dec. 2005), pp. 1253–62. DOI: 10.1038/ni1272.

[35] Gabriele Campi, Rajat Varma, and Michael L. Dustin. “Actin and agonist MHC–peptide complex–dependent T cell receptor microclusters as scaffolds for signaling”. In: *The Journal of Experimental Medicine* 202.8 (Oct. 2005), pp. 1031–1036. DOI: 10.1084/jem.20051182.

[36] Johannes B Huppa et al. “TCR-peptide-MHC interactions in situ show accelerated kinetics and increased affinity.” In: *Nature* 463.7283 (Feb. 2010), pp. 963–7. DOI: 10.1038/nature08746.

[37] Jun Huang et al. “The kinetics of two-dimensional TCR and pMHC interactions determine T-cell responsiveness.” In: *Nature* 464.7290 (Apr. 2010), pp. 932–6. DOI: 10.1038/nature08944.

[38] G. Bell. “Models for the specific adhesion of cells to cells”. In: *Science* 200.4342 (May 1978), pp. 618–627. DOI: 10.1126/science.347575.

[39] Zhengyu Ma et al. “Surface-anchored monomeric agonist pMHCs alone trigger TCR with high sensitivity.” In: *PLoS biology* 6.2 (Feb. 2008), e43. DOI: 10.1371/journal.pbio.0060043.

[40] Alexander Babich et al. “F-actin polymerization and retrograde flow drive sustained PLCγ1 signaling during T cell activation.” In: *The Journal of cell biology* 197.6 (June 2012), pp. 775–87. DOI: 10.1083/jcb.201201018.

[41] Noah Joseph, Barak Reicher, and Mira Barda-Saad. “The calcium feedback loop and T cell activation: how cytoskeleton networks control intracellular calcium flux.” In: *Biochimica et biophysica acta* 1838.2 (Feb. 2014), pp. 557–68. DOI: 10.1016/j.bbamem.2013.07.009.

[42] Peter T Sage et al. “Antigen recognition is facilitated by invadosome-like protrusions formed by memory/effector T cells.” In: *Journal of immunology (Baltimore, Md. : 1950)* 188.8 (Apr. 2012), pp. 3686–99. DOI: 10.4049/jimmunol.1102594.

[43] Jason Yi et al. “Actin retrograde flow and actomyosin II arc contraction drive receptor cluster dynamics at the immunological synapse in Jurkat T cells.” In: *Molecular Biology of the Cell* 23.5 (Mar. 2012), pp. 834–52. DOI: 10.1091/mbc.E11-08-0731.

[44] Alexander A Smoligovets et al. “Characterization of dynamic actin associations with T-cell receptor microclusters in primary T cells.” In: *Journal of cell science* 125.Pt 3 (Feb. 2012), pp. 735–42. DOI: 10.1242/jcs.092825.

[45] Ya-Chen Li et al. “Cutting Edge: mechanical forces acting on T cells immobilized via the TCR complex can trigger TCR signaling.” In: *Journal of immunology (Baltimore, Md. : 1950)* 184.11 (June 2010), pp. 5959–63. DOI: 10.4049/jimmunol.0900775.

[46] Sun Taek Kim et al. “The alphabeta T cell receptor is an anisotropic mechanosensor.” In: *The Journal of biological chemistry* 284.45 (Nov. 2009), pp. 31028–37. DOI: 10.1074/jbc.M109.052712.

[47] Sun Taek Kim et al. “TCR Mechanobiology: Torques and Tunable Structures Linked to Early T Cell Signaling.” In: *Frontiers in immunology* 3.April (Jan. 2012), p. 76. DOI: 10.3389/fimmu.2012.00076.

[48] Kenneth H. Hu and Manish J. Butte. “T cell activation requires force generation”. In: *The Journal of Cell Biology* 213.5 (June 2016), pp. 535–542. DOI: 10.1083/jcb.201511053.

[49] Michael L. Dustin and Lance C. Kam. “Tapping out a mechanical code for T cell triggering”. In: *The Journal of Cell Biology* 213.5 (June 2016), pp. 501–503. DOI: 10.1083/jcb.201605072.

[50] Baoyu Liu et al. “Accumulation of dynamic catch bonds between TCR and agonist peptide-MHC triggers T cell signaling.” In: *Cell* 157.2 (Apr. 2014), pp. 357–68. DOI: 10.1016/j.cell.2014.02.053.

[51] M Elzinga et al. “Complete amino-acid sequence of actin of rabbit skeletal muscle.” In: *Proceedings of the National Academy of Sciences of the United States of America* 70.9 (Sept. 1973), pp. 2687–91. DOI: 10.1073/pnas.70.9.2687.

[52] K C Holmes et al. “Atomic model of the actin filament.” In: *Nature* 347.6288 (Sept. 1990), pp. 44–9. DOI: 10.1038/347044a0.

[53] D Bray and J G White. “Cortical flow in animal cells.” In: *Science (New York, N.Y.)* 239.4842 (Feb. 1988), pp. 883–8. DOI: 10.1126/science.3277283.

[54] Daisuke Mizuno et al. “Nonequilibrium mechanics of active cytoskeletal networks.” In: *Science (New York, N.Y.)* 315.5810 (Jan. 2007), pp. 370–3. DOI: 10.1126/science.1134404.

[55] Thomas D Pollard. “Rate constants for the reactions of ATP- and ADP-actin with the ends of actin filaments”. In: *The Journal of Cell Biology* 103.6 (Dec. 1986), pp. 2747–2754. DOI: 10.1083/jcb.103.6.2747.

[56] Miia Bovellan et al. “Cellular control of cortical actin nucleation.” In: *Current biology : CB* 24.14 (July 2014), pp. 1628–35. DOI: 10.1016/j.cub.2014.05.069.

[57] Thomas D. Pollard et al. “Direct observation of dendritic actin filament networks nucleated by Arp2/3 complex and WASP/Scar proteins”. In: *Nature* 404.6781 (Apr. 2000), pp. 1007–1011. DOI: 10.1038/35010008.

[58] Jean-Francois Joanny et al. “The actin cortex as an active wetting layer”. In: (Feb. 2013). arXiv: 1302.5025.

[59] Alf Honigmann et al. “A lipid bound actin meshwork organizes liquid phase separation in model membranes.” In: *eLife* 3 (2014), e01671. DOI: 10.7554/eLife.01671.

[60] Tobias Baumgart, Samuel T. Hess, and Watt W. Webb. “Imaging coexisting fluid domains in biomembrane models coupling curvature and line tension”. In: *Nature* 425.6960 (Oct. 2003), pp. 821–824. DOI: 10.1038/nature02013.

[61] Richard G. Fehon, Andrea I. McClatchey, and Anthony Bretscher. “Organizing the cell cortex: the role of ERM proteins”. In: *Nature Reviews Molecular Cell Biology* 11.4 (Apr. 2010), pp. 276–287. DOI: 10.1038/nrm2866.

[62] Christoph Le Clainche and Marie-France F Carlier. “Regulation of actin assembly associated with protrusion and adhesion in cell migration”. In: *Physiological Reviews* 88.2 (Apr. 2008), pp. 489–513. DOI: 10.1152/physrev.00021.2007..

[63] Yunfei Cai et al. “Nonmuscle myosin IIA-dependent force inhibits cell spreading and drives F-actin flow.” In: *Biophysical journal* 91.10 (Nov. 2006), pp. 3907–20. DOI: 10.1529/biophysj.106.084806.

[64] Stefan A. Koestler et al. “Differentially oriented populations of actin filaments generated in lamellipodia collaborate in pushing and pausing at the cell front”. In: *Nature Cell Biology* 10.3 (Mar. 2008), pp. 306–313. DOI: 10.1038/ncb1692.

[65] Thomas D Pollard and Gary G Borisy. “Cellular motility driven by assembly and disassembly of actin filaments.” In: *Cell* 112.4 (Feb. 2003), pp. 453–465. DOI: 10.1016/S0092-8674(03)00120-X.

[66] T. Isogai et al. “Initiation of lamellipodia and ruffles involves cooperation between mDia1 and the Arp2/3 complex”. In: *Journal of Cell Science* 128.20 (Oct. 2015), pp. 3796–3810. DOI: 10.1242/jcs.176768.

[67] A Ponti et al. “Two distinct actin networks drive the protrusion of migrating cells.” In: *Science (New York, N.Y.)* 305.5691 (Sept. 2004), pp. 1782–6. DOI: 10.1126/science.1100533.

[68] Gaudenz Danuser. “Testing the lamella hypothesis: the next steps on the agenda.” In: *Journal of cell science* 122.Pt 12 (June 2009), pp. 1959–62. DOI: 10.1242/jcs.054379.

[69] Rudolf Merkel et al. “Cell force microscopy on elastic layers of finite thickness.” In: *Biophysical journal* 93.9 (Nov. 2007), pp. 3314–23. DOI: 10.1529/biophysj.107.111328.

[70] Huw Colin-York et al. “Super-Resolved Traction Force Microscopy (STFM).” In: *Nano letters* 16.4 (Apr. 2016), pp. 2633–8. DOI: 10.1021/acs.nanolett.6b00273.

[71] Saba Ghassemi et al. “Cells test substrate rigidity by local contractions on submicrometer pillars.” In: *Proceedings of the National Academy of Sciences of the United States of America* 109.14 (Apr. 2012), pp. 5328–33. DOI: 10.1073/pnas.1119886109.

[72] Viola Vogel and Michael Sheetz. “Local force and geometry sensing regulate cell functions.” In: *Nature reviews. Molecular cell biology* 7.4 (Apr. 2006), pp. 265–75. DOI: 10.1038/nrm1890.

[73] Brandon L Blakely et al. “A DNA-based molecular probe for optically reporting cellular traction forces”. In: *Nature Methods* 11.12 (Oct. 2014), pp. 1229–1232. DOI: 10.1038/nmeth.3145.

[74] Carsten Grashoff et al. “Measuring mechanical tension across vinculin reveals regulation of focal adhesion dynamics.” In: *Nature* 466.7303 (July 2010), pp. 263–6. DOI: 10.1038/nature09198.

[75] Daniel R Stabley et al. “Visualizing mechanical tension across membrane receptors with a fluorescent sensor.” In: *Nature methods* 9.1 (Jan. 2012), pp. 64–7. DOI: 10.1038/nmeth.1747.

[76] Yang Liu et al. “Tension sensing nanoparticles for mechano-imaging at the living/nonliving interface.” In: *Journal of the American Chemical Society* 135.14 (Apr. 2013), pp. 5320–3. DOI: 10.1021/ja401494e.

[77] Xuefeng Wang and Taekjip Ha. “Defining single molecular forces required to activate integrin and notch signaling.” In: *Science (New York, N.Y.)* 340.6135 (May 2013), pp. 991–4. DOI: 10.1126/science.1231041.

[78] Masatoshi Morimatsu et al. “Visualizing the Interior Architecture of Focal Adhesions with High-Resolution Traction Maps”. In: *Nano Letters* 15.4 (Apr. 2015), pp. 2220–2228. DOI: 10.1021/nl5047335.

[79] William J Polacheck and Christopher S Chen. “Measuring cell-generated forces: a guide to the available tools”. In: *Nature Methods* 13.5 (Apr. 2016), pp. 415–423. DOI: 10.1038/nmeth.3834.

[80] Daniel J. Müller and Yves F. Dufrêne. “Atomic force microscopy as a multifunctional molecular toolbox in nanobiotechnology”. In: *Nature Nanotechnology* 3.5 (May 2008), pp. 261–269. DOI: 10.1038/nnano.2008.100.

[81] Andrew R Harris and G T Charras. “Experimental validation of atomic force microscopy-based cell elasticity measurements”. In: *Nanotechnology* 22.34 (Aug. 2011), p. 345102. DOI: 10.1088/0957-4484/22/34/345102.

[82] Allison M. Whited and Paul S.-H. Park. “Atomic force microscopy: A multifaceted tool to study membrane proteins and their interactions with ligands”. In: *Biochimica et Biophysica Acta (BBA) - Biomembranes* 1838.1 (2014), pp. 56–68. DOI: 10.1016/j.bbamem.2013.04.011.

[83] Jordi Alcaraz et al. “Microrheology of human lung epithelial cells measured by atomic force microscopy.” In: *Biophysical journal* 84.3 (Mar. 2003), pp. 2071–9. DOI: 10.1016/S0006-3495(03)75014-0.

[84] Eric M Darling et al. “Viscoelastic properties of human mesenchymally-derived stem cells and primary osteoblasts, chondrocytes, and adipocytes”. In: *Journal of Biomechanics* 41.2 (Jan. 2008), pp. 454–464. DOI: 10.1016/j.jbiomech.2007.06.019.

[85] Susana Moreno-Flores et al. “Stress relaxation and creep on living cells with the atomic force microscope: a means to calculate elastic moduli and viscosities of cell components.” In: *Nanotechnology* 21.44 (Nov. 2010), p. 445101. DOI: 10.1088/0957-4484/21/44/445101. arXiv: 1003.0862.

[86] Keir C Neuman and Attila Nagy. “Single-molecule force spectroscopy: optical tweezers, magnetic tweezers and atomic force microscopy.” In: *Nature methods* 5.6 (June 2008), pp. 491–505. DOI: 10.1038/nmeth.1218.

[87] Jochen Guck et al. “Optical deformability as an inherent cell marker for testing malignant transformation and metastatic competence.” In: *Biophysical journal* 88.5 (May 2005), pp. 3689–98. DOI: 10.1529/biophysj.104.045476.

[88] J Guck et al. “The optical stretcher: a novel laser tool to micromanipulate cells.” In: *Biophysical journal* 81.2 (Aug. 2001), pp. 767–84. DOI: 10.1016/S0006-3495(01)75740-2.

[89] F M Hochmuth et al. “Deformation and flow of membrane into tethers extracted from neuronal growth cones.” In: *Biophysical journal* 70.1 (Jan. 1996), pp. 358–69. DOI: 10.1016/S0006-3495(96)79577-2.

[90] Drazen Raucher and Michael P. Sheetz. “Characteristics of a Membrane Reservoir Buffering Membrane Tension”. In: *Biophysical Journal* 77.4 (1999), pp. 1992–2002. DOI: 10.1016/S0006-3495(99)77040-2.

[91] Bruno Pontes et al. “Membrane Elastic Properties and Cell Function”. In: *PLoS ONE* 8.7 (July 2013). Ed. by Stefan FT. Weiss, e67708. DOI: 10.1371/journal.pone.0067708.

[92] Robert M Hochmuth. “Micropipette aspiration of living cells.” In: *Journal of biomechanics* 33.1 (Jan. 2000), pp. 15–22. DOI: 10.1016/S0021-9290(99)00175-X.

[93] Yiider Tseng, Thomas P. Kole, and Denis Wirtz. “Micromechanical mapping of live cells by multiple-particle-tracking microrheology.” In: *Biophysical journal* 83.6 (Dec. 2002), pp. 3162–76. DOI: 10.1016/S0006-3495(02)75319-8.

[94] Giuliano Scarcelli et al. “Noncontact three-dimensional mapping of intracellular hydromechanical properties by Brillouin microscopy”. In: *Nature Methods* 12.12 (Dec. 2015), pp. 1132–1134. DOI: 10.1038/nmeth.3616.

[95] KT Bashour and Alexander Gondarenko. “CD28 and CD3 have complementary roles in T-cell traction forces”. In: *PNAS* 13 (2014). DOI: 10.1073/pnas.1315606111.

[96] K. L. Hui et al. “Cytoskeletal forces during signaling activation in Jurkat T-cells”. In: *Molecular Biology of the Cell* 26.4 (Feb. 2015), pp. 685–695. DOI: 10.1091/mbc.E14-03-0830.

[97] Yang Liu et al. “DNA-based nanoparticle tension sensors reveal that T-cell receptors transmit defined pN forces to their antigens for enhanced fidelity”. In: *Proceedings of the National Academy of Sciences* 113.20 (May 2016), pp. 5610–5615. DOI: 10.1073/pnas.1600163113.

[98] W F Scherer, J T Syverton, and G O Gey. "Studies on the propagation in vitro of poliomyelitis viruses. IV. Viral multiplication in a stable strain of human malignant epithelial cells (strain HeLa) derived from an epidermoid carcinoma of the cervix." In: *The Journal of experimental medicine* 97.5 (May 1953), pp. 695–710.

[99] Edward L. Barsumian et al. "IgE-induced histamine release from rat basophilic leukemia cell lines: isolation of releasing and nonreleasing clones". In: *European Journal of Immunology* 11.4 (1981), pp. 317–323. DOI: 10.1002/eji.1830110410.

[100] Ulrich Schneider, Hans-Ulrich Schwenk, and Georg Bornkamm. "Characterization of EBV-genome negative "null" and "T" cell lines derived from children with acute lymphoblastic leukemia and leukemic transformed non-Hodgkin lymphoma". In: *International Journal of Cancer* 19.5 (May 1977), pp. 621–626. DOI: 10.1002/ijc.2910190505.

[101] Milos Aleksic et al. "Dependence of T cell antigen recognition on T cell receptor-peptide MHC confinement time." In: *Immunity* 32.2 (Feb. 2010), pp. 163–74. DOI: 10.1016/j.immuni.2009.11.013.

[102] J.-L. Ji-Li Chen et al. "Ca2+ release from the endoplasmic reticulum of NY-ESO-1-specific T cells is modulated by the affinity of TCR and by the use of the CD8 coreceptor." In: *Journal of immunology (Baltimore, Md. : 1950)* 184.4 (Feb. 2010), pp. 1829–1839. DOI: 10.4049/jimmunol.0902103.

[103] Yi Li et al. "Directed evolution of human T-cell receptors with picomolar affinities by phage display." In: *Nature biotechnology* 23.3 (Mar. 2005), pp. 349–54. DOI: 10.1038/nbt1070.

[104] R Zufferey et al. "Multiply attenuated lentiviral vector achieves efficient gene delivery in vivo." In: *Nature biotechnology* 15.9 (Sept. 1997), pp. 871–5. DOI: 10.1038/nbt0997-871.

[105] A Radu Aricescu, Weixian Lu, and E Yvonne Jones. "A time- and cost-efficient system for high-level protein production in mammalian cells". In: *Acta Crystallographica Section D: Biological Crystallography* 62.10 (Oct. 2006), pp. 1243–1250. DOI: 10.1107/S0907444906029799.

[106] Y H Ding et al. "Four A6-TCR/peptide/HLA-A2 structures that generate very different T cell signals are nearly identical." In: *Immunity* 11.1 (July 1999), pp. 45–56. DOI: 10.1016/S1074-7613(00)80080-1.

[107] Andreas Holzinger. "Jasplakinolide: an actin-specific reagent that promotes actin polymerization." In: *Methods in molecular biology (Clifton, N.J.)* 586 (2009), pp. 71–87. DOI: 10.1007/978-1-60761-376-3_4.

[108] Justin R. Tse et al. "Preparation of hydrogel substrates with tunable mechanical properties." In: *Current protocols in cell biology / editorial board, Juan S. Bonifacino ... [et al.]* Chapter 10.June (June 2010), Unit 10.16. DOI: 10.1002/0471143030.cb1016s47.

[109] Aleksandra K Denisin and Beth L Pruitt. "Tuning the Range of Polyacrylamide Gel Stiffness for Mechanobiology Applications". In: *ACS Applied Materials & Interfaces* (2016), acsami.5b09344. DOI: 10.1021/acsami.5b09344.

[110] N M Green. “A spectrophotometric assay for avidin and biotin based on binding of dyes by avidin”. In: *The Biochemical journal* 94 (Mar. 1965), pp. 23C–24C.

[111] Violeta G. Janolino, Javier Fontecha, and Harold E. Swaisgood. “A spectrophotometric assay for biotinbinding sites of immobilized avidin”. In: *Applied Biochemistry and Biotechnology* 56.1 (Jan. 1996), pp. 1–7. DOI: 10.1007/BF02787865.

[112] Giuseppe Vicidomini et al. “Sharper low-power STED nanoscopy by time gating.” In: *Nature methods* 8.7 (June 2011), pp. 571–573. DOI: 10.1038/nmeth.1624.

[113] B.-C. Chen et al. “Lattice light-sheet microscopy: Imaging molecules to embryos at high spatiotemporal resolution”. In: *Science* 346.6208 (Oct. 2014), pp. 1257998–1257998. DOI: 10.1126/science.1257998.

[114] Dong Li et al. “Extended-resolution structured illumination imaging of endocytic and cytoskeletal dynamics”. In: *Science* 349.6251 (Aug. 2015), aab3500–aab3500. DOI: 10.1126/science.aab3500. arXiv: 15334406.

[115] Mats G L Gustafsson et al. “Three-dimensional resolution doubling in wide-field fluorescence microscopy by structured illumination.” In: *Biophysical journal* 94.12 (June 2008), pp. 4957–70. DOI: 10.1529/biophysj.107.120345.

[116] Marco Fritzsche et al. “CalQuo: automated, simultaneous single-cell and population-level quantification of global intracellular Ca2+ responses”. In: *Scientific Reports* 5 (Nov. 2015), p. 16487. DOI: 10.1038/srep16487.

[117] Yongxiang Gao and Maria L. Kilfoil. “Accurate detection and complete tracking of large populations of features in three dimensions”. In: *Optics Express* 17.6 (Mar. 2009), p. 4685. DOI: 10.1364/OE.17.004685.

[118] Chunming Li et al. “Distance regularized level set evolution and its application to image segmentation.” In: *IEEE transactions on image processing : a publication of the IEEE Signal Processing Society* 19.12 (Dec. 2010), pp. 3243–54. DOI: 10.1109/TIP.2010.2069690.

[119] C Liu. “Beyond Pixels: Exploring New Representations and Applications for Motion Analysis”. Doctoral Thesis. Massachusetts Institute of Technology, May 2009.

[120] A K Harris, P Wild, and D Stopak. “Silicone rubber substrata: a new wrinkle in the study of cell locomotion.” In: *Science (New York, N.Y.)* 208.4440 (Apr. 1980), pp. 177–9. DOI: 10.1126/science.6987736.

[121] Sergey V. Plotnikov et al. “Force Fluctuations within Focal Adhesions Mediate ECM-Rigidity Sensing to Guide Directed Cell Migration”. In: *Cell* 151.7 (Dec. 2012), pp. 1513–1527. DOI: 10.1016/j.cell.2012.11.034.

[122] Benedikt Sabass et al. “High resolution traction force microscopy based on experimental and computational advances.” In: *Biophysical journal* 94.1 (Jan. 2008), pp. 207–20. DOI: 10.1529/biophysj.107.113670.

[123] L Landau and E Lifschitz. *Theory of Elasticity*. Oxford: Elsevier, 1986.

[124] Sergey V Plotnikov et al. *High-Resolution Traction Force Microscopy*. 1st ed. Vol. 123. Elsevier Inc., 2014, pp. 367–394. DOI: 10.1016/B978-0-12-420138-5.00020-3.

[125] James P Butler et al. “Traction fields, moments, and strain energy that cells exert on their surroundings.” In: *American journal of physiology. Cell physiology* 282.3 (Mar. 2002), pp. C595–605. DOI: 10.1152/ajpcell.00270.2001.

[126] Heinz Engl. *Regularization of inverse problems*. Dordrecht Boston: Kluwer Academic Publishers, 1996.

[127] U S Schwarz et al. “Calculation of Forces at Focal Adhesions from Elastic Substrate Data : The Effect of Localized Force and the Need for Regularization”. In: *Biophysical journal* 83.September (Sept. 2002), pp. 1380–1394. DOI: 10.1016/S0006-3495(02)73909-X.

[128] Alejandro Sune-Aunon et al. “L1-regularized reconstruction for traction force microscopy”. In: *2016 IEEE 13th International Symposium on Biomedical Imaging (ISBI)*. IEEE, Apr. 2016, pp. 140–144. DOI: 10.1109/ISBI.2016.7493230.

[129] Sangyoon J Han et al. “Traction microscopy to identify force modulation in subresolution adhesions.” In: *Nature methods* 12.7 (June 2015), pp. 653–6. DOI: 10.1038/nmeth.3430.

[130] Tikhonov A. “Solution of Incorrectly Formulated Problems and the Regularization Method”. In: *Soviet Math. Dokl.* 5 (1963), pp. 1035/1038.

[131] PC Hansen. *The L-curve and its use in the numerical treatment of inverse problems*. Vol. 2. 1999, pp. 1–24.

[132] Nicolas Chenouard et al. “Objective comparison of particle tracking methods”. In: *Nature Methods* 11.3 (Jan. 2014), pp. 281–289. DOI: 10.1038/nmeth.2808.

[133] Jean-Louis Martiel et al. “Measurement of cell traction forces with ImageJ”. In: *Methods in cell biology*. Vol. 125. 2015, pp. 269–287. DOI: 10.1016/bs.mcb.2014.10.008.

[134] Markus Raffel et al. *Particle Image Velocimetry A Practical Guide*. Springer, 1998.

[135] Richard D. Keane and Ronald J. Adrian. “Theory of cross-correlation analysis of PIV images”. In: *Applied Scientific Research* 49.3 (July 1992), pp. 191–215. DOI: 10.1007/BF00384623.

[136] Dhruv K. Vig, Alex E. Hamby, and Charles W. Wolgemuth. “On the Quantification of Cellular Velocity Fields.” In: *Biophysical journal* 110.7 (Apr. 2016), pp. 1469–75. DOI: 10.1016/j.bpj.2016.02.032.

[137] Samantha G. Knoll, M. Yakut Ali, and M. Taher A. Saif. “A Novel Method for Localizing Reporter Fluorescent Beads Near the Cell Culture Surface for Traction Force Microscopy”. In: *Journal of Visualized Experiments* 91 (Sept. 2014), e51873–e51873. DOI: 10.3791/51873.

[138] Wesley R Legant et al. “Multidimensional traction force microscopy reveals out-of-plane rotational moments about focal adhesions.” In: *Proceedings of the National Academy of Sciences of the United States of America* 110.3 (Jan. 2013), pp. 881–6. DOI: 10.1073/pnas.1207997110.

[139] Amir Rashid et al. “Review: Diagnostic and therapeutic applications of rat basophilic leukemia cells”. In: *Molecular Immunology* 52.3-4 (Oct. 2012), pp. 224–228. DOI: 10.1016/j.molimm.2012.05.019.

[140] Travis J Gould et al. "Auto-aligning stimulated emission depletion microscope using adaptive optics." In: *Optics letters* 38.11 (June 2013), pp. 1860–2. DOI: 10.1364/OL.38.001860.

[141] Travis J Gould et al. "Adaptive optics enables 3D STED microscopy in aberrating specimens." In: *Optics express* 20.19 (Sept. 2012), pp. 20998–1009.

[142] Lars Kjer-Nielsen et al. "Crystal structure of the human T cell receptor CD3$\epsilon\gamma$ heterodimer complexed to the therapeutic mAb OKT3". In: *Proceedings of the National Academy of Sciences of the United States of America* 101.20 (2004), p. 7675. DOI: 10.1073/pnas.0402295101.

[143] T Chatila et al. "Mechanisms of T cell activation by the calcium ionophore ionomycin." In: *Journal of immunology (Baltimore, Md. : 1950)* 143.4 (Aug. 1989), pp. 1283–9.

[144] Edward Judokusumo et al. "Mechanosensing in T lymphocyte activation." In: *Biophysical journal* 102.2 (Jan. 2012), pp. L5–7. DOI: 10.1016/j.bpj.2011.12.011.

[145] Janosch Deeg et al. "T cell activation is determined by the number of presented antigens". In: *Nano Letters* 13.11 (2013), pp. 5619–5626. DOI: 10.1021/nl403266t.

[146] CE Chan and DJ Odde. "Traction dynamics of filopodia on compliant substrates". In: *Science Signaling* 322.December (2008), pp. 1687–1691.

[147] Mark L Kachanov, B Shafiro, and Igor Tsukrov. *Handbook of Elasticity Solutions*. Springer, 2003.

[148] S.-S. Zhou and X.-L. Gao. "Solutions of the generalized half-plane and half-space Cerruti problems with surface effects". In: *Zeitschrift für angewandte Mathematik und Physik* 66.3 (June 2014), pp. 10–12. DOI: 10.1007/s00033-014-0419-4.

[149] D. Anagnostou, P. Gourgiotis, and H. Georgiadis. "The Cerruti problem in dipolar gradient elasticity". In: *Mathematics and Mechanics of Solids* 20.9 (Oct. 2015), pp. 1088–1106. DOI: 10.1177/1081286513514882.

[150] M G Gustafsson. "Surpassing the lateral resolution limit by a factor of two using structured illumination microscopy." In: *Journal of microscopy* 198.Pt 2 (May 2000), pp. 82–7.

[151] Bastian Rouven Brückner et al. "Ezrin is a Major Regulator of Membrane Tension in Epithelial Cells." In: *Scientific reports* 5 (2015), p. 14700. DOI: 10.1038/srep14700.

[152] Wesley R Legant et al. "Measurement of mechanical tractions exerted by cells in three-dimensional matrices". In: 7.12 (2010). DOI: 10.1038/NMETH.1531.

[153] Christian Osseforth et al. "Simultaneous dual-color 3D STED microscopy." In: *Optics express* 22.6 (Mar. 2014), pp. 7028–39.

[154] William A. Comrie, Alexander Babich, and Janis K. Burkhardt. "F-actin flow drives affinity maturation and spatial organization of LFA-1 at the immunological synapse". In: *The Journal of Cell Biology* 208.4 (2015).

Appendix A

The Cerruti Problem

A point force, $\mathbf{F} = F\mathbf{e}_1$, acting at the origin tangential to an semi-infinite elastic half-space defines a classical problem from elastic theory, known as the Cerruti problem (see Figure A.1).[147] The components of the displacements resulting from the point force are given by,

$$u_1 = \frac{F}{4G\pi}\left\{\frac{1}{R} + \frac{{x_1}^2}{R^3} + \frac{1-2\nu}{R+x_3}\left[1 - \frac{{x_1}^2}{R(R-x_3)}\right]\right\} \tag{A.1}$$

$$u_2 = \frac{F}{4G\pi R}\left\{\frac{x_1 x_2}{R^2} - (1-2\nu)\frac{x_1 x_2}{(R+x_3)^2}\right\} \tag{A.2}$$

$$u_3 = \frac{F}{4G\pi R}\left\{\frac{x_1 x_3}{R^2} + (1-2\nu)\frac{x_1}{(R+x_3)}\right\} \tag{A.3}$$

$$R = \sqrt{{x_1}^2 + {x_2}^2 + {x_3}^2} \tag{A.4}$$

Next, we calculate the displacement at the surface of the half-space ($x_3 = 0$), along the line defined by the origin ($x_2 = 0$). In this case, $R = \sqrt{{x_1}^2 + 0^2 + 0^2} = x_1$, therefore the displacement along $\mathbf{e}_1$ as a function of the distance from the origin x_1 is,

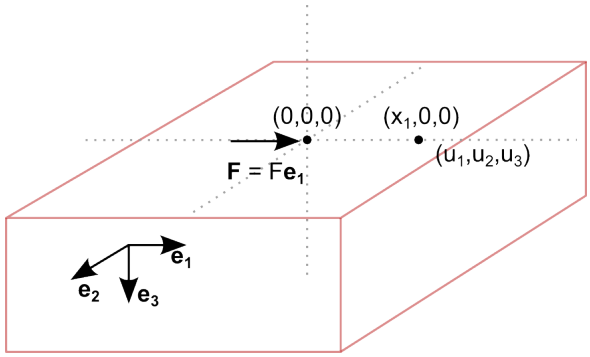


Fig. A.1 The Cerruti problem - Schematic outlining the Cerruti problem

$$u_1(x_1,0,0) = \frac{F}{4G\pi}\left\{\frac{1}{x_1} + \frac{{x_1}^2}{{x_1}^3} + \frac{1-2\nu}{x_1+0}\left[1 - \frac{{x_1}^2}{{x_1}^2+0}\right]\right\} \tag{A.5}$$

$$u_1(x_1,0,0) = \frac{F}{4G\pi}\left\{\frac{1}{x_1} + \frac{1}{x_1}\right\} \tag{A.6}$$

$$u_1(x_1,0,0) = \frac{F}{2G\pi x_1} \tag{A.7}$$

Substituting for the shear modulus, G,

$$G = \frac{E}{2(1+\nu)} \tag{A.8}$$

$$u_1(x_1,0,0) = \frac{F(1+\nu)}{E\pi x_1} \tag{A.9}$$

Rearranging for the magnitude of the point force, F,

$$F = \frac{E\pi x_1 u_1}{(1+\nu)} \tag{A.10}$$

Note, this is the same solution found by Chan *et al.*.[146]

Along $\mathbf{e}_2$,

$$u_2(x_1,0,0) = 0 \tag{A.11}$$

Along $\mathbf{e}_3$,

$$u_3(x_1, 0, 0) = \frac{F(1-2\nu)}{4G\pi x_1} \tag{A.12}$$

$$u_3(x_1, 0, 0) = \frac{F(1-2\nu)}{4G\pi x_1} \tag{A.13}$$

$$u_3(x_1, 0, 0) = \frac{F(1-\nu+2\nu^2)}{2E\pi x_1} \tag{A.14}$$

We only consider the displacements along the direction $\mathbf{e}_1$, therefore the solution of interest is,

$$F = \frac{E\pi x_1 u_1}{(1+\nu)} \tag{A.15}$$

x_1 is the distance from the point force and u_1 is the strain at the point x_1. In the load-fail experiments, x_1 is zero, as the point force co-localises with the bead position. By plotting u_1 as a function of x_1 a singularity is present at the origin (E=3000 Pa, F = 0.5nN, ν=0.5)(see Figure A.2). The represents a limitation of the classical theory, which implies an infinite displacement of the elastic medium, independent of the force, at the origin[149].[148]

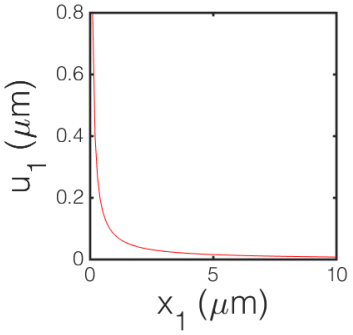


Fig. A.2 1D Cerruti problem - 1D dependence of the displacement with distance from point force